

DISS. ETH NO. 20217

**MODELING AND MULTI-OBJECTIVE  
OPTIMIZATION OF INDUCTIVE  
POWER COMPONENTS**

A dissertation submitted to  
ETH ZURICH

for the degree of  
Doctor of Sciences

presented by  
JONAS MÜHLETHALER  
M.Sc. ETH Zürich  
born 16. September 1982  
citizen of Lucerne, Switzerland

accepted on the recommendation of  
Prof. Dr. Johann W. Kolar, examiner  
Prof. Dr. Charles R. Sullivan, co-examiner

2012



# Acknowledgments

First of all, I would like to thank Prof. Johann W. Kolar for giving me the opportunity to do my Ph.D. thesis in his group. The environment he established in his laboratory is impressive, and I felt lucky to work there. He always trusted me and gave me plenty of freedom, which was perfect for me. I also would like to thank Prof. Charles R. Sullivan for being the co-examiner of my Ph.D. thesis. Also, I would like to thank him for creating the foundation of my research, which finally resulted in the  $i^2$ GSE.

ABB Corporate Research sponsored the work behind this thesis. I would like to thank my supervisor Dr. Andreas Ecklebe for the numerous scientific discussions and his exceptional interest in the outcome of the work. Also, I would like to thank Henri Kinnunen from ABB Finland for his interests in my work.

I would like to thank the entire PES staff including Ph.D. students, post-doctoral researchers, secretaries, administrators, and the electronics laboratory for providing a great research atmosphere.

Furthermore, a big thanks goes to the semester and master students who have supported me in my research: Sascha O. Schneider, Robert Blattmann, and Marko Tanasković.

This Ph.D. thesis would not have been successful and, more importantly, would not have been fun without interactions with people in and outside the PES. Discussions led many (weird) theories in magnetism, which (sometimes) were discarded almost as quickly as they were formed. Also the glorious, unforgettable performances in many sport events (such as the SOLA-Stafette, the ASVZ soccer championship, or the ITET Summer Fight) made the time at PES clearly a good one. Many people were involved in these events, and the boundaries between work and pleasure became blurry. Therefore, here is

---

an alphabetical list of the people with whom I am grateful to have shared this important phase of my life: Uwe Badstübner, Jürgen Biela, David Boillat, Daniel Christen, Bernardo Cougo, Thomas Friedli, Ivana Kovačević, Fabio Magagna, Christoph Marxgut, Gabriel Ortiz, Mario Schweizer, Thiago Soeiro, Arda Tüysüz, and Benjamin Wrzecionko.

Last but not least, I would like to thank my family and all my friends for the great support they have given me anytime and anywhere.

# Abstract

This thesis deals with the modeling and multi-objective optimization of inductive power components, in order to improve the efficiency and/or power density of power electronic systems.

The first part of the thesis introduces how to model magnetic circuits, i.e. how to set up an accurate reluctance model of an inductive component. A novel approach to accurately determine the reluctances of air gaps is introduced. The approach is easy to handle as it is based on a modular concept where a simple basic geometry is used as a building block to describe different three dimensional air gap shapes.

The second part of the thesis deals with core loss modeling. The applied core loss approach can be seen as a hybrid of an improved version of the empirical Steinmetz equation and an approach based on a material loss database (loss map). In order to build the material loss database, core loss measurements must be made. Therefore, special focus is placed on how core losses can be measured and what measurements are necessary for an accurate core loss modeling.

Relaxation effects in magnetic materials are discussed. In modern power electronic systems, voltages across inductors or transformers generally show rectangular shapes, including periods of zero voltage. In most core loss models, the phase where the voltage across the magnetic component is zero (i.e. the flux remains constant) is not considered. It is implicitly assumed that no losses occur when the flux remains constant. However, as measurements show, this is not a valid simplification. In phases of constant flux, losses still occur in the material. This is due to relaxation processes. A new core loss modeling approach that takes such relaxation effects into consideration is given.

Another aspect to be considered is the fact that core losses are influenced by a DC premagnetization. The Steinmetz Premagnetization

---

Graph (SPG) that shows the dependency of the Steinmetz parameters ( $\alpha$ ,  $\beta$  and  $k$ ) on premagnetization is proposed. This permits the calculation of core losses under DC bias conditions.

Power electronic engineers often work with circuit simulators in order to validate their designs before building costly prototypes. It is shown, how to calculate core losses from a simulated flux waveform. In order to do this, the simulated flux waveform is divided into its fundamental flux waveform and into piecewise linear flux waveform segments. The loss energy is then calculated for the fundamental and all piecewise linear segments, summed and divided by the fundamental period length in order to determine the average core loss. Another aspect to be considered in core loss calculation is the effect of the core shape and size. By introducing a reluctance model of the core, and with it, calculating the flux density in every core section of (approximately) homogenous flux density, one can calculate the losses of each core section. The core losses of each section are then summed to obtain the total core losses. This generally leads to a high accuracy. However, under certain circumstances, in tape wound cores a flux orthogonal to the tape layers can lead to high eddy currents and thus to high core losses.

The second source of losses in inductive components is the ohmic losses in the windings. The resistance of a conductor increases with increasing frequency due to eddy currents. Self-induced eddy currents inside a conductor lead to the skin-effect. Eddy currents due to an external alternating magnetic field, e.g. the air gap fringing field or the magnetic field from other conductors, lead to the proximity-effect. The skin-effect and proximity-effect losses can be calculated for round, litz, or foil windings; provided that the external field and the current is known exactly. However, the calculation of the external magnetic field strength, which has to be known when calculating the proximity losses, is challenging. In the case of an un-gapped core and windings that are fully-enclosed by core material, 1D approximations to determine the magnetic field exist. However, in the case of gapped cores, such 1D approximations are not applicable as the fringing field of the air gap cannot be described in a 1D manner. The approach presented in the thesis is a 2D approach in which the magnetic field at any position can be calculated as the superposition of the fields of each of the conductors. The impact of a magnetic conducting material can be modeled with the *method of images*. The presence of an air gap can be modeled as a fictitious conductor carrying a current equal to the Magneto-Motive

---

Force (MMF) across the air gap.

Another important aspect in modeling inductive components is their thermal behavior. This is not only important to avoid overheating; it also has importance in modeling the losses correctly, as they are influenced by the temperature. Formulae that allow heat conduction, convection and radiation to be calculated are given.

The last part of the thesis is about the multi-objective optimization of inductive power components. The optimization of inductive components is illustrated using the example of LCL filters for three-phase PFC rectifiers. The optimization procedure leads to different filter designs depending on whether the aim of the optimization is more on reducing the volume  $V$  or more on reducing the losses  $P$ . Furthermore, an overall system optimization, i.e. an optimization of the complete three-phase PFC rectifier, is given.



# Kurzfassung

Diese Doktorarbeit beschäftigt sich mit der umfassenden Modellierung und Optimierung von induktiven Komponenten, um die Effizienz bzw. Leistungsdichte von leistungselektronischen Systemen zu erhöhen.

Im ersten Teil der Arbeit wird gezeigt wie man Reluktanzmodelle induktiver Komponenten aufstellt, wobei der Fokus auf der Bestimmung von Luftspaltreluktanzen liegt. Zur genauen Bestimmung der Luftspaltreluktanz wird ein neuer Rechenansatz eingeführt. Der Ansatz basiert auf einem modularen Konzept bei dem eine einfache grundlegende Geometrie als Baustein verwendet wird, um verschiedene dreidimensionale Luftspalttypen zu beschreiben.

Der zweite Teil der Arbeit befasst sich mit der Berechnung von Kernverlusten. Der angewandte Ansatz zur Bestimmung der Kernverluste kann als eine Kombination aus einer erweiterten Version der empirischen Steinmetzgleichung und einem Ansatz basierend auf einer Kernmaterial-Verlustdatenbank gesehen werden. Für das Aufstellen dieser Datenbank müssen Kernverluste von verschiedenen Materialien gemessen werden. Deshalb ist ein besonderer Schwerpunkt darauf gelegt, wie Kernverluste gemessen werden und welche Messungen für eine genaue Modellierung der Kernverluste notwendig sind.

Des Weiteren ist eine ausführliche Diskussion über Relaxationseffekte in magnetischen Materialien gegeben. In modernen leistungselektronischen Systemen liegen typischerweise rechteckförmige Spannungen an den induktiven Komponenten, einschliesslich Zeiten mit Nullspannung. In den meisten Kernverlustmodellen ist die Phase, wo die Spannung über den magnetischen Komponenten Null ist (d.h. wo der magnetische Fluss konstant bleibt) nicht berücksichtigt. Es wird implizit davon ausgegangen, dass keine Verluste auftreten, wenn der Fluss konstant bleibt. In der vorliegenden Arbeit werden Messungen vorgestellt,

---

welche zeigen, dass zu Beginn eines Intervalls mit konstantem Fluss noch immer Verluste im Material auftreten. Dies ist auf Relaxationsprozesse im Kernmaterial zurückzuführen. Ein neuer Kernverlust-Modellierungsansatz wird vorgestellt, mit welchem diese Relaxationseffekte mitberücksichtigt werden.

Ein weiterer Aspekt, den es zu berücksichtigen gilt ist, dass Kernverluste durch eine DC Vormagnetisierung beeinflusst werden. Leider wird dieses Verhalten in gängigen Datenblättern zu Kernmaterialien nicht weiter spezifiziert. In dieser Doktorarbeit wird der Steinmetz Premagnetization Graph (SPG) bzw. Steinmetz Vormagnetisierungs-Graph eingeführt, welcher die Abhängigkeit der Steinmetzparameter ( $\alpha$ ,  $\beta$  und  $k$ ) bezüglich einer Vormagnetisierung zeigt. Der SPG ermöglicht die Berechnung der Kernverluste in einem Arbeitspunkt mit DC Vormagnetisierung.

Entwickler von induktiven Komponenten arbeiten oftmals mit Schaltungssimulatoren, um ihre Entwürfe vor dem Bau teurer Prototypen zu validieren. Es wird gezeigt, wie von einem simulierten Flussverlauf Kernverluste berechnet werden können. Dazu wird die Verlustenergie für die Grundschwingung und für alle stückweise linearen Segmente einzeln berechnet. Ein weiterer wichtiger Aspekt in der Kernverlustberechnung ist der Einfluss der Form und Grösse des Kernmaterials auf die Verluste. Durch die Einführung eines Reluktanzmodells können die Verluste der einzelnen Abschnitte mit (ungefähr) homogener Flussdichte berechnet werden. Die Kernverluste der einzelnen Abschnitte werden dann aufsummiert. Dieser Ansatz führt zu einer hohen Genauigkeit. Allerdings gibt es Situationen in welchen mit diesem Vorgehen die Kernverluste unterschätzt werden. In Schnittbandkerne kann sich unter gewissen Umständen ein Fluss ausbilden, welcher orthogonal zu den Bändern steht. In dieser Situation bilden sich starke Wirbelströme aus. Diese Wirbelströme führen zu überhöhten Kernverlusten.

Die zweite Quelle von Verlusten in induktiven Bauelementen sind die ohmschen Verluste in den Wicklungen. Der Widerstand eines Leiters steigt mit steigender Frequenz aufgrund von selbst-induzierten Wirbelströmen. Dieser Effekt nennt sich Skin-Effekt. Die Wirbelströme in einem Leiter, welche von einem externen magnetischen Wechselfeld (z.B. dem Luftspaltstreufeld oder dem magnetischen Feld von Nachbarleitern) induziert werden führen zum Proximity-Effekt. Die Verluste aufgrund des Skin-Effekts und Proximity-Effekts können für Rundleiter,

---

für Hochfrequenz-Litze und Folienleiter berechnet werden, vorausgesetzt, dass das äussere Feld genau bekannt ist. Allerdings ist die Bestimmung dieses äusseren Feldes zur Berechnung des Proximity-Effekts nicht ganz trivial. Für den Fall eines Kerns ohne Luftspalt und mit Leitern, die vollständig von Kernmaterial umgeben sind, existieren 1D Ansätze für die Bestimmung des äusseren Feldes. Doch im Fall von Kernen mit Luftspalten sind solche 1D Ansätze nicht anwendbar, da für die Beschreibung des Luftspalt-Streufeldes mindestens eine 2D Beschreibung notwendig ist. Der Ansatz in der vorliegenden Arbeit ist ein 2D Ansatz, bei welchem das Magnetfeld an jeder beliebigen Stelle als Überlagerung der Felder der einzelnen Leitern abgeleitet wird. Die Auswirkungen eines magnetischen leitenden Materials lassen sich mit dem Spiegelungsverfahren beschreiben. Ein Luftspalt kann mittels fiktivem Leiter, welcher einen Strom gleich dem magnetischen Spannungsabfall über dem Luftspalt führt, modelliert werden.

Ein weiterer wichtiger Aspekt bei der Modellierung induktiver Bauelemente ist ihr thermisches Verhalten. Dies ist nicht nur wichtig, um eine thermische Zerstörung zu vermeiden, es ist auch wichtig, um die Verluste korrekt zu modellieren, da diese durch die Temperatur beeinflusst werden. Formeln zur Bestimmung der Kern und Wicklungstemperatur sind gegeben, wobei die Wärmeleitung, Wärmekonvektion, und Wärmestrahlung gerechnet wird.

Im letzten Teil der Arbeit geht es um die Optimierung induktiver Komponenten. Die Optimierung von induktiven Bauelementen wird am Beispiel eines LCL-Filters für dreiphasige PFC-Pulsgleichrichter illustriert. Das vorgestellte Optimierungsverfahren führt zu unterschiedlichen Filterdesigns mit unterschiedlichen Volumina  $V$  und Verlusten  $P$ . Des Weiteren wird eine Optimierung des gesamten Systems, also eine Optimierung des gesamten dreiphasigen PFC-Pulsgleichrichters vorgestellt.



# Contents

|          |   |           |
|----------|---|-----------|
| <b>1</b> | <b>Introduction</b>   | <b>1</b>  |
| 1.1      | Modeling of Inductive Power Components . . . . .  | 2         |
| 1.2      | Multi-Objective Optimization of Inductive Power Components . . . . .                      | 7         |
| 1.3      | Outline of the Thesis . . . . .   | 8         |
| 1.4      | List of Publications . . . . .  | 10        |
| <b>2</b> | <b>Magnetic Circuit Modeling</b>  | <b>13</b> |
| 2.1      | Existing Approaches for Air Gap Reluctance Calculation                                    | 15        |
| 2.1.1    | Method of the Conformal Schwarz-Christoffel Transformation . . . . .                      | 15        |
| 2.1.2    | Increase of the Air Gap Cross-Sectional Area . . . . .                                    | 16        |
| 2.1.3    | FEM Tuned Equations . . . . .   | 17        |
| 2.1.4    | Desired Approach for Air Gap Calculations . . . . .                                       | 17        |
| 2.2      | Air Gap Reluctance . . . . .  | 18        |
| 2.2.1    | Reluctance of Air Gaps with Rectangular Cross-Section . . . . .                           | 18        |
| 2.2.2    | Reluctance of Air Gap with Round Cross-Section . . . . .                                  | 24        |
| 2.2.3    | Adaptation of the Air Gap Reluctance Calculation Approach to Different Problems . . . . . | 24        |
| 2.3      | Core Reluctance . . . . .   | 25        |
| 2.4      | Experimental Results . . . . .  | 27        |
| 2.4.1    | Inductance . . . . .  | 27        |
| 2.4.2    | Saturation . . . . .  | 27        |
| <b>3</b> | <b>Core Loss Modeling</b>   | <b>31</b> |
| 3.1      | Physical Origin of Core Losses . . . . .  | 32        |
| 3.2      | Existing Approaches for Core Loss Calculation . . . . .                                   | 35        |

|          |  |           |
|----------|--|-----------|
| 3.3      | Outline of Novel Core Loss Calculation Models and Approaches . . . . .       | 38        |
| 3.4      | Test Setup to Measure Core Losses . . . . .                                  | 39        |
| 3.5      | Accuracy of the Measurement System . . . . .                                 | 41        |
| 3.5.1    | Phase Shift Error of Voltage and Current Measurement . . . . .               | 43        |
| 3.5.2    | Equipment Accuracy . . . . .   | 45        |
| 3.5.3    | Capacitive Coupling . . . . .  | 45        |
| 3.5.4    | Temperature . . . . .  | 46        |
| 3.5.5    | Comparative Measurement and Conclusion . . . . .                             | 46        |
| 3.6      | Relaxation Effects in Magnetic Materials . . . . .                           | 46        |
| 3.6.1    | Measurement Results . . . . .  | 47        |
| 3.6.2    | Theory of Relaxation Effects . . . . .                                       | 49        |
| 3.6.3    | Shape of B-H Loop for Trapezoidal Flux Waveforms . . . . .                   | 50        |
| 3.6.4    | Model Derivation . . . . .   | 52        |
| 3.6.5    | Measurements on Different Materials . . . . .                                | 63        |
| 3.6.6    | Conclusion and Future Work . . . . .   | 65        |
| 3.7      | Core Losses Under DC Bias Conditions . . . . .                               | 66        |
| 3.7.1    | Measurement Results and the Steinmetz Premagnetization Graph (SPG) . . . . . | 67        |
| 3.7.2    | Influence of Temperature . . . . .   | 72        |
| 3.7.3    | Example How to Use the SPG . . . . .   | 74        |
| 3.7.4    | Core Losses under DC Bias Conditions of Different Materials . . . . .        | 76        |
| 3.7.5    | Conclusion and Future Work . . . . .   | 77        |
| 3.8      | Minor and Major B-H Loops . . . . .  | 77        |
| 3.9      | Hybrid Core Loss Calculation Approach . . . . .                              | 79        |
| 3.9.1    | Use of Loss Map . . . . .  | 82        |
| 3.10     | Influence of Core Shape on Core Losses . . . . .                             | 84        |
| 3.10.1   | Effective Dimensions of Toroidal Cores . . . . .                             | 85        |
| 3.10.2   | General Core Shape . . . . .   | 86        |
| 3.10.3   | Impact of Core Shape on Eddy Current Losses . . . . .                        | 88        |
| 3.10.4   | Dimensional Resonance . . . . .  | 91        |
| 3.10.5   | Losses in Gapped Tape Wound Cores . . . . .                                  | 93        |
| <b>4</b> | <b>Winding Loss Modeling</b>   | <b>97</b> |
| 4.1      | Skin Effect . . . . .  | 98        |
| 4.2      | Proximity Effect . . . . .   | 100       |
| 4.3      | Round Conductor . . . . .  | 102       |

|          |   |            |
|----------|---|------------|
| 4.3.1    | Skin Effect . . . . .   | 103        |
| 4.3.2    | Proximity Effect . . . . .  | 104        |
| 4.3.3    | Multi-Layer Windings Without Air Gap . . . . .                    | 105        |
| 4.3.4    | Multi-Layer Windings With Air Gap . . . . .                       | 107        |
| 4.3.5    | Litz-Wire Windings . . . . .                                      | 110        |
| 4.3.6    | Accuracy Analysis . . . . .                                       | 113        |
| 4.4      | Foil Conductor . . . . .  | 115        |
| 4.4.1    | Skin Effect . . . . .   | 117        |
| 4.4.2    | Proximity Effect . . . . .  | 118        |
| 4.4.3    | Foil Multi-Layer Without Air Gap . . . . .                        | 119        |
| 4.4.4    | Short Foil Conductors . . . . .                                   | 120        |
| 4.4.5    | Foil Multi-Layer With Air Gap . . . . .                           | 121        |
| 4.4.6    | Accuracy Analysis . . . . .                                       | 123        |
| <b>5</b> | <b>Thermal Modeling</b>   | <b>127</b> |
| 5.1      | Overview of Thermal Models . . . . .                              | 127        |
| 5.1.1    | Total Thermal Resistance . . . . .                                | 128        |
| 5.1.2    | Thermal Resistor Networks . . . . .                               | 128        |
| 5.2      | Heat Transfer Mechanisms . . . . .                                | 130        |
| 5.2.1    | Thermal Conduction . . . . .                                      | 130        |
| 5.2.2    | Thermal Natural Convection . . . . .                              | 131        |
| 5.2.3    | Thermal Radiation . . . . .                                       | 136        |
| 5.3      | Practical Implementation Issues . . . . .                         | 137        |
| <b>6</b> | <b>Magnetic Design Environment and Experimental Results</b>       | <b>139</b> |
| 6.1      | Overview of Implemented Loss Modeling Environment . . . . .       | 140        |
| 6.2      | Experiment I . . . . .  | 142        |
| 6.3      | Experiment II . . . . .   | 144        |
| <b>7</b> | <b>Multi-Objective Optimization of Inductive Power Components</b> | <b>147</b> |
| 7.1      | Three-Phase PFC Rectifier with Input Filter . . . . .             | 148        |
| 7.2      | Modeling of Input Filter Components . . . . .                     | 150        |
| 7.2.1    | Calculation of the Inductance . . . . .                           | 150        |
| 7.2.2    | Core Losses . . . . .   | 151        |
| 7.2.3    | Winding Losses . . . . .  | 151        |
| 7.2.4    | Thermal Modeling . . . . .  | 152        |
| 7.2.5    | Capacitor Modeling . . . . .                                      | 152        |
| 7.2.6    | Damping Branch . . . . .  | 153        |

|          |   |            |
|----------|---|------------|
| 7.3      | Optimization of the Input Filter . . . . .                      | 153        |
| 7.3.1    | Optimization Constraints and Conditions . . . . .               | 154        |
| 7.3.2    | Calculation of $L_{2,\min}$ . . . . .                           | 154        |
| 7.3.3    | Loss Calculation of Filter Components . . . . .                 | 155        |
| 7.3.4    | Optimization Procedure . . . . .                                | 156        |
| 7.4      | Optimization Outcomes . . . . .                                 | 159        |
| 7.5      | Experimental Results . . . . .                                  | 160        |
| 7.6      | Overall Rectifier Optimization . . . . .                        | 162        |
| 7.6.1    | Overall Optimized Designs . . . . .                             | 164        |
| 7.7      | Conclusion and Future Work . . . . .                            | 169        |
| <b>8</b> | <b>Summary &amp; Outlook</b>                                    | <b>171</b> |
| 8.1      | Summary . . . . .   | 171        |
| 8.2      | Outlook . . . . .   | 173        |
| <b>A</b> | <b>Appendix</b>   | <b>175</b> |
| A.1      | Derivation of the Basic Reluctance . . . . .                    | 175        |
| A.2      | iGSE and Sinusoidal Flux Waveforms . . . . .                    | 180        |
| A.3      | SPGs of Other Materials . . . . .                               | 181        |
| A.4      | Derivation of the Steinmetz Premagnetization Graph . . . . .    | 181        |
| A.5      | Classic Steinmetz Parameter $k$ . . . . .                       | 185        |
| A.6      | Derivation of Effective Dimensions for Toroidal Cores . . . . . | 185        |
| A.7      | Derivation of Winding Losses in Foil Conductors . . . . .       | 187        |
| A.7.1    | Skin Effect . . . . .   | 188        |
| A.7.2    | Proximity Effect . . . . .                                      | 191        |
| A.8      | Derivation of Winding Losses in Round Conductors . . . . .      | 192        |
| A.8.1    | Skin Effect . . . . .   | 192        |
| A.8.2    | Proximity Effect . . . . .                                      | 194        |
| A.9      | Orthogonality of Winding Losses . . . . .                       | 196        |

# Chapter 1

## Introduction

The three major reasons why the world's energy policy has to be rethought are [1]:

- ▶ global warming / climate change that has to be prevented,
- ▶ dependency on fossil energy sources as oil, gas, coal, etc. that are often located in unstable world regions,
- ▶ and increasing energy costs due to shortage of resources, e.g. discussion about the peak-oil problem.

Bose [2] predicted in 2000 that "it appears that cheap and abundant energy supply which we are now enjoying will be over in future and our society will be forced to move in an altered direction". One step towards a more sustainable energy policy and improved stewardship of available resources could be achieved by promoting electric energy. Taking electric vehicles as an example, even when electricity is generated mainly in coal-fired power plants, the fuel chain efficiency of electrical vehicles compared to gasoline-filled vehicles increases [2].

Power electronics is clearly a key technology in helping to solve any of these upcoming energy issues. Highly efficient power electronic converters allow energy saving through the efficient use of electricity. Power electronics will also play a key role in providing new solutions for transportation systems (e.g. electric vehicles), transmission systems (e.g. HVDC), distribution systems, and integration of new power sources into the grid [3].

The evolution of power electronics closely follows the evolution of power semiconductor devices. Power semiconductor devices have improved in terms of higher current / voltage ratings, and lower conduction and switching losses allowing higher switching frequencies. New power semiconductor devices permit higher system efficiencies and lower system volumes, i.e. higher power densities. Generally, one can see a trend in power electronics research towards higher efficiencies and higher power densities. This trend is driven by cost considerations (e.g. material economies), space limitations (e.g. in the automotive environment), and increasing efficiency requirements (e.g. for telecom applications). The increase of the power density often affects the efficiency, i.e. a trade-off between these two quality indices exists [4].

A higher switching frequency allows a reduction in the volume of passive components, such as inductive components. Inductive components occupy a significant amount of space in today's power electronic systems, and furthermore, considerable losses occur in these components. Particularly, today's increasing switching frequency leads to High Frequency (HF) losses that are difficult to determine. In order to increase the power density and/or efficiency of power electronic systems, losses in inductive components must be reduced, and/or new cooling concepts need to be investigated. For it, accurate loss and thermal models are crucial. There have been several publications focusing on modeling inductive components [5, 6, 7, 8, 9, 10]. The aim of this thesis is to improve the model accuracy. This is done by combining the best state-of-the-art approaches with newly-developed approaches.

## 1.1 Modeling of Inductive Power Components

Inductive components are widely used in power electronic applications. Three typical examples that employ inductive power components are illustrated in Figure 1.1. Figure 1.1(a) shows a buck converter with a typical inductor current/flux waveform in Continuous Conduction Mode (CCM). The current is, in case of a linear inductance  $L$ , proportional to the magnetic flux. The flux waveform has a triangular shape with a DC offset. The core losses are influenced by this DC pre-magnetization; this has been discussed in many previous publications [8, 11, 12, 13, 14, 15, 16]. Since data that shows the influence of a DC

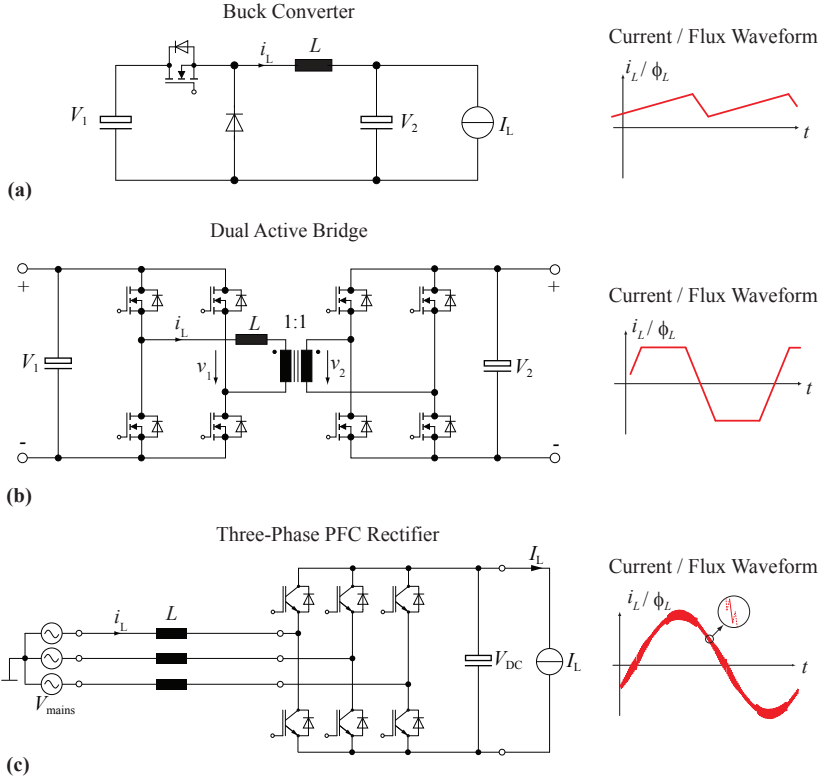


**Figure 1.1:** Applications of inductive power components: (a) inductor in buck converter, (b) inductor in Dual Active Bridge (DAB) converter, (c) boost inductors in three-phase PFC rectifier.

pre-magnetization to the core losses is normally not provided by core manufacturers, it is difficult to determine core losses under a DC bias condition.

In Figure 1.1(b) a Dual Active Bridge (DAB) with a typical inductor current/flux waveform for CCM is given. This flux waveform is typical for power electronic applications in general. In modern power electronic systems voltages across inductors or transformers generally show rectangular shapes, including periods of zero voltage. In most core loss models, the phase where the voltage across the magnetic component is zero (i.e. the flux remains constant) is not considered. It is implicitly

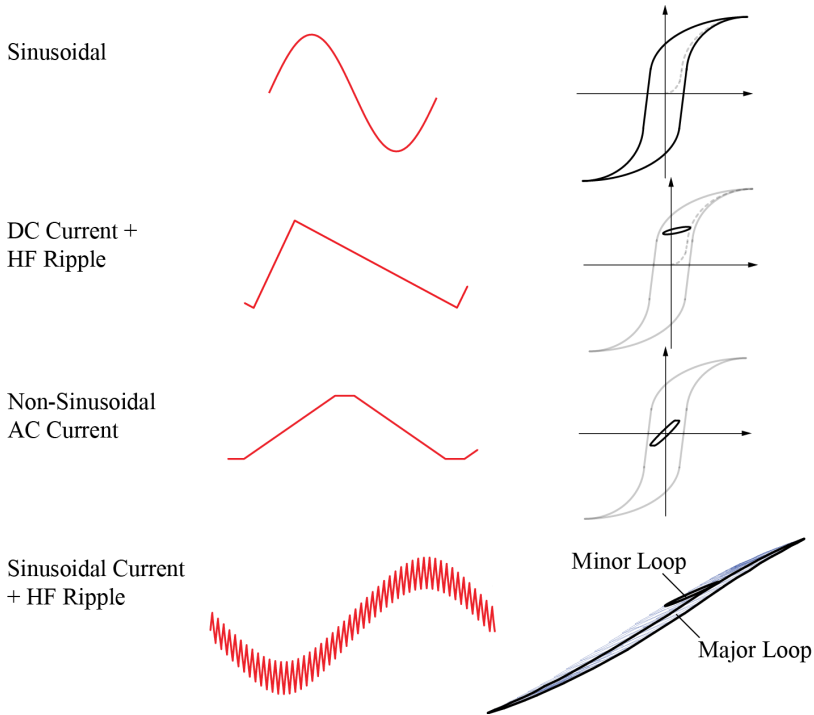


**Figure 1.2:** Overview of different typical flux waveforms.

assumed that no losses occur when the flux remains constant. However, as measurements show, this is not a valid simplification. At the beginning of a period of constant flux, losses still occur in the material. This is due to relaxation processes inside the magnetic material.

The third application is a three-phase PFC rectifier with three boost inductors (cf. Figure 1.1(c)). The flux waveform can be seen as a fundamental (sinusoidal) waveform and superimposed HF ripple. When plotting the traversed B-H-curve, one sees a large loop and many small loops, i.e. one large *major* loop and many small *minor* loops. The large loop originates in the fundamental waveform, while the small loops originate in the HF ripples.

The three flux waveforms discussed point out the main issues related to the impact of different flux waveform shapes on core losses. These three flux waveforms and a standard sinusoidal waveform are summa-

rized in Figure 1.2. In this thesis, different means of how to calculate core losses while addressing the above mentioned difficulties are derived. The Steinmetz Premagnetization Graph (SPG) that shows the dependency of the Steinmetz parameters ( $\alpha$ ,  $\beta$  and  $k$ ) on premagnetization is proposed. This permits the calculation of core losses under DC bias conditions. In order to model flux waveforms with periods of constant flux, a new core loss model that takes relaxation effects into consideration is derived. Furthermore, it is experimentally verified that the loss energy for each (minor or major) loop can be calculated independently and totaled. The flux waveform can be divided into its fundamental flux waveform and into piecewise linear flux waveform segments. The loss energy is then calculated for the fundamental and all piecewise linear segments, totaled and divided by the fundamental period length in order to determine the average core loss. Actually, when doing this, one does not consider how the minor loop closes: each piecewise linear segment is modeled as having half the loss energy of its corresponding closed loop.

In order to improve the model accuracy a loss database has been built up. The applied core loss approach can be seen as a hybrid of an improved version of the empirical Steinmetz equation and an approach based on a material loss database (loss map). In order to build the material loss database, core loss measurements have to be conducted. A particular focus is therefore placed on how core losses can be measured, and what measurements are necessary for accurate core loss modeling.

The situation concerning non-linear current waveforms is much simpler for winding losses. Due to the orthogonality of the cosine-function, it is acceptable to perform a Fourier expansion of the current, calculate the losses for each frequency component, and then total up the losses. This is not valid for core losses, since there is a non-linear relation between losses and (peak) flux density.

In addition to the impact of the current/flux waveform on core and winding losses, there are other issues, which make the modeling of inductive components challenging. The procedure to model inductive components can be structured as:

1. Set up a magnetic circuit model, i.e. a reluctance model.
2. Determine core losses.
3. Determine winding losses.

#### 4. Model the thermal behavior.

A magnetic circuit model is set up in order to calculate the inductance, predict the flux density in each section of the core, and model the effect of the air gap fringing field on winding losses. The flux density in each core section is important to calculate the core losses and to avoid saturation of the core. Despite its importance, a satisfying air gap reluctance model has not been found in literature. A new means to determine accurately the reluctances of air gaps is accordingly suggested. The approach is easy to handle as it is based on a modular concept where a simple basic geometry is used as a building block to describe different three dimensional air gap shapes.

In step two, the core losses are modeled. In addition to the issues of the impact of the flux waveform on core losses (see above), another aspect to be considered in core loss calculation is the effect of the core shape and size. By introducing a reluctance model of the core, and with it, calculating the flux density in every core section of (approximately) homogenous flux density, one can calculate the losses of each core section. The core losses of each section are then totaled to obtain the total core losses. This generally leads to a high accuracy. However, under certain circumstances, in tape wound cores a flux orthogonal to the tape layers can lead to high eddy currents and therewith to high core losses.

The second source of losses in inductive components is the ohmic losses in the windings. The resistance of a conductor increases with increasing frequency due to eddy currents. Self-induced eddy currents inside a conductor lead to the skin effect. Eddy currents due to an external alternating magnetic field, e.g. the air gap fringing field or the magnetic field from other conductors, lead to the proximity-effect. The skin-effect and proximity-effect losses can be calculated for round, litz, or foil windings; provided that the external field and the current are exactly known. However, the calculation of the external magnetic field strength, which has to be known when calculating the proximity losses, is challenging. In the case of an un-gapped core and windings that are fully-enclosed by core material, 1D approximations to calculate the magnetic field exist. However, in the case of gapped cores, such 1D approximations are not applicable as the fringing field of the air gap cannot be described in an 1D manner. This thesis applies a 2D approach in which the magnetic field at any position can be determined as superposition of the fields of each of the conductors. The impact

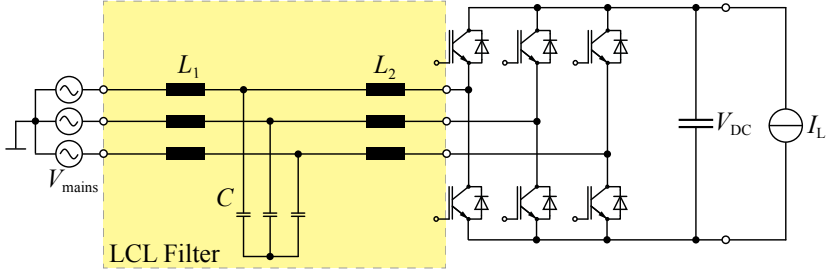


**Figure 1.3:** Three-phase PFC rectifier with LCL input filter.

of a magnetic conducting material can further be modeled with the *method of images*. The presence of an air gap can be modeled as a fictitious conductor carrying a current equal to the Magneto-Motive Force (MMF) across the air gap.

Finally, in step four, the thermal behavior of the inductive components must be determined. This is not only important to avoid overheating; it also has importance in modeling the losses correctly, as they are influenced by the temperature. As the temperature and losses are depending on each other, one has to iteratively perform the four steps until the problem converges.

## 1.2 Multi-Objective Optimization of Inductive Power Components

The loss models described in this thesis will form the basis for the optimization of inductive components. The focus of the last part of the thesis is placed on how to conduct a multi-objective optimization of inductive power components employed in power electronic applications. Using the example of an LCL input filter of a three-phase Power Factor Correction (PFC) rectifier, an inductive component design procedure based on a generic optimization approach, guaranteeing low volume and/or low losses, is proposed. The system considered is illustrated in Figure 1.3. Limiting factors for the filter design are the filter's maximum temperature and its maximum volume. The optimization procedure leads to different filter designs depending on whether the aim of the optimization is more on reducing the filter volume or more on reducing

the filter losses. In the selected example of an LCL input filter, a higher switching frequency leads to lower volume, or, when keeping the volume constant, to lower losses of the inductive components. However, higher semiconductor switching losses are expected in the case of higher switching frequencies. Therefore, an overall system optimization, i.e. an optimization of the complete three-phase PFC rectifier (not only the filter), is conducted. In so doing it is taken into account that in the design phase of any power electronics system, it is important to consider the system as a whole, as there are parameters that bring advantages for one subsystem but bring disadvantages for another.

### 1.3 Outline of the Thesis

In **Chapter 2** it is shown how to model inductive components using magnetic circuits. A magnetic circuit model enables a fast and straightforward inductance calculation. It also allows one to predict the flux density in each section of the core, thereby making it possible to calculate core losses and avoid saturation of the core when designing inductive components. Furthermore, when calculating winding losses the effect of the air gap fringing flux can be accurately modeled as a function of the Magneto-Motive Force (MMF) across the air gap. The air gap reluctance in a magnetic circuit model (or reluctance model) is by far the most difficult to calculate. An approach to accurately calculate the reluctance of an air gap has been developed in the course of this thesis.

In **Chapter 3** it is shown how core losses can be modeled accurately; thereby considering all different aspects of core loss modeling. The impact of peak-to-peak flux density, frequency, DC premagnetization, temperature, core shape, minor and major loops, flux waveform, and material on the core loss calculation are all considered. A high level of accuracy is achieved by combining the best state-of-the-art approaches and by embedding newly developed approaches into a new hybrid core loss calculation approach (Section 3.9). A special discussion is given about relaxation effects in magnetic materials. Additional losses may occur due to relaxation processes. A new core loss modeling approach that takes such relaxation effects into consideration has been developed in the course of this thesis and named the *improved-improved Generalized Steinmetz Equation*,  $i^2\text{GSE}$  (Section 3.6). Another fact that makes the prediction of core losses difficult is that core losses are influenced by

a DC premagnetization. The *Steinmetz Premagnetization Graph* (SPG) that shows the dependency of the Steinmetz parameters ( $\alpha$ ,  $\beta$  and  $k$ ) on premagnetization is introduced (Section 3.7). This permits the calculation of core losses under DC bias conditions. Other aspects that are discussed are how core losses are measured (Section 3.4 and Section 3.5) and how the core shape influences core losses (Section 3.10).

In **Chapter 4** the second source of losses in inductive components, the ohmic losses in the windings, are discussed. The skin effect and proximity effect losses can be calculated for foil (Section 4.4), round (Section 4.3), or litz wire (Section 4.3.5) windings; provided that the external field and the current are exactly known. An approach that also considers the air gap stray field in the calculation of the external field for the case of gapped cores is given.

In **Chapter 5** another important aspect in modeling inductive components, their thermal behavior, is introduced. This is not only important to avoid overheating, but also for correctly modeling the losses, as they are influenced by the temperature. It is shown how to calculate heat conduction, convection, and radiation in inductive components.

In **Chapter 6** experimental tests that confirm the overall accuracy are shown. It is shown that a high level of accuracy is achieved by combining all loss and thermal models introduced in this thesis. Furthermore, in order to handle the models and enable others to determine losses accurately, a *Magnetic Design Environment* has been implemented in the course of this thesis. A short overview is given in Section 6.1.

The last part of the thesis (**Chapter 7**) is about the multi-objective optimization of inductive power components. The design of inductive components will be illustrated using the example of LCL filters for three-phase PFC rectifiers. In the design phase all the loss and thermal models introduced will be used. The optimization procedure demonstrated leads to different filter designs depending whether the aim of the optimization is more on reducing the volume or more on reducing the losses. Furthermore, an overall system optimization, i.e. an optimization of the complete three-phase PFC rectifier including the filter, has been performed.

## 1.4 List of Publications

Different parts of this work have already been published or are being published in international journals or conference proceedings. These publications are listed below.

### Conference Papers

1. J. Mühlethaler, J. Biela, J. W. Kolar, and A. Ecklebe, *Core Losses under DC Bias Condition Based on Steinmetz Parameters*, Proc. of the IEEE/IEEJ International Power Electronics Conference (ECCE Asia), Sapporo, Japan, June 21-24, 2010.
2. J. Mühlethaler, J. Biela, J. W. Kolar, and A. Ecklebe, *Improved Core Loss Calculation for Magnetic Components Employed in Power Electronic Systems*, Proc. of the Applied Power Electronics Conference and Exposition (APEC), Fort Worth, TX, March 6-10, 2011.
3. J. Mühlethaler, J. W. Kolar, and A. Ecklebe, *A Novel Approach for 3D Air Gap Reluctance Calculations*, Proc. of the 8th International Conference on Power Electronics - ECCE Asia, The Shilla Jeju, Korea, May 30-June 3, 2011.
4. J. Mühlethaler, J. W. Kolar, and A. Ecklebe, *Loss Modeling of Inductive Components Employed in Power Electronic Systems*, Proc. of the 8th International Conference on Power Electronics - ECCE Asia, The Shilla Jeju, Korea, May 30-June 3, 2011.
5. C. Marxgut, J. Mühlethaler, F. Krismer, and J. W. Kolar, *Multi-Objective Optimization of Ultra-Flat Magnetic Components with a PCB-Integrated Core*, Proc. of the 8th International Conference on Power Electronics - ECCE Asia, The Shilla Jeju, Korea, May 30-June 3, 2011.
6. J. Mühlethaler, M. Schweizer, R. Blattmann, J. W. Kolar, and A. Ecklebe, *Optimal Design of LCL Harmonic Filters for Three-Phase PFC Rectifiers*, in Proc. of the IECON, Melbourne, November 7-10, 2011

7. B. Cougo, A. Tüysüz, J. Mühlethaler, and J.W. Kolar, *Increase of Tape Wound Core Losses Due to Interlamination Short Circuits and Orthogonal Flux Components*, in Proc. of the IECON, Melbourne, November 7-10, 2011.

### **Journal Papers**

8. J. Mühlethaler, J. Biela, J.W. Kolar, and A. Ecklebe, *Core Losses Under the DC Bias Condition Based on Steinmetz Parameters*, IEEE Transactions on Power Electronics, Vol. 27, No. 2, February 2012.
9. J. Mühlethaler, J. Biela, J.W. Kolar, and A. Ecklebe, *Improved Core-Loss Calculation for Magnetic Components Employed in Power Electronic Systems*, IEEE Transactions on Power Electronics, Vol. 27, No. 2, February 2012.



## Chapter 2

# Magnetic Circuit Modeling

In an analogous manner to Kirchhoff's voltage law, according to Ampere's law the sum of the magnetomotive force (MMF) in a magnetic circuit around a closed loop is zero. Gauss's law for magnetic circuits yields to the fact that the sum of magnetic fluxes into a node is zero, similar to Kirchhoff's current law. Furthermore, the reluctance  $R_m$  is defined as  $R_m = \text{MMF}/\Phi$ , where  $\Phi$  is the magnetic flux through the reluctance  $R_m$ . These analogies lead to the concept of magnetic circuits. The theory of magnetic circuits is, for instance, introduced in [5, 17].

A magnetic circuit model, also named simply *reluctance model*, of an inductive component enables a fast and straightforward inductance calculation. It also allows one to predict the flux density in each section of the core, thereby making it possible to avoid saturation of the core. Furthermore, when winding losses are calculated, the effect of the air gap fringing flux can be modeled accurately as a function of the Magneto-Motive Force (MMF) across the air gap [5]. The air gap reluctance must be known in advance for an accurate MMF calculation.

The inductance of an inductive component with  $N$  winding turns and a total magnetic reluctance  $R_{m,\text{tot}}$  is calculated as

$$L = \frac{N^2}{R_{m,\text{tot}}}. \quad (2.1)$$

The reluctance of each section of the flux path has to be calculated first

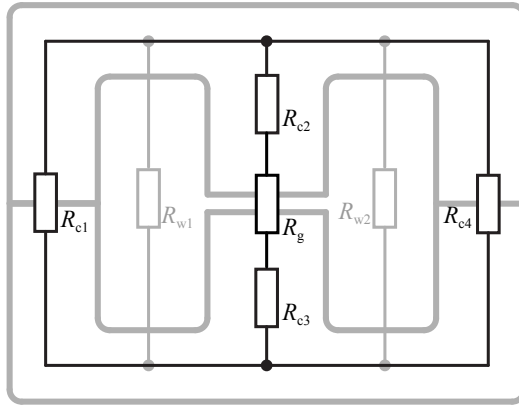


**Figure 2.1:** Illustration of a magnetic reluctance model for the example of an E-core.

in order to calculate  $R_{m,\text{tot}}$ . In Figure 2.1 such a reluctance model for the example of an E-core is illustrated. The calculation of the reluctance  $R_{ci}$  of the core sections is simple: for a core section of length  $l_c$ , cross-section  $A_c$ , and permeability  $\mu_r\mu_0$  it is

$$R_{ci} = \frac{l_c}{\mu_r\mu_0 A_c}. \quad (2.2)$$

Difficulties occur only in the corner sections. However, simple and reasonably accurate approximations for handling these sections exist. The reluctances  $R_{w1}$  and  $R_{w2}$  represent the flux paths that are not closed over the core and consequently reduce the total magnetic reluctance  $R_{m,\text{tot}}$ . These winding reluctances  $R_w$  are rather high and can be neglected in most practical cases. Dominant for the inductance value is the air gap reluctance  $R_g$ . Unfortunately, it is by far the most difficult to calculate; therefore, the focus of this chapter is on its calculation. Existing means of calculating the reluctance of air gaps are given in the following section, and, in Section 2.2, a new model to calculate the air gap reluctance is derived. Later, in Section 2.3, it is discussed how core reluctances can be calculated and in Section 2.4, to support the theoretical analysis, experimental results are given.

## 2.1 Existing Approaches for Air Gap Reluctance Calculation

Different means of calculating the reluctance of air gaps exist. Under the assumption of a homogenous flux density distribution in the air gap and no fringing flux, the air gap reluctance can be calculated as

$$R_g = \frac{l_g}{\mu_0 A_g}, \quad (2.3)$$

where  $l_g$  and  $A_g$  are the air gap length and air gap cross-section respectively, and  $\mu_0$  is the permeability of free space. Equation (2.3) is only accurate when the fringing flux is small compared to the total flux, i.e. when the air gap length is very small compared to the dimensions of the air gap cross-section.

Different approaches of how to take the fringing flux into consideration for calculating the air gap reluctance have been derived in the past. The approaches can be basically classified into three categories, which are discussed within Section 2.1.1, Section 2.1.2, and Section 2.1.3.

### 2.1.1 Method of the Conformal Schwarz-Christoffel Transformation

One approach to calculate analytically the reluctance of an air gap geometry is the method of the conformal Schwarz-Christoffel transformation [18, 19, 20]. The solutions described in [9, 21, 22] are based on this transformation. The approach of [21] is based on the capacitance-to-reluctance analogy for calculating the reluctance of air gaps: if air is the dielectric, the capacitance  $C$  can be expressed as

$$C = \epsilon_0 F(g), \quad (2.4)$$

where  $F(g)$  represents the geometry between plates of infinite conductivity and  $\epsilon_0$  is the permittivity of free space. The reluctance  $R_{m,airgap}$  of an air gap between surfaces of infinite permeability and with the same geometry  $F(g)$  is then

$$R_g = \frac{1}{\mu_0 F(g)}. \quad (2.5)$$

Hence, the calculation of the capacitance of the air gap geometry with help of the Schwarz-Christoffel transformation leads directly to the air

gap reluctance. However, in [21] only 2D considerations have been made, which considerably limits the practicability of this approach for real 3D air gaps.

Also in [9] the magnetic field is calculated via the Schwarz-Christoffel transformation, though without the capacitance-to-reluctance analogy. The three-dimensionality of air gaps has been taken into consideration. The solution of approach [9] leads to a relatively complex, difficult to handle, but accurate formula for the air gap reluctance.

### 2.1.2 Increase of the Air Gap Cross-Sectional Area

The fringing flux can be taken into consideration by increasing the actual air gap cross-sectional area (by increasing the air gap cross-sectional area the reluctance is reduced to the actual value) [22, 23, 24]. According to [23], 10% is a typical value by which the cross-sectional area has to be increased; however, it is admitted that the cross-sectional area should be increased as a function of the air gap length  $l_g$  and that a determination of the exact value by which the cross-sectional area has to be increased is difficult. In [24], the reluctance of an air gap with length  $l_g$ , width  $c$ , and depth  $t$  is calculated as

$$R_g = \frac{l_g}{\mu_0(c + l_g)(t + l_g)}. \quad (2.6)$$

No explanation or derivation of the equation is given. As will be shown later, the results deviate from comparison with FEM simulations. In [22] the effective semi-width of the gap, e.g. the radius in case of a round cross-section, is increased by the amount of

$$\left(0.241 + \frac{1}{\pi} \ln \frac{b_a}{l_g}\right) l_g, \quad (2.7)$$

where  $b_a$  is the total inside length of the leg containing the air gap, e.g. for a pot core  $b_a$  equals the width of the winding space. No derivation for the formula (2.7) is given. However, (2.7) can be derived from (2.8)<sup>1</sup> ((2.8) has not been explained yet but will be introduced in the next section). The approach of (2.7) is based on the method of the

---

<sup>1</sup> $\mu_0 \left[ \frac{w}{2l} + \frac{2}{\pi} \left( 1 + \ln \frac{\pi h}{4l} \right) \right]$  with  $l = l_g/2$  and  $h = b_a/2$  becomes  
 $\frac{2\mu_0}{l_g} \left[ \frac{w}{2} + \frac{l_g}{\pi} \left( 1 + \ln \frac{\pi b_a}{4l_g} \right) \right] = \frac{2\mu_0}{l_g} \left[ \frac{w}{2} + \left( 0.241 + \frac{1}{\pi} \ln \frac{b_a}{l_g} \right) l_g \right].$

conformal Schwarz-Christoffel transformation and is therefore a hybrid of the two categories. This approach is only capable of calculating the reluctances of air gaps with shapes as illustrated in Figure 2.2(a); for this particular air gap shape (air gap type 1/1; cf. next section) the solution of approach (2.7) and the solution obtained with the model that will be derived next are the same.

### 2.1.3 FEM Tuned Equations

A third class of approaches is based on equations with FEM tuned parameters for different air gap cases. For instance, an approach to derive the 3D reluctance from the 2D results of [21] has been made in [25]. For it, the corner reluctance of one air gap shape is described by an equation, in which a parameter has to be tuned by a 3D FEM simulation. The structure of the equation for the corner reluctance was found in [26]. The approach in [26] is a rough approximation based on geometrically constructed flux and equipotential lines of different given standard geometries. This rough approximation had then been improved in [25] by a FEM tuned parameter. Another approach to solve the problem with FEM tuned equations is given in [5, 27], where different two dimensional cases are modeled with FEM tuned equations. A corner reluctance is added as well in order to consider the 3D reluctance. Generally, a high accuracy can be achieved with FEM tuned equations as given in [25] or [5, 27]. However, in both approaches the added corner reluctance has more an approximative character and a different approach to consider the three-dimensionality would be interesting to have.

### 2.1.4 Desired Approach for Air Gap Calculations

An approach for an air gap calculation that is capable of calculating the reluctance and

- ▶ considers the three-dimensionality,
- ▶ is reasonably easy-to-handle,
- ▶ is capable of handling different shapes of air gaps, as e.g. the ones illustrated in Figure 2.2,
- ▶ and maintains a high accuracy,

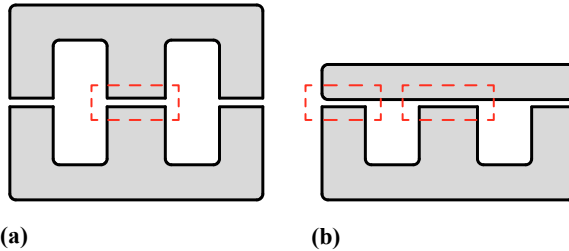


**Figure 2.2:** Illustration of different core shapes that lead to different air gap shapes.

is important to have. In the following, a new approach to calculate the air gap reluctance is derived. The approach is accurate because it is based on analytical field solutions.

## 2.2 Air Gap Reluctance

The novel approach for the 3D air gap reluctance calculation is derived from the example of air gaps with rectangular cross-section in Section 2.2.1. Later, in Section 2.2.2, it is described how to apply the approach to air gaps with round cross-sections.

### 2.2.1 Reluctance of Air Gaps with Rectangular Cross-Section

The reluctance of the simple basic geometry of Figure 2.3 is taken as a basis to calculate more complex air gap structures. This basic geometry is used as a building block to describe different three dimensional air gap shapes.

The geometry in Figure 2.3 has the 2D reluctance

$$R'_{\text{basic}} = \frac{1}{\mu_0 \left[ \frac{w}{2l} + \frac{2}{\pi} \left( 1 + \ln \frac{\pi h}{4l} \right) \right]}, \quad (2.8)$$

where the parameters are as illustrated in Figure 2.3. The 2D reluctance has the unit m/H and corresponds to the permeance per-unit-length. The derivation of (2.8) has been found in [21] and is given in Appendix A.1.

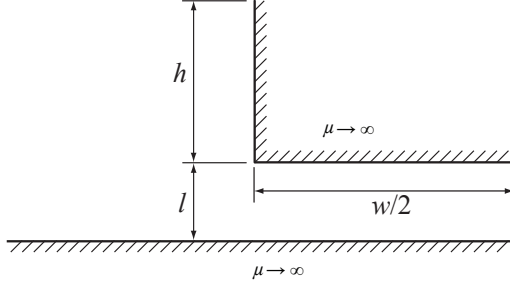


**Figure 2.3:** Basic geometry for air gap calculation.

Basically, one can think of three types of air gap shapes, which are illustrated in Figure 2.4. All air gap types can be seen as an assembly of several basic geometries of Figure 2.3. Figure 2.4 shows how to put together basic geometries to achieve the designated air gap type. In addition it shows how to set the values for  $w$  and  $l$  of (2.8). The value  $h$  represents the distance from the air gap edge to the next core corner, as e.g. illustrated in Figure 2.11. To clarify the idea, another illustration is given in Figure 2.5, where it is shown how to assemble several basic geometries in order to build an air gap type 2.

In order to consider the three dimensionality of air gaps, a fringing factor is introduced which describes by which factor the air gap reluctance decreases due to fringing flux comparing to the idealized reluctance of (2.3). This approach is introduced using the example of the air gap illustrated in Figure 2.7. The 3D air gap of Figure 2.7 is named a type 1/2 air gap, as it is based on an air gap type 1 ( $xz$ -plane) and an air gap type 2 ( $yz$ -plane). Under the assumption that the air gap is infinitely long in the  $x$ -direction ( $t \rightarrow \infty$ ), the fringing effects at the air gap boundaries in the  $x$ -direction can be neglected. This air gap has a cross-section as illustrated in Figure 2.4(b) (air gap type 2). The fringing factor that considers fringing effects in  $y$ -direction is determined by calculating the corresponding 2D air gap reluctance  $R'_{yz}$  (as illustrated in Figure 2.4(b)) and dividing it by the 2D reluctance that neglects any fringing effects:

$$\sigma_y = \frac{R'_{yz}}{\frac{a}{\mu_0 b}}. \quad (2.9)$$

The fringing factor  $\sigma_y$  now describes by which factor the air gap re-

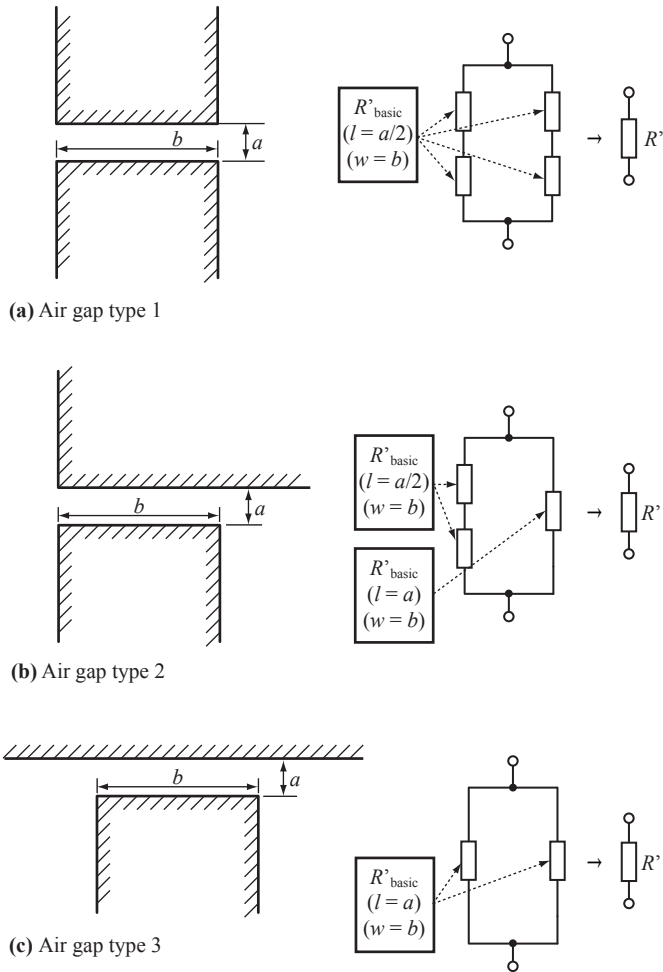


**Figure 2.4:** Different types of air gaps.

luctance decreases due to fringing flux in  $y$  direction comparing to the idealized reluctance of (2.3).

In a similar manner the fringing factor considering fringing effects in the  $x$ -direction can also be determined. Under the assumption that the air gap is infinitely long in the  $y$ -direction ( $b \rightarrow \infty$ ), the fringing effects

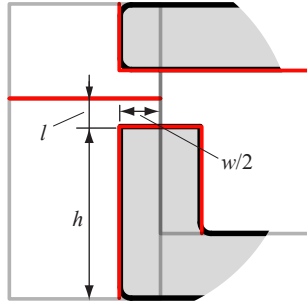


**Figure 2.5:** Illustration of how to assemble several basis geometries in order to build an air gap type 2.

at the air gap boundaries in the  $y$ -direction can be neglected. This air gap has a cross-section as illustrated in Figure 2.4(a) (air gap type 1). The fringing factor considering fringing effects in the  $x$ -direction is determined by calculating the corresponding 2D air gap reluctance  $R'_{xz}$  (as illustrated in Figure 2.4(a)) and dividing it by the 2D reluctance that neglects any fringing effects:

$$\sigma_x = \frac{R'_{xz}}{\mu_0 t}. \quad (2.10)$$

The fringing factor  $\sigma_x$  now describes by which factor the air gap reluctance decreases due to fringing flux in  $x$  direction comparing to the idealized reluctance of (2.3).

Now, after the two 2D fringing factors have been derived, it should be discussed how a 3D fringing factor can be derived from them. How this is done is illustrated in Figure 2.6. In a first step, the idealized equation of (2.3) is multiplied by the fringing factor  $\sigma_x$ . This can be interpreted as if the air gap cross-sectional area is multiplied by  $1/\sigma_x$  and a new cross-sectional area is calculated that allows the reluctance calculation with (2.3) and the consideration of the fringing flux in  $x$ -direction. An air gap with this new cross-sectional area and no fringing flux in  $x$ -direction has the same properties as the air gap with reduced size but fringing flux in  $x$ -direction. When this new cross-sectional area is now multiplied with  $1/\sigma_y$ , the fringing flux in  $y$ -direction is,

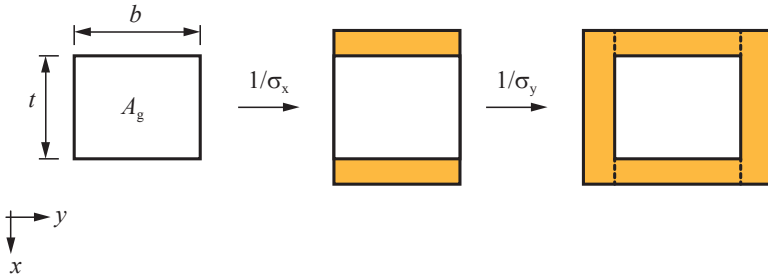


**Figure 2.6:** Illustration of how the 3D fringing factor is derived.

furthermore, taken into consideration. This is illustrated in the second transition of Figure 2.6. With the above steps, all fringing flux is taken into consideration.

As discussed above, the product of the fringing factors  $\sigma_x$  and  $\sigma_y$  shows by which factor the air gap reluctance decreases due to the total fringing flux comparing to the idealized reluctance of (2.3), i.e. the 3D fringing factor is derived as

$$\sigma = \sigma_x \sigma_y. \quad (2.11)$$

The reluctance of the air gap can then easily be calculated with (2.3) and (2.11)

$$R_{m,\text{airgap}} = \sigma \frac{a}{\mu_0 \cdot t \cdot b}. \quad (2.12)$$

The novel approach for reluctance calculations (2.12) has been compared to the approach of (2.6), and to the FEM tuned equation of [5, 27], and to 3D FEM simulations<sup>2</sup>. The results are given in Figure 2.8. The results are given normalized to the "classical" approach of (2.3), i.e. normalized to  $R_{\text{classic}}$ . The comparisons have been made for a type 1/1 air gap with fixed parameters (leg width and depth:  $w = 40$  mm, and distance between air gap and next core corner  $h = 60$  mm). With the FEM tuned equation of [5, 27] and the new model a high accuracy is achieved. At smaller air gaps the FEM tuned equation has a slightly higher accuracy (presumably this is the range at which the parameters have been tuned). The new model has, in return, a slightly higher accuracy at larger air gaps.

<sup>2</sup>FEM Software: Ansoft Maxwell 14.0

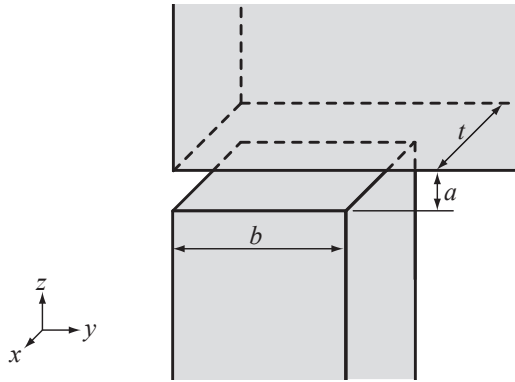


**Figure 2.7:** 3D air gap type 1/2, based on air gap type 1 ( $xz$ -plane) and air gap type 2 ( $yz$ -plane) of Figure 2.4.

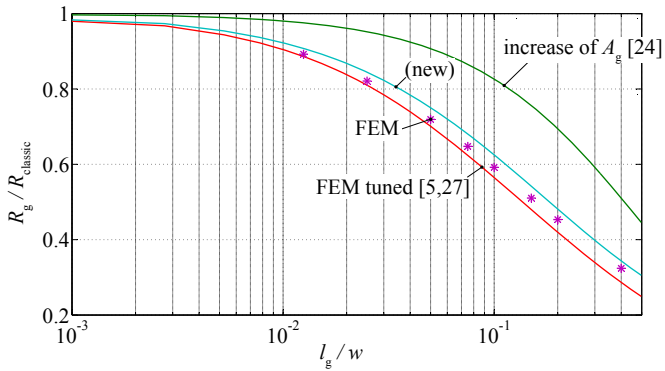


**Figure 2.8:** Comparison of air gap calculation approaches.

Type 1/2 and type 1/3 air gaps have been compared to FEM simulations as well: the maximum deviation of the new model has always been smaller than 6%.

## 2.2.2 Reluctance of Air Gap with Round Cross-Section

The fringing factor considering fringing effects in the  $r$ -direction (polar coordinate system) is

$$\sigma_r = \frac{R'}{\frac{a}{\mu_0 r}}, \quad (2.13)$$

where  $a$  is the air gap length,  $r$  the radius of the air gap, and  $R'$  represents the 2D air gap reluctance (this corresponds to the permeance per-unit-angle) of half of the core leg (including fringing effects). The accurate reluctance can then be calculated as

$$R_g = \sigma_r^2 \frac{a}{\mu_0 r^2 \pi}. \quad (2.14)$$

## 2.2.3 Adaptation of the Air Gap Reluctance Calculation Approach to Different Problems

Sometimes the geometry for which the air (gap) reluctance has to be calculated doesn't allow directly applying the novel calculation approach; however, in such cases the introduced approach can often be adapted to meet the problem. In the following this will be illustrated on one example, where the reluctance model of a PCB-integrated flyback transformer for a 1 mm thin PFC rectifier has been calculated.

In [28] the design and implementation of an PCB-integrated flyback transformer for a 1 mm thin PFC rectifier has been investigated. The ultra-flat core of the flyback transformer results in a considerable fringing flux. The setup investigated and the according reluctance model are shown in Figure 2.9. The air gap reluctances have been calculated as presented above. However, for  $b \gg a$  (cf. Figure 2.9) the window reluctances  $R_{m,\sigma}$  are not negligible anymore. Therefore, the flux through the window  $\Phi_\sigma$  has been calculated via window reluctances as illustrated in Figure 2.9. These window reluctances have been calculated with a fringing factor  $\sigma_x$  in order to consider the fringing flux in  $x$ -direction. The structure is an "air gap" type 1, as can be seen in the  $xz$ -plane. No other dimension for fringing calculation has to be considered. A high accuracy has been achieved. The interested reader is referred to [28] for more information.

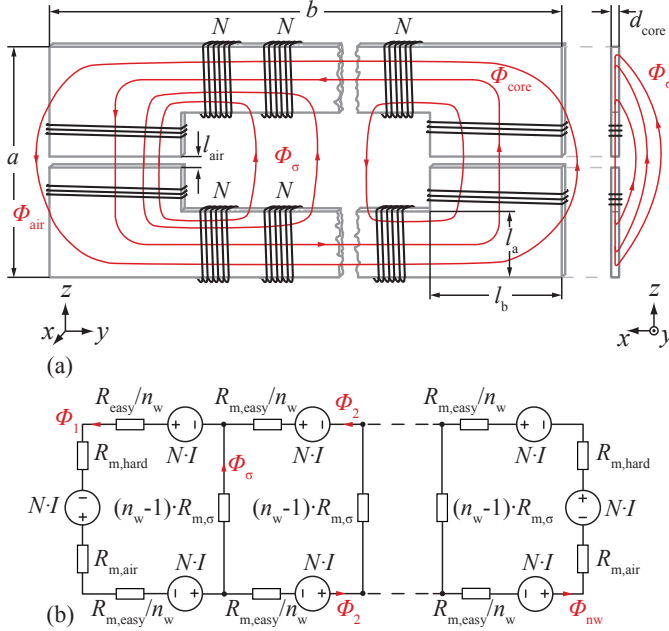


**Figure 2.9:** (a) Setup of a PCB-integrated inductor;  $n_w$  winding packages, each with  $N$  turns, are placed around the core in order to facilitate an interleaving with a secondary winding. The reluctances  $R_m$  between the long magnetic rods have to be considered in the inductance calculation as they have considerable impact on the inductance for long core lengths  $b$ . (b) Reluctance model of the setup presented in (a). Figure taken from [28].

## 2.3 Core Reluctance

In addition to the dominating air gap reluctance, the core reluctances have to be determined in order to achieve the complete reluctance model. The reluctance of a core section  $i$  can be calculated as

$$R_{Ci} = \frac{l_i}{\mu_0 \mu_r A_i}, \quad (2.15)$$

where  $l_i$  and  $A_i$  are the length and cross-section of section  $i$ . Hence, for every section the magnetic path length and the cross-sectional area have to be calculated first. This is difficult for corner sections. Practical

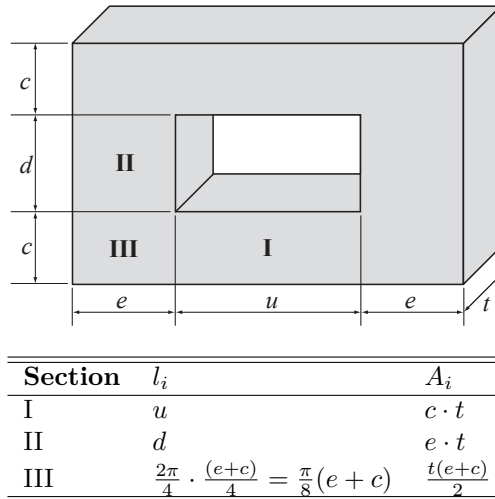


**Figure 2.10:** Approximations of core dimensions for core reluctance calculation [22].

cores have usually sharp corners, where the flux tends to concentrate on the inside the bend, so shortening the mean magnetic path.

Sophisticated ways of describing  $A_i$  and  $l_i$  of corner sections exist, e.g. introduced in [9]. However, it is unclear whether the difficult formulae of [9] lead to better results as they neglect the fact that the flux density concentrates mainly at the inner bend. In any case, the corners represent only a minor part of the core. Therefore, for this work the simple approximations from [22] have been taken. They are given in Figure 2.10.

The accuracy can be further improved by taking the non-linearity of the core material into consideration, i.e.  $\mu_r = f(H)$ . This is not straightforward: since the flux depends on the nonlinear B-H characteristics, not on a linearization of it represented by reluctance. This problem must be solved iteratively by using a numerical solving method, e.g. Newton's method.

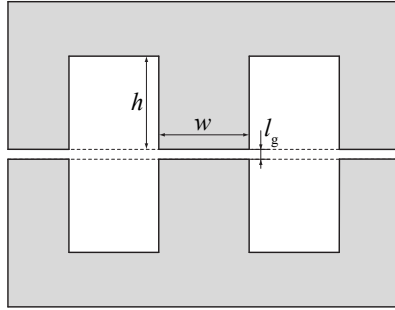


**Figure 2.11:** Built E core for inductance calculation and measurement comparison.

## 2.4 Experimental Results

This section presents some experimental results that illustrate well the accuracy that can be achieved.

### 2.4.1 Inductance

In Table 2.1 measurements and calculated inductance values  $L$  of an inductor built of two E-Cores (EPCOS ferrite N27; core E55/28/21 [29]; winding turns  $N = 80$ ) are given. The core has three air gaps of length  $l_g$  as illustrated in Figure 2.11. The inductances for different air gap lengths have been measured. The calculation has been performed with the idealized "classic" approach (2.3) and the newly derived approach (2.12). As can be seen, it is not appropriate to neglect the fringing flux; the classic approach leads to an underestimation of the inductance value. The calculation with the newly derived approach leads to accurate results.

### 2.4.2 Saturation

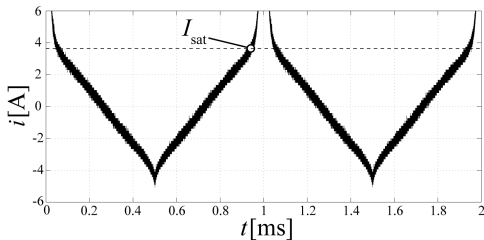
The saturation current  $I_{\text{sat}}$  is another very important design parameter. A current that is higher than the saturation current would result in a flux density above the saturation flux density  $B_{\text{sat}}$ . This would result in a substantial decrease of the relative permeability  $\mu_r$ , hence

**Table 2.1:** Measurement Results of E-Core

| Air Gap Length<br>$l_g$ | Calculated<br>classically (2.3) | Calculated with<br>new approach (2.12) | Measured |
|-------------------------|---------------------------------|--|----------|
| 1.0 mm                  | 1.42 mH                         | 1.97 mH                                | 2.07 mH  |
| 1.5 mm                  | 0.96 mH                         | 1.47 mH                                | 1.58 mH  |
| 2.0 mm                  | 0.72 mH                         | 1.22 mH                                | 1.26 mH  |

**Table 2.2:** Measurement Results of E-Core

|                  | Calculated<br>classically (2.3) | Calculated with<br>new approach (2.12) |
|------------------|---------------------------------|--|
| $L$              | 2.75 mH                         | 3.55 mH                                |
| $I_{\text{sat}}$ | 4.6 A                           | 3.6 A                                  |


**Figure 2.12:** Measurement of saturation current.

the inductance would drop. The saturation current can be calculated as

$$I_{\text{sat}} = \frac{B_{\text{sat}} A_e N}{L}. \quad (2.16)$$

An inductor built of two E-cores with an air gap in the center leg (EPCOS ferrite N27; core E55/28/21 [29]; air gap length  $l_g = 1$  mm; winding turns  $N = 80$ ) has been built. In Table 2.2, inductance values and saturation currents are given. The saturation flux density is taken from the data sheet B-H-curve [29] and is approximately  $B_{\text{sat}} = 0.45$  T at room temperature ( $25^\circ\text{C}$ ). The results can be compared to a mea-

surement for which the measured current waveform is given in Figure 2.12. A rectangular voltage waveform has been applied across the inductor to achieve this current waveform. The measured saturation current  $I_{\text{sat}}$  is approximately 3.7 A, which corresponds well to the calculated value.



# Chapter 3

## Core Loss Modeling

There are basically three physical core loss mechanisms: (static) hysteresis losses, eddy-current losses, and a third loss component which is often referred to as residual losses. Hysteresis losses are linear with the frequency  $f$  (rate-independent B-H loop). Eddy-current core losses occur because of an induced current due to the changing magnetic field and are strongly dependent on the material conductivity and the core geometry. The residual losses are, according to [30], due to relaxation processes: if the thermal equilibrium of a magnetic system changes, the system progressively moves towards the new thermal equilibrium condition. When the magnetization changes rapidly, as for example is the case in high-frequency or pulsed field applications, such relaxation processes become very important.

Core losses have to be described as a function of the peak-to-peak flux density  $\Delta B$ , frequency  $f$ , DC premagnetization  $H_{DC}$ , temperature, core shape, flux waveform, and material. This is not a simple task; predicting core losses is challenging. This chapter shows ways how a high accuracy in core loss modeling can be achieved.

In Section 3.1 physical origins of the core losses are summarized. In Section 3.2 state-of-the-art means of core loss modeling are shown. Later, in Section 3.3, needs for improvement are pointed out and novel models and approaches for core loss calculation that have been derived within the course of this thesis are outlined. A test system has been built to perform studies on core losses and to be able to fully characterize the loss behavior of different materials. The test system and

an accuracy analysis are given in Section 3.4 and Section 3.5. A loss model that allows one to consider relaxation effects in magnetic materials is introduced in Section 3.6. In Section 3.7 a graph is introduced that allows one to consider that core losses may vary under a DC bias condition when modeling core losses. Another important aspect of core loss modeling is how to consider the presence of major and minor loops; this is discussed in Section 3.8. In order to improve the model accuracy a loss database has been built up. The applied core loss approach can then be seen as a hybrid of an improved version of the empirical Steinmetz equation and an approach based on a material loss database (loss map). This hybrid core loss calculation approach is introduced in Section 3.9. Another aspect to be considered in core loss calculation is the effect of the core shape and size, which is discussed in Section 3.10.

### 3.1 Physical Origin of Core Losses

Diamagnetism, paramagnetism, ferromagnetism, anti-ferromagnetism and ferrimagnetism constitute five general groups into which materials can be classified according to their magnetic properties. Diamagnetic materials have a relative permeability  $\mu_r$  less than unity; paramagnetic materials have a relative permeability  $\mu_r$  greater than unity; however, both material groups have a relative permeability  $\mu_r$  close to unity. Antiferromagnetic materials behave similarly to paramagnetic materials; however, their underlying magnetic structure differs a lot from that of paramagnetic materials; hence they have a separate classification. Ferromagnetic and ferrimagnetic materials have a relative permeability  $\mu_r$  much higher than unity and therefore, these materials become very interesting for various technical applications. Ferromagnetic and ferrimagnetic materials are often named simply magnetic materials. Magnetic materials can be further divided into the two subgroups *soft* magnetic materials and *hard* magnetic materials, depending on the coercivity of the magnetic material, i.e. depending on the shape of the B-H loop. The coercivity  $H_c$  is defined as the magnetic field required to bring the magnetization of the material back to zero after the material has been saturated. A material with low coercivity is called a soft magnetic material, while a material with high coercivity is called a hard magnetic material. In this thesis, only soft magnetic materials are considered. Other materials, such as diamagnetic, paramagnetic, antiferromagnetic or hard magnetic materials are not discussed further.

The interested reader is referred to [31, 32] for more information about the different material groups.

The rotation of the electron around its nucleus as well as its spin result in a magnetic moment. The magnetic moment per unit volume is called the intensity of magnetization. In ferro- and ferrimagnetic materials, the atoms interact in a way that the materials show spontaneous magnetization at room temperature, i.e. the material sample is spontaneously magnetized even when no external field is applied. However, to keep the system in a minimum energy state, the sample is divided into (Weiss) domains of different magnetizing directions, that, together have a net magnetization of zero. In other words, although the material consists of magnetically saturated domains, the material sample has on a macroscopic scale a net magnetization of zero in the case that no external magnetic field is applied. These domains are separated by domain walls (or Bloch walls). In the case that an external magnetic field is applied to the material sample, the domain walls are shifted or the magnetic moment within domains change their direction; hence, the macroscopic net magnetization becomes greater than zero. The situations without an external field and the magnetizing process by the movement of the domain walls and the rotation of the magnetic moments due to an external applied field are illustrated in the Figure 3.1 (a) and (b) respectively. A very important material parameter of ferro- and ferrimagnetic materials is the Curie temperature  $T_{\text{Curie}}$  above which the material becomes paramagnetic (no spontaneous magnetization occurs anymore).

The magnetization process leads to a magnetization curve such as shown in Figure 3.2, where the magnetic flux density  $B$  versus the external applied magnetic field  $H$  is plotted. The flux change in the magnetic material is partly irreversible, i.e. energy is dissipated as heat. Even when the loop is traversed very slowly, i.e. in a quasistatic manner, losses occur. These losses originate in rapid jumps of the domain walls, the so called Barkhausen jumps. The large local flux changes due to Barkhausen jumps result in eddy currents that are located in the region of the jumps and, consequently, in losses. The energy per unit volume of a magnetic material with intensity of magnetization  $\mathbf{M}$  and external field  $\mathbf{H}$  is  $-\mathbf{H} \cdot \mathbf{M}$ . Consequently, the energy needed to change the intensity of magnetization from  $M_1$  to  $M_2$  is

$$W = \int_{M_1}^{M_2} \mathbf{H} d\mathbf{M}. \quad (3.1)$$

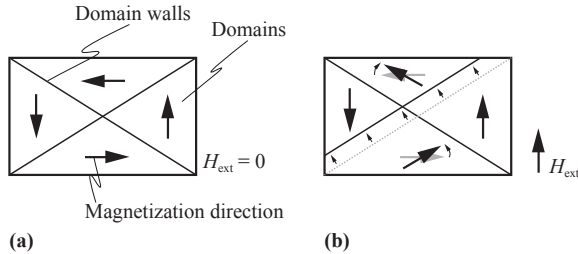


**Figure 3.1:** The magnetization process of a ferro- or ferrimagnetic sample: (a) illustration of domain walls in case no external field is applied; (b) illustration of the magnetizing process by the movement of the domain walls and the rotation of the magnetic moments due to an external applied field.

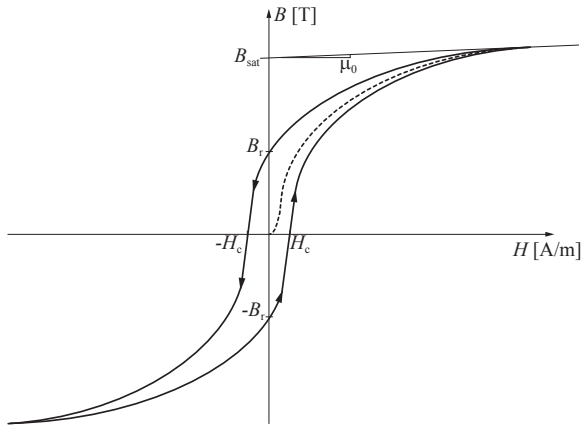


**Figure 3.2:** Typical magnetization curve (hysteresis loop) of a soft magnetic material.

If the process would be fully reversible, going from  $M_1$  to  $M_2$  and back would store potential energy in the magnetic material that is later released. In a plot similar to Figure 3.2, but with  $M$  instead of  $B$  for the ordinate scale, the area of the enclosed loop would be zero. However, as the process is partly irreversible, in reality a hysteresis loop with an area representing the energy loss per cycle appears. Since  $\oint H dH = 0$ ,

the loss energy per closed loop can be written as

$$W = \oint \mathbf{H} \, d\mathbf{B}, \quad (3.2)$$

i.e. the area of the closed loop in Figure 3.2 represents the energy per unit volume that is dissipated as heat when going around the loop.

It is important to note that the losses due to eddy currents that are induced around Barkhausen jumps are not the ones commonly named eddy-current core losses. The term "eddy-current core losses" has a different meaning. Eddy-current core losses are referred to the losses that originate from Maxwell's equation when the presence of magnetic domains is ignored, i.e. only the macroscopic net magnetization is considered. A discussion about different issues to be considered about (classic) eddy-current core losses is given in Section 3.10.3. Residual losses are another loss phenomenon. These losses are, according to [30], due to relaxation processes inside the magnetic material; state-of-the art models normally neglect effects related to relaxation phenomena. These losses will be discussed in Section 3.6 and a new core loss modeling approach that takes relaxation effects into consideration is introduced. The discussion above about physical origins of core losses builds a brief summary from [5, 30, 31, 32, 33]. The interested reader is referred to these references for more information about the physics of core losses.

## 3.2 Existing Approaches for Core Loss Calculation

The most used equation for characterizing core losses is the empirical power equation [22]

$$P_v = k f^\alpha \hat{B}^\beta \quad (3.3)$$

where  $\hat{B}$  is the peak induction of a sinusoidal excitation with frequency  $f$ ,  $P_v$  is the time-average power loss per unit volume, and  $k$ ,  $\alpha$ ,  $\beta$  are material parameters that have to be empirically determined. The equation is called the Steinmetz Equation (SE). The material parameters  $k$ ,  $\alpha$ , and  $\beta$  are accordingly referred to as the Steinmetz parameters. They are valid for a limited frequency and flux density range. Core manufacturers often provide data of losses per volume (or per weight) as a function of frequency  $f$ , flux density  $\hat{B}$ , and temperature. The Steinmetz parameters can be extracted out of this data. Sometimes, the

Steinmetz parameters are quoted. However, the SE is, in many circumstances, not capable of accurately calculating core losses because

- ▶ the material is usually exposed to non-sinusoidal flux waveforms in power electronic applications,
- ▶ and a potential DC premagnetization  $H_{DC}$  is not considered.

Different approaches have been developed to overcome this limitation and determine losses for a wider variety of waveforms. The approaches can be classified into the following categories:

1. Improvements of the Steinmetz equation (3.3): for instance, the analysis in [11] is motivated by the fact that the loss due to domain wall motion has a direct dependency of  $dB/dt$ . As a result, a modified Steinmetz equation is proposed. In [34] the approach is further improved and in [35] a method how to deal with minor hysteresis loops is presented and some minor changes to the equation are made. The approach of [11], [34], and [35] leads to the improved Generalized Steinmetz Equation (iGSE)

$$P_v = \frac{1}{T} \int_0^T k_i \left| \frac{dB}{dt} \right|^\alpha (\Delta B)^{\beta-\alpha} dt \quad (3.4)$$

where  $\Delta B$  is the peak-to-peak flux density and

$$k_i = \frac{k}{(2\pi)^{\alpha-1} \int_0^{2\pi} |\cos \theta|^\alpha 2^{\beta-\alpha} d\theta}. \quad (3.5)$$

The parameters  $k$ ,  $\alpha$ , and  $\beta$  are the same parameters as used in the Steinmetz equation (3.3). By use of the iGSE losses of any flux waveform can be calculated, without requiring extra characterization of material parameters beyond those for the Steinmetz equation. This approach is widely applied [6, 36]. If one inserts a sinusoidal flux density waveform into the iGSE, (3.4) transforms back to the Steinmetz equation (3.3). This is shown in Appendix A.2.

2. Calculation of the losses with a loss map that is based on measurements. This loss map stores the loss information for different operating points, each described by the flux density ripple  $\Delta B$ , the frequency  $f$ , the temperature, and a DC bias  $H_{DC}$  (e.g. in [37, 38, 39]).

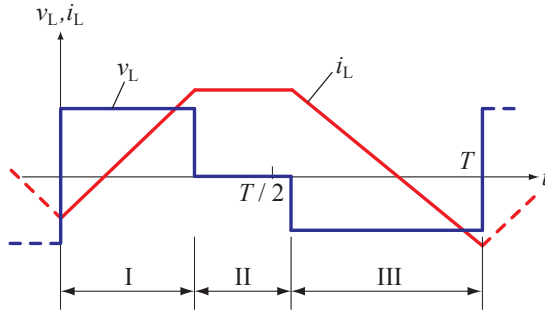


**Figure 3.3:** Typical voltage/current waveform of magnetic components employed in power electronic systems. Phase I: positive voltage; phase II: zero voltage; phase III: negative voltage.

3. Methods to determine core losses based on breaking up the total loss into loss components, i.e. static hysteresis losses, classical eddy current losses, and residual losses [30, 33, 40].
4. Hysteresis models such as Preisach and Jiles-Atherton used for calculating core losses.

The approaches of loss separation (category 3) and hysteresis models (category 4) have a practical disadvantage: such models are based on parameters which are not always available and are difficult to extract. However, the approach of loss separation has its relevance, as it gives a deeper understanding about physical core loss mechanisms. In the categories 1 and 2 an energy loss is assigned to each section of the voltage / current waveform as illustrated in Figure 3.3 (e.g. via an equation as (3.4) or via a loss map), and these losses are summed up to calculate the power loss occurring in the core. In the course of this thesis, an approach that can be seen as a hybrid of an improved version of the empirical Steinmetz equation (category 1) and an approach based on a loss map (category 2) has been developed; hence, the main focus is placed on these categories. However, to physically justify the models, the approach of loss separation (category 3) will be often referred to.

### 3.3 Outline of Novel Core Loss Calculation Models and Approaches

Existing core loss models have been summarized in the previous section. This section now points out unconsidered effects related to core losses modeling; and an outline of novel core loss calculation models and approaches, that have been derived in the course of this thesis, is given.

In modern power electronic systems voltages across inductors or transformers generally show rectangular shapes, including periods of zero voltage. In most core loss models, the phase where the voltage across the magnetic component is zero (i.e. the flux remains constant) is not discussed. It has been implicitly assumed that no losses occur when the flux remains constant. However, as measurements show, this is not a valid simplification. In phases of constant flux, losses still occur in the material. In the publication [41] about core loss modeling, a loss increase during zero voltage periods has been observed; but no explanation or modeling approach is given. Losses still occur a short period after switching the winding voltage to zero due to magnetic relaxation. A further improvement of the iGSE that takes this effect into consideration is suggested in Section 3.6. The new model is named the improved-improved Generalized Steinmetz Equation, or simply i<sup>2</sup>GSE. The model equation is

$$P_V = \frac{1}{T} \int_0^T k_i \left| \frac{dB}{dt} \right|^\alpha (\Delta B)^{\beta-\alpha} dt + \sum_{l=1}^n Q_{rl} P_{rl}, \quad (3.6)$$

where  $P_{rl}$  is calculated for each stepped voltage change according to

$$P_{rl} = \frac{1}{T} k_r \left| \frac{dB(t)}{dt} \right|^{\alpha_r} (\Delta B)^{\beta_r} \left( 1 - e^{-\frac{t}{\tau}} \right), \quad (3.7)$$

and  $Q_{rl}$  is a function that further describes the voltage change and is

$$Q_{rl} = e^{-q_r \left| \frac{dB(t_+)/dt}{dB(t_-)/dt} \right|}, \quad (3.8)$$

and  $\alpha$ ,  $\beta$ ,  $k_i$ ,  $\alpha_r$ ,  $\beta_r$ ,  $k_r$ ,  $\tau$ , and  $q_r$  are material parameters.

The approach of (3.6) attempts to solve the problem of different flux shapes. However, (3.6) does not consider a potential DC premagnetization  $H_{DC}$ . For many materials, the impact of a DC bias cannot be

neglected as it may increase the losses by a factor of more than two. An approach to describe core losses under DC bias condition is introduced in Section 3.7: a graph that shows the dependency of the Steinmetz parameters ( $\alpha$ ,  $\beta$  and  $k_i$ ) on premagnetization is proposed. The graph is named the Steinmetz Premagnetization Graph, SPG. This graph enables the calculation of losses via the Steinmetz equation (3.3), the iGSE (3.4), or the i<sup>2</sup>GSE (3.6) using appropriate Steinmetz parameters.

A core loss calculation with the models i<sup>2</sup>GSE and SPG described above has one major drawback: the models are based on parameters that cannot be extracted from the data provided by the core manufacturers. Until core manufacturers provide data to extract the dependency of a DC bias, e.g. an SPG, or provide data with which to predict relaxation effects, e.g. relaxation parameters  $\alpha_r$ ,  $\beta_r$ ,  $k_r$ ,  $\tau$ , and  $q_r$  (3.7) and (3.8), core loss measurements must be performed for an accurate core loss calculation. The measurement results could be stored in a core material database, which enables one to consider all the effects described above when designing inductive components. This is one aim of this thesis: to determine a structure for a core material database (later named loss map) to permit accurate core loss calculations. The novel structure is given in Section 3.9.

However, for the purpose of the above introduced studies a core loss measurement test setup has been built and is described next in Section 3.4.

## 3.4 Test Setup to Measure Core Losses

To perform measurements, the best measurement technique has to be selected first. In [42] different methods are compared. The B-H Loop Measurement has been evaluated as the most suitable. Amongst other advantages, this technique offers rapid measurement (compared to other methods, e.g. calorimetric measurement), copper losses are not measured, and a good accuracy. In Section 3.5 the accuracy is analyzed in detail. The principles are as follows: two windings are placed around the Core Under Test (CUT). The sense winding (secondary winding) voltage  $v$  is integrated to sense the core flux density  $B$

$$B(t) = \frac{1}{N_2 \cdot A_e} \int_0^t v(\tau) d\tau \quad (3.9)$$

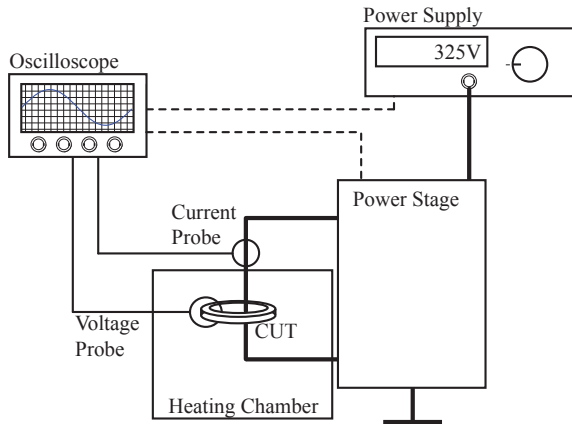


**Figure 3.4:** Overview of the test system.

|                        |                                      |
|------------------------|--------------------------------------|
| <b>Oscilloscope</b>    | LeCroy WaveSurfer 24MXs-A            |
| <b>Current Probe</b>   | LeCroy AP015                         |
| <b>Heating Chamber</b> | Binder ED53                          |
| <b>Power Supply</b>    | Xantrex XTR 600-1.4                  |
| <b>Power Stage</b>     | 0 – 450 V<br>0 – 25 A<br>0 – 200 kHz |

**Table 3.1:** Measurement Equipment

where  $N_2$  is the number of sense winding turns and  $A_e$  the effective core cross section of the CUT. The current in the excitation winding (primary winding) is proportional to the magnetic field strength  $H$

$$H(t) = \frac{N_1 \cdot i(t)}{l_e} \quad (3.10)$$

where  $N_1$  is the number of excitation winding turns and  $l_e$  the effective magnetic path length of the CUT. The loss per unit volume is then the

enclosed area of the B-H loop, multiplied by the frequency  $f$ <sup>1</sup>

$$\frac{P}{V} = f \oint H dB. \quad (3.11)$$

The selected approach is widely used [35, 38, 43, 44]. The test system consists of an oscilloscope, a power supply, a heating chamber, and a power stage, as illustrated in Figure 3.4. It is controlled by a MATLAB program running on the oscilloscope under Microsoft Windows. In Table 3.1 the used equipment is listed. In Figure 3.5 a photograph **(a)** and the simplified schematic **(b)** of the power stage is shown. The power stage has been designed and built in the course of this thesis. In Table 3.2 the most important components employed in the power stage are listed. The power stage is capable of a maximal input voltage of 450 V, output current of 25 A and a switching frequency of up to 200 kHz. With the power stage, it is possible to achieve rectangular voltage shapes (including phases of zero voltage) across the CUT that leads to triangular or trapezoidal current shapes including DC bias (if desired). This behavior is illustrated in Figure 3.6. To control the DC current, the current is sensed by a DC current transducer. A low frequency sinusoidal excitation is also possible; for this an output filter has been designed to achieve a sinusoidal current/voltage shape for frequencies up to 1 kHz.

## 3.5 Accuracy of the Measurement System

The different aspects that influence the accuracy of the measurements are given in the following.

---

<sup>1</sup>The core loss per unit volume is

$$\begin{aligned} \frac{P}{V} &= \frac{f \int_0^T i_1(t) \frac{N_1}{N_2} v_2(t) dt}{A_e l_e} = \frac{f \int_0^T H(t) l_e A_e \frac{dB(t)}{dt} dt}{A_e l_e} \\ &= f \int_{B(0)}^{B(T)} H(B) dB = f \oint H dB, \end{aligned}$$

where  $\frac{N_1}{N_2} v_2(t)$  is the sense winding voltage transformed to the primary side.

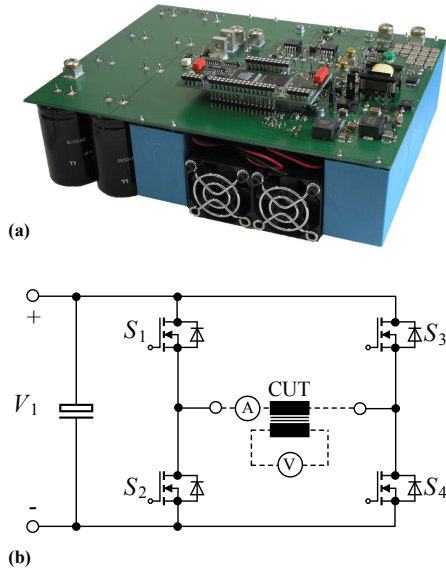


Figure 3.5: Power stage (a) photograph, (b) simplified schematic.

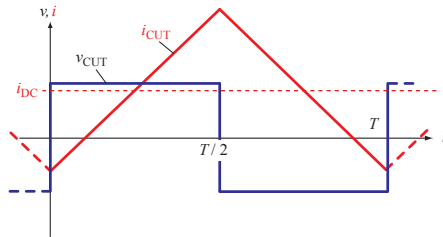


Figure 3.6: Current and voltage waveforms of the CUT.

|                       |   |
|-----------------------|---|
| <b>Power MOSFETs</b>  | IXYS IXFB82N60P   |
| <b>Gate Driver</b>    | IXYS IXDD414SI  |
| <b>Capacitors</b>     | Electrolytic: 2.75 mF<br>Foil: 360 $\mu$ F<br>Ceramic: 3.86 $\mu$ F |
| <b>DSP</b>            | TI TMS320F2808  |
| <b>Current Sensor</b> | LEM LTS 25-NP   |
| <b>Fan</b>            | San Ace 40 GE   |

Table 3.2: Power stage components.

### 3.5.1 Phase Shift Error of Voltage and Current Measurement

The error due to an inaccurate measurement of the voltage and current phase displacement can be quantified as [45]

$$E = 100 \cdot \frac{\cos(\zeta + \phi) - \cos \zeta}{\cos \zeta}, \quad (3.12)$$

where  $E$  is the relative error in % of the measured core losses,  $\zeta$  is the actual phase shift between the sense winding output voltage and the excitation winding current, and  $\phi$  is the error in the measurement of  $\zeta$ . Measurements have shown that  $\phi$  (over some frequency range) depends linearly on the frequency. In other words,  $\phi$  originates from a delay time  $T_d$  that is independent of the frequency. This delay time  $T_d$  can be measured with a rectangular current shape through a low inductance shunt, and with it the delay time can be compensated. The main cause of the delay time  $T_d$  is the current probe.

Different measurements with the material ferrite N87 from EPCOS (core part number: B64290L22X87) are presented in this thesis; therefore a short discussion about phase shift accuracy is given using the example of this core. This accuracy discussion is similar to the discussion presented in [12]. In Figure 3.7 a simplified equivalent circuit of the Core Under Test (CUT) is given. Winding losses and leakage inductance are assumed to be negligible. The reactance  $X_m$  can be calculated as

$$X_m = \omega A_L N_1^2, \quad (3.13)$$

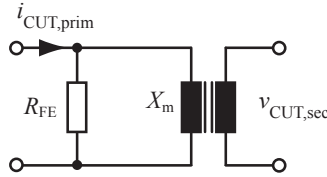


**Figure 3.7:** Equivalent circuit of the CUT.

where  $A_L$  is the inductance factor,  $N_1$  is the number of primary winding turns, and  $\omega = 2\pi f$  is the angular frequency. Hence, for the CUT ( $A_L = 2560$  nH [29],  $N_1 = 10$ ) and a frequency  $f = 100$  kHz the reactance is  $X_m = 160.8 \Omega$ . At the operating point  $\Delta B = 100$  mT (peak-to-peak),  $f = 100$  kHz, and  $T = 40^\circ\text{C}$  losses of  $P_{\text{Loss}} = 0.2$  W are expected (from material data sheet [29]). With this information, the equivalent resistor  $R_{\text{FE}}$  that represents the core losses can be calculated

$$R_{\text{FE}} = \frac{V_{\text{rms}}^2}{P_{\text{Loss}}} = \frac{\left(N_1 A_e \omega \frac{\Delta B}{2\sqrt{2}}\right)^2}{P_{\text{Loss}}}, \quad (3.14)$$

where  $A_e$  is the effective core cross section. For the CUT and operating point, the resistor  $R_{\text{FE}}$  is  $2.26$  k $\Omega$ . Now, the angle  $\zeta$  can be calculated as

$$\zeta = \arctan \frac{R_{\text{FE}}}{X_m} = 85.9^\circ. \quad (3.15)$$

An uncompensated delay time  $T_d$  would result in a phase shift error of voltage and current measurement of

$$\phi = f \cdot T_d \cdot 360^\circ. \quad (3.16)$$

When (3.16) is inserted in (3.12) and then solved for  $T_d$ , a tolerable uncompensated delay time for a desired accuracy is derived; e.g. for an accuracy of  $\pm 3\%$ , an uncompensated delay time of  $\pm 3.5$  ns at  $100$  kHz and  $\zeta = 85.9^\circ$  would be tolerable. Measurements have shown that the delay time compensation leads to lower residual delay times; although a quantification is difficult. With a realistic delay time compensation to an accuracy of  $\pm 1.5$  ns, and with an expected system accuracy (only phase shift consideration) of  $\pm 4\%$ , measurements of materials up to an angle of  $\zeta = 88.7^\circ$  (at  $f = 100$  kHz) can be performed. For lower frequency measurements the permitted angle  $\zeta$  increases for the same

accuracy constraint; e.g. at 20 kHz, for an accuracy of  $\pm 4\%$ , measurements up to an angle of  $\zeta = 89.7^\circ$  are permitted. All measurements presented in the next sections are within this range.

The system has one drawback related to the phase shift: the measurement of gapped cores (or low permeability cores) is difficult because the angle  $\zeta$  substantially increases in this situation. A detailed analysis together with a new method of how gapped cores could be measured is introduced in [13]. Two measurement methods that improve core loss measurement for very high frequencies (up to 70 MHz) are proposed in [46] and [47]. Although the focus of [46] and [47] are on measurements at very high frequencies, the method could be used to improve the loss measurement of gapped cores.

### 3.5.2 Equipment Accuracy

A typical magnitude/frequency characteristic of the current probe has been provided by the current probe manufacturer LeCroy, from which an AC accuracy of 3% could be extracted. Together with the accuracy of the passive probe (attenuation accuracy of 1%) and the accuracy of the oscilloscope itself (1.5% that originates amongst others from the limited vertical resolution of 8 bit), an equipment accuracy of  $\leq |\pm 5.6\%|$  is calculated.

### 3.5.3 Capacitive Coupling

Capacitive currents may result in errors and must therefore be avoided. The typical capacitances that are present in windings are

- ▶ capacitance between the primary and secondary winding (inter capacitance),
- ▶ self capacitance between turns of a winding (intra capacitance),
- ▶ and capacitance between the windings and the magnetic core.

Generally, the inter and intra capacitances increase with increasing area between the windings and decrease with distance between the windings. To decrease the inter capacitance, a separation of the primary and secondary windings is favorable; although a separation of the windings avoids an absolutely uniform winding distribution around the core (ideally, the primary winding should be distributed uniformly around the

core to achieve a homogenous flux density distribution). Another important aspect of the winding arrangement is the chosen number of turns of the primary winding. Even with the use of favorable winding layout, some ringing in current and voltage is inevitable. Fewer turns are more favorable for two reasons: this additionally decreases parasitic capacitances, and, because the current for the same magnetic operating point is higher, capacitive currents are relatively lower compared to (desired) inductive currents.

### 3.5.4 Temperature

An important aspect is that the temperature of the CUT is defined and constant. To keep the temperature constant, the test system performs the measurement automatically (starts excitation, controls current, regulates flux ( $\Delta B$ ), triggers the oscilloscope, reads values). With such an automated measurement system, a working point is rapidly measured and the losses do not heat the core in the short measurement period.

### 3.5.5 Comparative Measurement and Conclusion

Comparative measurements with the power analyzer *Norma D6100* have been performed to confirm the accuracy. The power analyzer is connected to measure the excitation winding current and the sense winding voltage to obtain the core losses [42]. The results in the performed working points matched very well. The deviation between the results of the test system and of the power analyzer was always  $\leq |\pm 4\%|$  (measured up to 100 kHz).

From the equipment accuracy ( $\leq |\pm 5.6\%|$ ) and the phase shift accuracy ( $\leq |\pm 4\%|$ ), a system accuracy of  $\leq |\pm 9.8\%|$  is calculated. However, based on the results of the comparative measurements, it can be said that the accuracy achieved is higher.

As a conclusion, a test system has been built up that performs the measurements quickly and leads to sufficiently accurate results.

## 3.6 Relaxation Effects in Magnetic Materials

In modern power electronic systems, voltages across inductors or transformers generally show rectangular shapes, including periods of zero

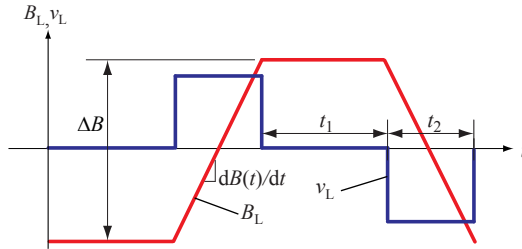


**Figure 3.8:** Voltage and flux density waveforms.

voltage. In most core loss models, the phase where the voltage across the magnetic component is zero (i.e. the flux remains constant) is not discussed. It has been implicitly assumed that no losses occur when the flux remains constant. However, as measurements show, this is not a valid simplification. As already mentioned in Section 3.3, during phases of constant flux (i.e. where the voltage across the magnetic component is zero) losses still occur in the core material. A literature survey led to the hypothesis that this is due to relaxation processes in the magnetic core material. In this section, first, measurements are presented that illustrate magnetic relaxation. Further, an attempt to theoretically explain the effect is given, and, with it, the resulting shape of a B-H loop for a trapezoidal flux waveform is analyzed.

### 3.6.1 Measurement Results

According to (3.4), the energy loss would only depend on the magnitude and the slope of the flux, and consequently, there should be no loss during periods of constant flux (zero voltage). Measurements on waveforms as illustrated in Figure 3.8 have been performed to investigate this. Figure 3.9 shows the corresponding measurement results. The CUT is made of ferrite EPCOS N87 (size R42). According to (3.4), the duration of  $t_1$  should not influence the *energy* loss per cycle, but, as can be seen, increasing  $t_1$  has a substantial influence on the energy loss per cycle. In particular, a change in  $t_1$  at low values of  $t_1$  influences the dissipated loss. For larger values of  $t_1$ , the core material has time to reach its equilibrium state and no increase in losses can be observed when  $t_1$  is increased further.

Different experiments have been conducted to confirm that this ef-

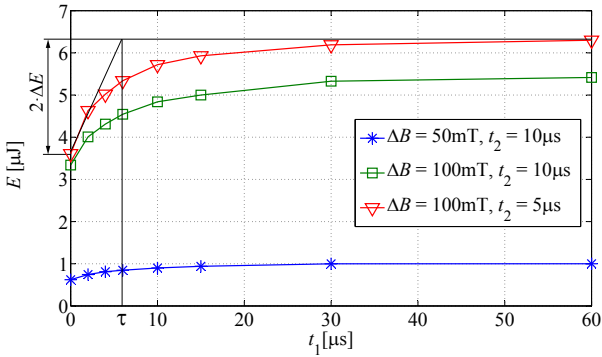


**Figure 3.9:** Measurement results for ferrite EPCOS N87 (R42, B64290L22X87 [29]); temperature = 25 °C. It is further illustrated how  $\tau$  according to (3.28) can be extracted.

fect is not due to an imperfection of the measurement setup. One could mainly think of two sources of error:

1. The effect of a small exponential change of current due to a residual voltage across the inductor in the "zero" voltage time intervals, i.e. an effect related to the CUT excitation.
2. An error in measurements due to limited measurement capabilities of the probes, i.e. an effect related to the measurement equipment used.

The following experiments have been conducted to make sure that none of these error sources led to the observed loss increase:

1. A resistor has been connected in series with the primary winding, i.e. the effect of an exponential change of the current due to a voltage drop across the inductor in the "zero" voltage time intervals has been deliberately increased. A resistor of 10  $\Omega$  has been chosen as this value is certainly higher than the residual resistance of the setup (for instance, the on-resistance of one MOSFET (IXYS IXFB82N60P) is only  $R_{\text{DS(on)}} = 75 \text{ m}\Omega$  at  $T_j = 25 \text{ }^\circ\text{C}$ ;  $I_D = 41 \text{ A}$ ). The excitation voltage has been accordingly adjusted to have the same magnetic operating point. The same core loss increase in the "zero" voltage time interval has been observed as without an

additional resistor, which indicates that the effect is not coming from an improper CUT excitation.

2. The current probe LeCroy AP015 has, with 50 MHz, the lowest bandwidth of the measurement equipment used. This is enough to measure the effect observed in Figure 3.9. Generally, according to the accuracy analysis in Section 3.5, accurate measurement results are expected for operating points with frequencies / flux densities such as presented in Figure 3.9. However, to confirm this, a simple comparative measurement has been performed to verify that the effect is not originating in the limitations of the voltage and current probes. For a limited temperature range it can be approximated that the relative change of the core temperature is proportional to the losses occurring in the core. According to this, the core losses can be observed by measuring the core temperature. The same loss increase in the zero voltage time intervals as illustrated in Figure 3.9 could be observed by this simple measurement. This comparative measurement indicates that the effect is not coming from the measurement equipment used.

Last but not least, the fact that this effect has been also observed by another research group [41] greatly increases the credibility of the result.

Concluding, during phases of constant flux, i.e. where the voltage across the magnetic component is zero, losses still occur. Based on a literature survey, it is hypothesized that this is because of relaxation processes in the magnetic core material. Next, a brief introduction about magnetic relaxation is given.

### 3.6.2 Theory of Relaxation Effects

There are basically three physical loss sources: static hysteresis losses, eddy-current losses, and a third loss component which is often referred to as residual losses. The residual losses are, according to [30], due to relaxation processes: if the thermal equilibrium of a magnetic system changes, the system progressively moves towards the new thermal equilibrium condition. When the magnetization changes rapidly, as for example is the case in high-frequency or pulsed field applications, such relaxation processes become very important.

The Landau-Lifshitz equation describes qualitatively the dynamics of the magnetic relaxation processes. This is a phenomenological equa-

tion that combines all processes that are involved in magnetic relaxation. The equation follows directly from equating the rate of change of the angular momentum  $L$  to the torque  $\mathbf{M} \times \mathbf{H}$  reduced by a frictional term that is directed opposite to the direction of motion [30]:

$$\frac{d\mathbf{M}}{dt} = \gamma \mathbf{M} \times \mathbf{H} - \Lambda \mathbf{M} \times (\mathbf{M} \times \mathbf{H})/M^2, \quad (3.17)$$

where  $\gamma = ge/2mc$  is the magnetomechanical ratio  $M/L$ ,  $\mathbf{M}$  is the magnetization vector,  $\mathbf{H}$  the magnetic field vector, and  $\Lambda$  is called the relaxation frequency. It describes how the system progressively moves towards the new thermal equilibrium. The equilibrium is achieved by rearranging the magnetic domain structures to reach states of lower energy. The relaxation process limits the speed of flux change, hence the B-H loops become rate-dependent. Several physical processes contribute simultaneously to magnetic relaxation. The interested reader is referred to [30, 32, 33] for more information.

Due to magnetic relaxation, the magnetization may change even when the applied field is constant (the magnetization is delayed). Consequently, a residual energy loss still occurs in the period of a constant applied field. Furthermore, the shape of the hysteresis loop is changed depending on the rate of change of the applied field (rate-dependent loop). An analysis of the impact of magnetic relaxation to a trapezoidal flux shape now follows.

### 3.6.3 Shape of B-H Loop for Trapezoidal Flux Waveforms

A B-H loop under trapezoidal flux waveform condition has been measured to gain a better comprehension of why the losses increase when the duration of the zero voltage period is increased. The CUT is a toroid core R42 made of ferrite EPCOS N87. In Figure 3.10(a) the flux waveform, in Figure 3.10(b) the corresponding B-H loop, and in Figure 3.10(c) the corresponding current waveform are plotted. Figure 3.10(b) and (c) are measured figures. The B-H loop always traverses counterclockwise. The different instants (cf. numbers in Figure 3.10(a), (b) and (c)) are now discussed step-by-step:

1. A constant voltage at the CUT primary winding results in a time linear flux increase.

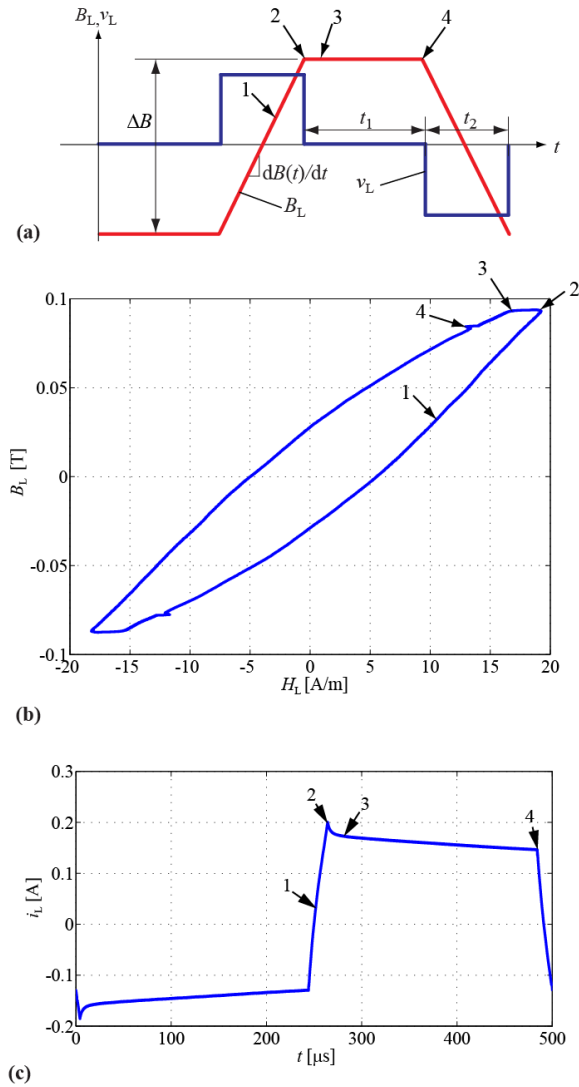


**Figure 3.10:** (a) Voltage and flux density waveforms. (b) B-H loop to illustrate magnetic relaxation under trapezoidal flux shape condition. (c) Current waveform.

2. The CUT primary voltage is set to zero; as a consequence the flux is frozen ( $dB/dt = 0$ ). However, the material has not yet reached its thermal equilibrium. The magnetic field strength  $H$  decreases in order to move towards the new thermal equilibrium and therewith reaches a state of lower energy. This can also be observed in the current (the current declines accordingly between point 2 and 3).
3. This point is reached approximately  $24\ \mu\text{s}$  after point 2. It is the point of the new thermal equilibrium.
4. This point is reached approximately  $200\ \mu\text{s}$  after point 3. The demagnetization in the zero voltage period is due to the small voltage drop over the on-resistance of the MOSFETs and copper resistance of the inductor primary winding. This demagnetization follows a different time constant than the demagnetization due to relaxation losses (cf. the approximately same distance 2-3 and 3-4, but the different time scale). This demagnetization can be observed in Figure 3.10(c) between point 3 and 4. In a measured flux waveform, this demagnetization could be observed too; however, Figure 3.10(a) is an illustrative figure which neglects this demagnetization, therefore, it cannot be seen there. At point 4 a negative voltage is applied to the CUT. The small buckle in the B-H loop is due to small capacitive currents at the switching instant.

The period between point 2 and 3 obviously increases the area of the B-H loop, and therewith increases the core losses. The loop area increases as a function of the duration  $t_1$ . After the thermal equilibrium is reached (in the above example after approximately  $24\ \mu\text{s}$ ) the loss increase becomes (almost) zero. In the next section more measurements are presented to find a method to include this effect into an existing core loss model.

### 3.6.4 Model Derivation

#### Model Derivation 1: Trapezoidal Flux Waveform

Losses can be calculated with the iGSE (3.4), without requiring extra characterization of material parameters beyond the parameters for the Steinmetz equation. The Steinmetz parameters are often given by core

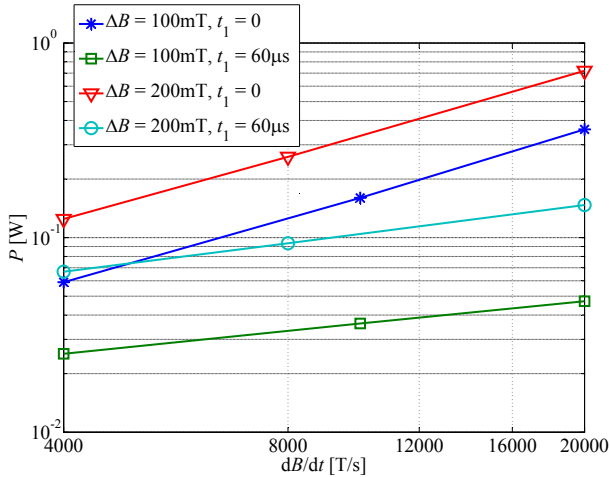


**Figure 3.11:** Core Loss (ferrite N87; measured on R42 core); temperature = 25 °C.

manufacturers, hence core loss modeling is possible without performing extensive measurements. However, the approach has some drawbacks. First, it neglects the fact that core losses may vary under a DC bias condition. This will be discussed in Section 3.7, where a graph showing the dependency of the Steinmetz parameters ( $\alpha$ ,  $\beta$  and  $k$ ) on premagnetization is introduced. With it, losses can be calculated via the Steinmetz equation (3.3) or the iGSE (3.4) using appropriate Steinmetz parameters. Another source of inaccuracy is that relaxation effects are not taken into consideration. As approach (3.4) is very often discussed in literature and often applied for designing magnetic components, improving this method would have the most practical use. Furthermore, in [6] it has been evaluated as the most accurate state-of-the-art loss model based on Steinmetz parameters. For this two reasons, in the following discussion the iGSE will be extended to consider relaxation losses as well.

When plotting the losses with logarithmic axes, where the x-axis represents the frequency and the y-axis represents the power loss, an approximately straight line is drawn. This is because the losses follow a power function as e.g. the Steinmetz equation (3.3) is. The parameter  $\alpha$  of (3.3) represents the slope of the curve in the plot. In Figure 3.11

such plots are given for few operating points. Instead of the frequency  $f$ ,  $dB/dt$  has been used as x-axis, which, for symmetric triangular or trapezoidal flux waveforms, is directly proportional to the frequency  $f$ . The time  $t_1$  is defined as in Figure 3.10 ( $t_1 = 0$  leads to a triangular flux waveform). As can be seen in Figure 3.11, when a long zero voltage phase is added between two voltage pulses (having a flux waveform as given in Figure 3.10) the loss still follows a power function with variable  $dB/dt$  (the losses are still represented by an approximately straight line). The same conclusion can be made when keeping  $dB/dt$  constant and varying  $\Delta B$ , hence, the use of a power function with variable  $\Delta B$  is justified as well.

It should be pointed out that when a (long) zero voltage interval ( $t_1 \neq 0$ ) is present the average power loss decreases (cf. Figure 3.11). There is no discrepancy with the observation in Figure 3.9, where an *energy loss per cycle* increase has been observed. When having a zero voltage interval the energy loss per cycle increases, but the period increases as well and leads to a lower average power loss.

The approach of (3.4) will now be extended by taking relaxation effects into consideration. This is done by adding a new term that represents the relaxation effect of a transition to zero voltage. As can be seen in Figure 3.9, the energy loss increase due to the zero voltage interval can be modeled with the exponential equation

$$E = \Delta E \left(1 - e^{-\frac{t_1}{\tau}}\right), \quad (3.18)$$

where  $\Delta E$  is the maximum energy loss increase (which occurs, when the magnetic material has enough time to reach the new thermal equilibrium),  $\tau$  is the relaxation time that has to be further determined, and  $t_1$  is the duration of the constant flux (zero applied voltage) phase. The exponential behavior is typical for relaxation processes. Measurements have shown that  $\tau$  can be considered to be a constant parameter for a given core material that does not change for different operating points. The increase of energy loss per cycle in measurements on waveforms illustrated in Figure 3.10(a) (or Figure 3.8) leads to twice  $\Delta E$ , since there are two transitions to zero voltage. Consequently, in Figure 3.9 the loss increase is labeled as  $2 \cdot \Delta E$ . Different measurements on waveforms as illustrated in Figure 3.10(a) have been conducted to determine a formula to describe  $\Delta E$ . The corresponding results are given in Figure 3.12, where measured values of  $2 \cdot \Delta E$  for different operating points are plotted. In Figure 3.12(a)  $dB/dt$  has been used as x-axis and in

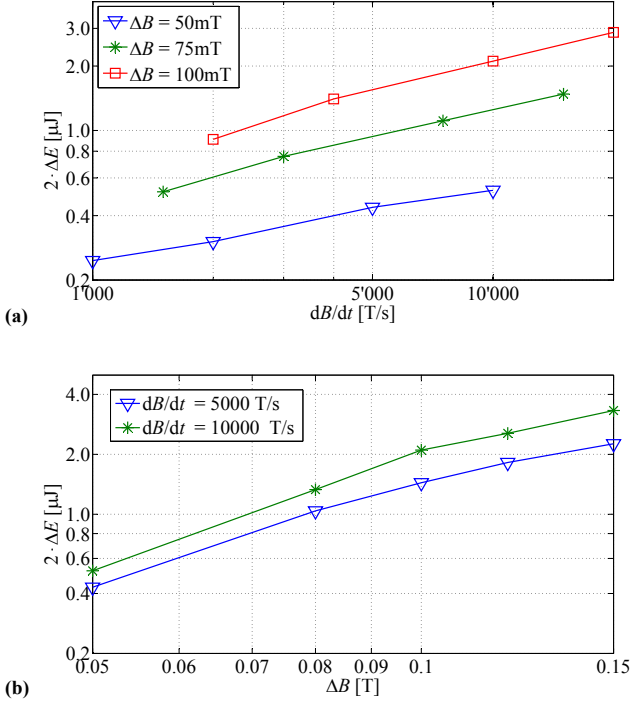


**Figure 3.12:** Measured values of  $2 \cdot \Delta E$  (ferrite N87; measured on R42 core); temperature = 25 °C.

Figure 3.12(b)  $\Delta B$  has been chosen for the  $x$ -axis. In both cases approximately parallel straight lines are drawn, i.e.  $2 \cdot \Delta E$  (approximately) follows a power function with variables  $dB/dt$  and  $\Delta B$ . Hence,  $\Delta E$  of one transition to zero voltage can be described by a power function with variables  $\Delta B$  and  $dB(t_-)/dt$ , where  $\Delta B$  and  $dB(t_-)/dt$  define the flux density waveform before this transition to zero voltage as illustrated in Figure 3.13. As a consequence, the following power function can be defined for  $\Delta E$ :

$$\Delta E = k_r \left| \frac{d}{dt} B(t_-) \right|^{\alpha_r} (\Delta B)^{\beta_r}, \quad (3.19)$$

where  $\alpha_r$ ,  $\beta_r$ , and  $k_r$  are new model parameters which have to be determined empirically. With (3.19), the relaxation losses of a transition to

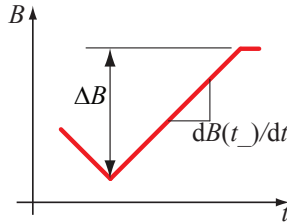


**Figure 3.13:** Definition of  $dB(t_-)/dt$  and  $\Delta B$ .

zero voltage can be determined according to the antecedent flux density slope  $dB(t_-)/dt$  and the antecedent flux density peak-to-peak value  $\Delta B$ . Accordingly, when the flux density reaches and remains at zero as occurs e.g. in a buck converter that is operating in discontinuous conduction mode, relaxation losses have to be taken into consideration as well. However, the losses may (slightly) differ in this situation because the antecedent flux density is DC biased. This DC level of the antecedent flux density has not been part of investigation of the present work and could be investigated as part of future work.

Concluding, (3.4) has been extended by an additional term that describes the loss behavior for a transient to constant flux. This leads to a new model to calculate the time-average power loss density

$$P_v = \frac{1}{T} \int_0^T k_i \left| \frac{dB}{dt} \right|^\alpha (\Delta B)^{\beta-\alpha} dt + \sum_{l=1}^n P_{rl}, \quad (3.20)$$

where  $P_{rl}$  represents the time-average power loss density due to the  $l^{\text{th}}$  of  $n$  transients to zero voltage. This power loss of each transient to zero voltage is calculated according to

$$P_{rl} = \frac{1}{T} k_r \left| \frac{d}{dt} B(t_-) \right|^{\alpha_r} (\Delta B)^{\beta_r} \left( 1 - e^{-\frac{t_l}{\tau}} \right). \quad (3.21)$$

For the sake of completeness, a limitation of the given model should be pointed out. The curves in Figure 3.12 do not have the shape of exact straight lines. This illustrates the fact that the newly introduced parameters  $\alpha_r$ ,  $\beta_r$  are only valid for a limited  $dB(t_-)/dt$  and  $\Delta B$  range. The limited parameter validity is a general problem of the Steinmetz approach.

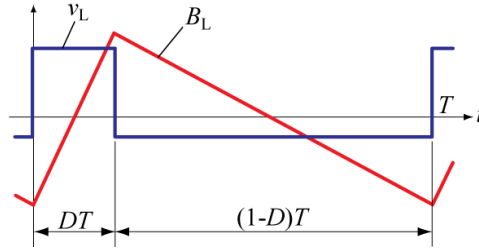


**Figure 3.14:** Triangular flux density waveform.

### Model Derivation 2: Triangular Flux Waveform

Often in power electronics, one has a period of zero voltage applied to a magnetic component winding, e.g. in the transformer of a bidirectional isolated DC-DC converter with Dual Active full Bridges (DAB). A DAB will be presented in Section 3.6.4 as an example to illustrate the model. In this case, (3.20) can directly be used to improve the loss model.

However, another frequently occurring waveform is a triangular flux waveform in which the flux slope changes to another *nonzero* value. This case is illustrated in Figure 3.14. When a duty cycle of 50% ( $D = 0.5$ ) is assumed, directly after switching to the opposite voltage the flux slope reverses, the material has hardly time to move towards the new thermal equilibrium. As a consequence, no notable loss increase is expected and thus this case is well described by the iGSE (3.4). However, when the duty cycle goes to smaller values, once each period, a high flux slope is followed by a comparatively very slow flux change. Assuming  $D$  to be infinitely small, it is like a switch to a constant flux. Consequently, in this case the iGSE (3.4) is not accurate and the relaxation term has to be added. In all operating points where  $D > 0$  and  $D < 0.5$  (or  $D > 0.5$  and  $D < 1$ ), a behavior that is in-between these two cases is expected. In other words, only part of the relaxation term has to be added.

In Figure 3.15 the calculated and measured core losses as a function of the duty cycle are plotted. One calculation has been performed based on the iGSE (3.4) which, according to the above discussion, represents the lower limit of possible losses (as no relaxation effects are taken into account). It should be noted that two sets of Steinmetz parameters have been used for the calculation of the iGSE. The reason is that the Steinmetz parameters are only valid in a limited  $dB/dt$  range, and the

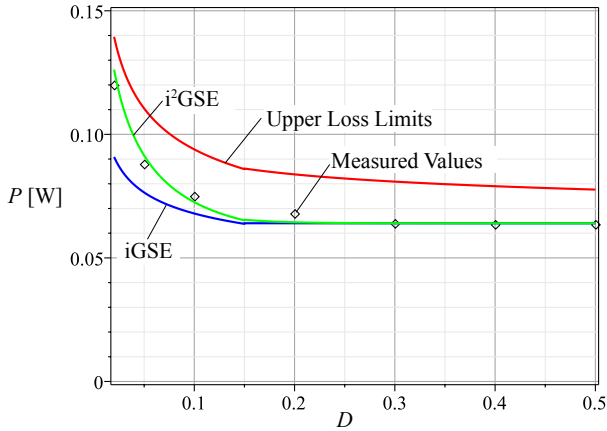


**Figure 3.15:** Core loss duty cycle dependency.  $\Delta B = 0.1 \text{ T}$ ,  $f = 20 \text{ kHz}$ .

$dB/dt$  in this experiment is varying in a wide range. This explains the sharp bend of the  $iGSE$  curve at  $D = 0.15$  (change of Steinmetz parameter). Another calculation has been made always including the full relaxation loss term and which represents the upper loss limit. In other words, it can be said that losses are expected to have values between the line representing the upper loss limit and the line representing the lower loss limit ( $iGSE$ ). According to the previous discussion, the real losses are closer to the lower loss limit for  $D$  close to 0.5, and losses closer to the upper loss limit for  $D$  close to zero. Measurements seem to confirm this hypothesis as can be seen in Figure 3.15. Other operating points showed the same behavior.

Based on the above discussion, the new approach can be further improved to be also valid for triangular flux waveforms. Basically, (3.20) can be rewritten as

$$P_v = \frac{1}{T} \int_0^T k_i \left| \frac{dB}{dt} \right|^\alpha (\Delta B)^{\beta-\alpha} dt + \sum_{l=1}^n Q_{rl} P_{rl}, \quad (3.22)$$

where  $Q_{rl}$  has to be further defined. In the case of a switch to zero voltage,  $Q_{rl}$  needs to have the value 1. Furthermore, it has to have a structure such that (3.22) fits the measurement points of a duty cycle measurement, such as illustrated in Figure 3.15. The following function

has been chosen:

$$Q_{rl} = e^{-q_r \left| \frac{dB(t_+)/dt}{dB(t_-)/dt} \right|}, \quad (3.23)$$

where  $dB(t_-)/dt$  represents the flux density before the switching,  $dB(t_+)/dt$  the flux density after the switching, and  $q_r$  is a new material parameter. For a triangular waveform as illustrated in Figure 3.14, (3.23) can be rewritten (for  $D \leq 0.5$ )

$$Q_{rl} = e^{-q_r \frac{\frac{\Delta B}{(1-D)T}}{\frac{\Delta B}{DT}}} = e^{-q_r \frac{D}{1-D}}. \quad (3.24)$$

In the case of the material Epcos N87  $q_r = 16$  has been found, the resulting loss curve is plotted in Figure 3.15. Before giving an illustrative example in Section 3.6.4, the new model will be summarized and the steps to extract the model parameters will be given.

### New Core Loss Model: The $i^2$ GSE

A new loss model that substantially increases the expected accuracy when core losses are modeled has been introduced. This new model is named the *improved-improved Generalized Steinmetz Equation*,  $i^2$ GSE. The name has been chosen because it is an improved version of the iGSE [35]. The time-average power loss density can be calculated with

$$P_v = \frac{1}{T} \int_0^T k_i \left| \frac{dB}{dt} \right|^\alpha (\Delta B)^{\beta-\alpha} dt + \sum_{l=1}^n Q_{rl} P_{rl}, \quad (3.25)$$

where  $P_{rl}$  is calculated for each voltage change according to

$$P_{rl} = \frac{1}{T} k_r \left| \frac{d}{dt} B(t_-) \right|^{\alpha_r} (\Delta B)^{\beta_r} \left( 1 - e^{-\frac{t_l}{\tau}} \right), \quad (3.26)$$

$Q_{rl}$  is a function that further describes the voltage change and is

$$Q_{rl} = e^{-q_r \left| \frac{dB(t_+)/dt}{dB(t_-)/dt} \right|}, \quad (3.27)$$

and  $\alpha$ ,  $\beta$ ,  $k_i$ ,  $\alpha_r$ ,  $\beta_r$ ,  $k_r$ ,  $\tau$ , and  $q_r$  are material parameters.

Now, the steps to extract the model parameters are given:

1. First, the parameters  $k_i$ ,  $\alpha$ , and  $\beta$  are extracted. The core is excited with a rectangular voltage waveform that leads to a symmetric triangular flux waveform. Measurements at three operating points are performed, then (3.25) is solved for the three

parameters. For symmetric triangular flux waveforms (with duty cycle  $D = 0.5$ ) it is  $\sum_{l=1}^n Q_{rl}P_{rl} = 0$ . In Table 3.3 the measurement results and the corresponding parameters are given. These parameters could be extracted directly from the data sheet as well, as explained in [35].

2. The parameter  $\tau$  can be read from Figure 3.9 with

$$\frac{\Delta E}{\tau} = \frac{dE}{dt}, \quad (3.28)$$

where  $dE/dt$  represents the slope of the energy increase directly after switching to zero voltage. This is illustrated in Figure 3.9.  $\tau = 6 \mu\text{s}$  has been extracted for the material N87.

3. The parameters  $k_r$ ,  $\alpha_r$ , and  $\beta_r$  are extracted by performing measurements at three operating points with  $t_1$  large enough to let the material reach the thermal equilibrium. Then, (3.19) is solved for the three parameters. In Table 3.3 the measurement results and the corresponding parameters are given.
4. The parameter  $q_r$  has to be selected such that (3.25) fits the measurement points of a duty cycle measurement, as illustrated in Figure 3.15.

All model parameters are summarized in Table 3.3. Extracting the parameters is sometimes difficult and measurements have to be performed very carefully. One error source is a possible current decrease due to a voltage drop over the inductor winding during "zero" voltage phase. This can be avoided by choosing a high amount of primary turns. This increases the inductance value and the current is kept more constant (by choosing a high amount of primary turns the winding copper resistance increases as well; however, the inductance value increases quadratically while the resistance value increases linearly).

### Example of How to Use the New Model

In the previous section, a new core loss modeling approach was introduced. This section shows now an easy-to-follow example that illustrates how to calculate core losses of a transformer employed in a bidirectional isolated DC-DC converter with Dual Active full Bridges

| Operating Point<br>( $\Delta B$ ; $f$ ) | Loss Density<br>[kW/m <sup>3</sup> ] | Model Parameters  |
|---|--------------------------------------|-------------------|
| (0.1 T; 20 kHz)                         | 5.98                                 | $k_i = 8.41$      |
| (0.1 T; 50 kHz)                         | 16.2                                 | $\alpha = 1.09$   |
| (0.2 T; 50 kHz)                         | 72.8                                 | $\beta = 2.16$    |
| ( $\Delta B$ ; $dB(t_-)/dt$ )           | [J/m <sup>3</sup> ]                  |                   |
| (0.1 T; 4 kT/s)                         | 0.068                                | $k_r = 0.0574$    |
| (0.1 T; 20 kT/s)                        | 0.13                                 | $\alpha_r = 0.39$ |
| (0.2 T; 20 kT/s)                        | 0.32                                 | $\beta_r = 1.31$  |
|   |                                      | $\tau = 6 \mu s$  |
|   |                                      | $q_r = 16$        |

**Table 3.3:** Measurement results and model parameters of material EPCOS N87.

(DAB) [6, 48]. In Figure 3.16(a) the simplified schematic and in Table 3.4 the specifications of the transformer are given. The shape of the core influences the core losses, however, this is not the scope of the present work, hence a simple toroid is considered as the transformer core. Phase-shift modulation has been chosen as modulation method: primary and secondary full bridge are switched with 50% duty cycle to achieve a rectangular voltage  $v_1$  and  $v_2$  across the primary and secondary transformer side, respectively. The waveforms are illustrated in Figure 3.16(b), including the magnetic flux density  $B_\mu$  of the transformer core. A phase shift  $\gamma$  between  $v_1$  and  $v_2$  results in a power transfer. When the voltages  $v_1$  and  $v_2$  are opposed (which is the case in phase  $t_\gamma$ ), the full voltage drop is across the transformer leakage inductance and the magnetic flux density  $B_\mu$  remains unchanged.

Only the magnetic flux density  $B_\mu$  time behavior has been considered for designing the transformer, i.e. no winding losses or leakage inductance have been calculated. The value of the leakage inductance is very important for the functionality, however, it is not discussed here. Therefore, no statement about feasibility is made, the circuit should only represent solely a simple and easy-to-follow illustrative magnetic example.

The losses are calculated according to the i<sup>2</sup>GSE (3.25). The results are then compared with measurement results. The peak flux density in

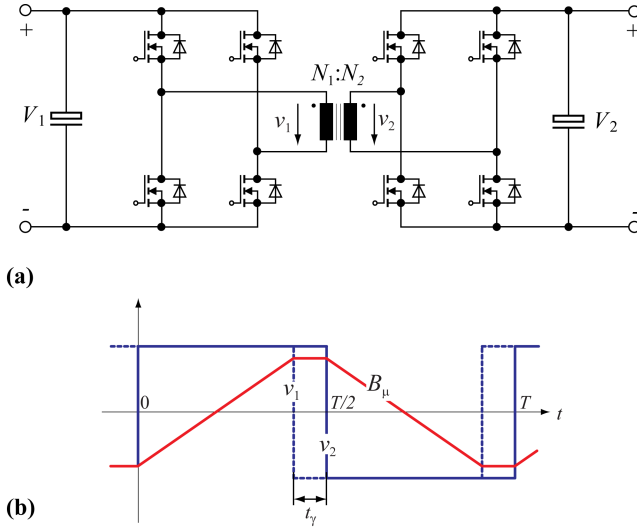


**Figure 3.16:** DAB schematic (a) and waveforms (b) with specifications given in Table 3.4.

|  |                                       |
|--|---------------------------------------|
| $V_{\text{DC}} = V_1 = V_2$            | 42 V                                  |
| $f$                                    | 50 kHz                                |
| $N=N_1=N_2$                            | 20                                    |
| Effective Magnetic Length $l_e$        | 103 mm                                |
| Effective Magnetic Cross Section $A_e$ | 95.75 mm <sup>2</sup>                 |
| Core                                   | EPCOS N87, R42<br>(B64290L22X87) [29] |

**Table 3.4:** Specifications of DAB Transformer

the core can be calculated with [6]

$$\hat{B} = \frac{1}{2} \frac{V_{\text{DC}}}{N A_e} \left( \frac{T}{2} - t_{\gamma} \right) \quad (3.29)$$

and its time derivative with

$$\frac{dB}{dt} = \begin{cases} \frac{V_{DC}}{NA_e} & \text{for } t \geq 0 \text{ and } t < \frac{T}{2} - t_\gamma, \\ 0 & \text{for } t \geq \frac{T}{2} - t_\gamma \text{ and } t < \frac{T}{2}, \\ -\frac{V_{DC}}{NA_e} & \text{for } t \geq \frac{T}{2} \text{ and } t < T - t_\gamma, \\ 0 & \text{for } t \geq T - t_\gamma \text{ and } t < T. \end{cases} \quad (3.30)$$

Calculating the losses according to (3.25) leads to the following expression as a function of  $t_\gamma$

$$P = \frac{T - 2t_\gamma}{T} k_i \left| \frac{V_{DC}}{NA_e} \right|^\alpha \left| \frac{V_{DC}}{NA_e} \left( \frac{T}{2} - t_\gamma \right) \right|^{\beta - \alpha} A_e l_e \\ + A_e l_e \sum_{l=1}^2 Q_{rl} P_{rl}, \quad (3.31)$$

where  $\sum_{l=1}^2 Q_{rl} P_{rl}$  represents the two transients to zero voltage. There are two switching instants to zero voltage, each with  $Q_{rl} = 1$ . The values for  $P_{rl}$  then have to be determined: it is for each transient

$$P_{rl} = \frac{1}{T} k_r \left| \frac{V_{DC}}{NA_e} \right|^{\alpha_r} \left| \frac{V_{DC}}{NA_e} \left( \frac{T}{2} - t_\gamma \right) \right|^{\beta_r} \left( 1 - e^{-\frac{t_\gamma}{\tau}} \right). \quad (3.32)$$

The losses have been calculated according to the new approach, and have been compared to a calculation using the classic iGSE (3.4) and with measurement results. Open-circuit (no load) measurements have been performed to validate the new model: the primary winding is excited to achieve a flux density as illustrated in Figure 3.16(b). Measurements for different values of  $t_\gamma$  have been performed, at constant frequency  $f$  and voltage  $V_{DC}$ . The new model and measurement results match very well as shown in Figure 3.17.

In [6] different state-of-the-art core loss calculation approaches are compared using a very similar example. The iGSE (3.4) showed the best agreement with measurements, but for increasing zero voltage periods  $t_\gamma$ , the calculated core losses start deviating from the measured core losses. The reason becomes clear with the new approach i<sup>2</sup>GSE and the calculation can be improved.

### 3.6.5 Measurements on Different Materials

The approach has been confirmed on different materials, including on VITROPERM 500F from VAC (measured on W452 core). Measure-

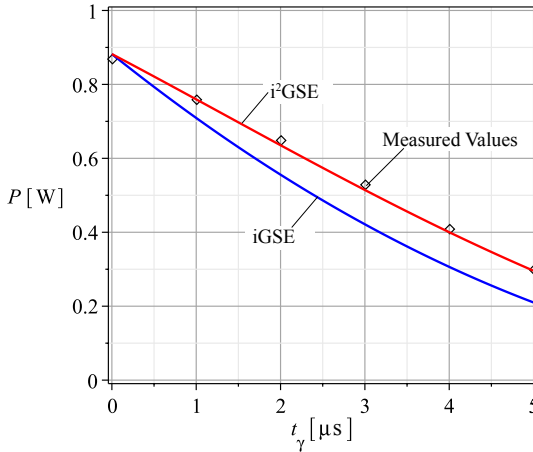


**Figure 3.17:** Loss calculation and loss measurement comparison of the DAB example.

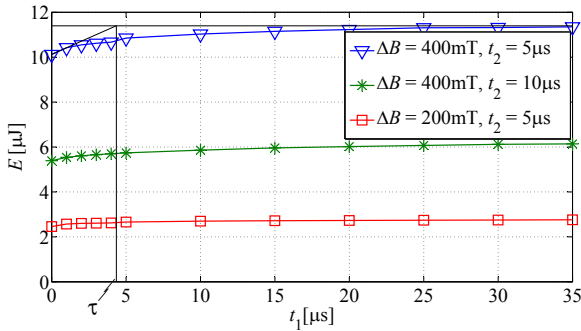


**Figure 3.18:** Measurement results measured on VITROPERM 500F from VAC (measured on W452 core); temperature = 25 °C. It is further illustrated how  $\tau$  according to (3.28) can be extracted.

ments on waveforms as illustrated in Figure 3.10(a) have been performed. Figure 3.18 shows the corresponding measurement results. The model parameters are given in Table 3.5. Measurements show promise that the approach is applicable for all material types; however, this remains to be confirmed as part of future work.

**Table 3.5:** Model parameters of material VITROPERM 500F (VAC).

|            |                     |
|------------|---------------------|
| $\alpha$   | 1.88                |
| $\beta$    | 2.02                |
| $k_i$      | $137 \cdot 10^{-6}$ |
| $\alpha_r$ | 0.76                |
| $\beta_r$  | 1.70                |
| $k_r$      | $139 \cdot 10^{-6}$ |
| $\tau$     | $4.5 \mu\text{s}$   |
| $q_r$      | 4                   |

### 3.6.6 Conclusion and Future Work

As experimentally verified, core losses are not necessarily zero when zero voltage is applied across a transformer or inductor winding after an interval of changing flux density. A short period after switching the winding voltage to zero, losses still occur in the material. This work hypothesizes that this is due to magnetic relaxation. A new loss modeling approach has been introduced and named the *improved-improved Generalized Steinmetz Equation*, i<sup>2</sup>GSE. The i<sup>2</sup>GSE needs five new parameters to calculate new core loss components. Hence, in total eight parameters are necessary to accurately determine core losses.

The tested measurement range is given in the following to identify the range in which the model validity has been confirmed. Two types of waveforms have been analyzed: trapezoidal as illustrated in Figure 3.10(a) and triangular waveforms as illustrated in Figure 3.14. For trapezoidal waveforms, measurements with  $t_1 = 0 \dots 500 \mu\text{s}$  and  $t_2 = 5 \dots 100 \mu\text{s}$  have been conducted. For the triangular waveforms measurements in the range between 20 kHz  $\dots$  100 kHz and  $D = 0.02 \dots 0.5$  have been conducted. No measurements for very low values of  $t_2$  have been conducted; however, the triangular operating point with  $D = 0.02$  and  $f = 20 \text{ kHz}$ , for instance, has a flux rise time of  $1 \mu\text{s}$ , which indicates that the model is also applicable for very short voltage pulses.

The Steinmetz parameters are valid only for a limited frequency and flux density range. This is also the case for the additional parameters of the i<sup>2</sup>GSE as has been illustrated in Figure 3.12; this parameter

dependency has not been further investigated. Furthermore, a DC level of the antecedent flux density has not been part of this investigation and could be considered in the course of future work.

### 3.7 Core Losses Under DC Bias Conditions

In many power electronic applications magnetic components are biased with a DC or low-frequency premagnetization, e.g. in Switched-Mode Power Supplies (SMPS). Within SMPS circuits, magnetic components that are operating under DC bias conditions are commonly used and are often among the largest components. Many publications have shown that the influence of DC bias on the material properties can not be neglected [8, 11, 12, 13, 14, 15, 16]. An approach how to handle DC bias losses is described in [37, 38, 39]. There, losses are calculated with a loss map that is based on measurements. This loss map stores the loss information for many operating points, each described by the flux ripple  $\Delta B$ , the frequency  $f$ , and a DC bias  $H_{DC}$ . It is explained how this loss map can be used to calculate core losses of inductors employed in power electronic systems. One parameter in the loss map is the DC premagnetization, thus the loss increase due to DC bias is considered in this approach. However, extensive measurements are necessary to build the loss map. Another approach how to consider DC bias losses is introduced in [14]: the effect of a DC bias is modeled by the given ratio between losses with and without DC bias for different DC bias levels  $H_{DC}$  and different AC flux densities. This ratio is called the displacement factor DPF. In [14] a graph that shows the DPF is given for the material ferrite N87 from EPCOS. In [11] an empirical formula that describes the DPF is given (though it is not named DPF). According to [11, 14] the DPF does not depend on the frequency  $f$  and can be described as a function of the AC flux density and the DC bias  $H_{DC}$ . A similar approach is suggested in [15], but according to [15] the DPF does not depend on the AC flux density. The influence of the frequency on the DPF has not been discussed. The approaches of [11, 14, 15] have in common that a factor is introduced by which the calculated losses have to be multiplied to take a premagnetization into consideration. In other words, the parameter  $k$  of (3.3) (or  $k_i$  of (3.4)) is multiplied by the DPF and therewith becomes dependent on  $\hat{B}$  (or  $\Delta B$ ).

This thesis proposes a new approach how to describe core losses under DC bias condition. A graph that shows the dependency of the

Steinmetz parameters ( $\alpha$ ,  $\beta$  and  $k$ ) on premagnetization is introduced in Section 3.7.1. This enables the calculation of losses via the Steinmetz equation (3.3) or the iGSE (3.4) using appropriate Steinmetz parameters.

### 3.7.1 Measurement Results and the Steinmetz Premagnetization Graph (SPG)

In this section, measurement results are presented and a new approach to describe core losses under DC bias conditions is introduced that is based on a graph that shows the dependency of the Steinmetz parameters ( $\alpha$ ,  $\beta$  and  $k$ ) on premagnetization. This is done on the example of the material ferrite N87 from EPCOS (core part number B64290L22X87 [29]). In Figure 3.19 the core losses and in Figure 3.20 the core losses normalized to the losses  $P_0$  at zero premagnetization are shown for different DC bias values. In Figure 3.21 the losses are plotted as a function of the frequency  $f$  and in Figure 3.22 the losses are plotted as a function of the peak-to-peak flux density  $\Delta B$ , with and without DC bias. To describe the losses via the Steinmetz equation (3.3) or the iGSE (3.4) is the most common method, hence improvements of this method would be most beneficial for design engineers. As the iGSE (3.4) is more suitable for the description of core losses in power electronic applications, in all following considerations the three discussed parameters are  $\alpha$ ,  $\beta$ , and  $k_i$  of the iGSE ( $\alpha$ ,  $\beta$  are the same as in (3.3), while  $k_i$  is described in (3.5)). For the applied waveform as illustrated in Figure 3.6 (symmetric triangular current/flux shape) (3.4) leads to

$$P_v = k_i(2f)^\alpha \Delta B^\beta. \quad (3.33)$$

When core losses are plotted with logarithmic axes, where the x-axis represents the frequency and the y-axis represents the power loss, approximately straight lines are drawn (cf. Figure 3.21). This is because the losses follow a power function as e.g. the laws stated in (3.3) and the iGSE (3.4) are. The parameter  $\alpha$  represents the slope of the curve in this plot. The same can be said when the frequency  $f$  is kept constant and  $\Delta B$  is varied; hence, the use of a power function with variable  $\Delta B$  is justified as well (cf. Figure 3.22). The parameter  $\beta$  represents the slope of the curve in this plot. When a core is under DC bias condition, the losses over a wide range of  $H_{DC}$  still can be described with the Steinmetz equation (3.3) or the iGSE (3.4), i.e. the losses

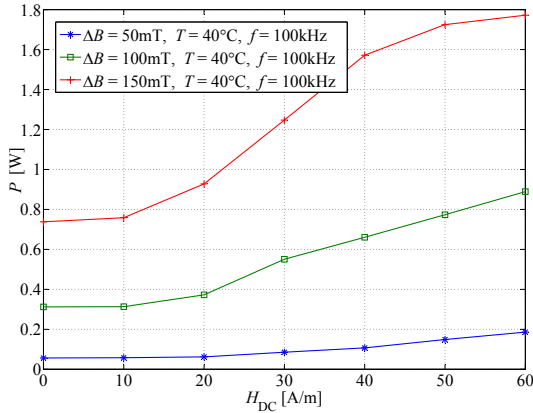


**Figure 3.19:** Core losses under DC bias conditions (ferrite N87; measured on R42 core),  $f = 100\text{ kHz}$ ,  $T = 40^\circ\text{C}$ .

still follow the power equation stated by Steinmetz (cf. Figure 3.21 and Figure 3.22). However, for very high values of  $H_{DC}$  and high flux densities  $\Delta B$  the use of a power function is not appropriate anymore (cf. Figure 3.22, curve for  $H_{DC} = 80\text{ A/m}$ ). This is due to saturation effects. The curve for  $H_{DC} = 50\text{ A/m}$  has been determined as the last one that can be considered as an approximate straight line over a wide flux density range. For most applications it is not desired to operate at higher DC bias levels; hence, the majority of inductive components are operated in a range where the losses still follow the power equation stated by Steinmetz.

As described above, the Steinmetz parameters must be adjusted according to the DC bias present. As will be shown in the following, a DC bias causes changes in the Steinmetz parameters  $\beta$  and  $k_i$ , but not in the parameter  $\alpha$ .

- ▶ The losses change when  $\Delta B$  and frequency  $f$  are kept constant and the DC bias  $H_{DC}$  is varied (cf. Figure 3.19). Thus, the Steinmetz parameter  $k_i$  depends on the DC bias  $H_{DC}$  ( $k_i = f(H_{DC})$ ).
- ▶ When the frequency  $f$  is kept constant, the factor by which the losses increase due to a premagnetization  $H_{DC}$  differs for different  $\Delta B$  (cf. Figure 3.20). Thus, the Steinmetz parameter  $\beta$  depends on the premagnetization  $H_{DC}$  as well ( $\beta = f(H_{DC})$ ). The slopes

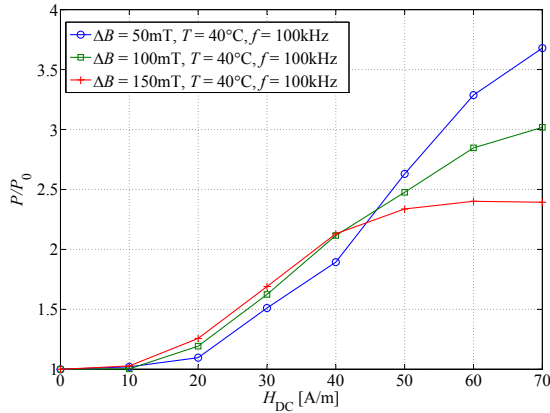


**Figure 3.20:** Core losses under DC bias conditions, normalized to losses  $P_0$  at zero premagnetization (ferrite N87; measured on R42 core),  $f = 100\text{ kHz}$ ,  $T = 40^\circ\text{C}$ .

of the curves in Figure 3.22 represent the parameter  $\beta$ . As can be seen the curve for  $H_{DC} = 20\text{ A/m}$  is slightly steeper compared to the curve of  $H_{DC} = 0\text{ A/m}$ , though the difference is very little. However, a small change in  $\beta$  already considerably influences the core losses, as one can see when comparing with Figure 3.20. It should be again pointed out that it is only valid to define a  $\beta$  within the range of  $H_{DC}$  where the logarithmically plotted losses lead to an approximate straight line (cf. Figure 3.22).

- According to [14], the influence of a DC bias does not depend on the measurement frequency  $f$ . This has been confirmed for frequencies up to 100 kHz. As can be seen in Figure 3.21, at a constant  $\Delta B$ , the factor by which the losses increase due to a premagnetization  $H_{DC}$  is the same for different frequencies  $f$  (the slopes of the curves remain the same). Hence, the Steinmetz parameter  $\alpha$  is in this frequency range independent of the premagnetization  $H_{DC}$  ( $\alpha = \text{const.}$ ). The fact that  $\alpha$  is constant has been confirmed to frequencies up to 100 kHz; no measurements above this frequency have been performed, hence no information can be given as to whether and up to which frequency  $\alpha$  is constant.

Next, at each tested DC bias level the Steinmetz parameters have

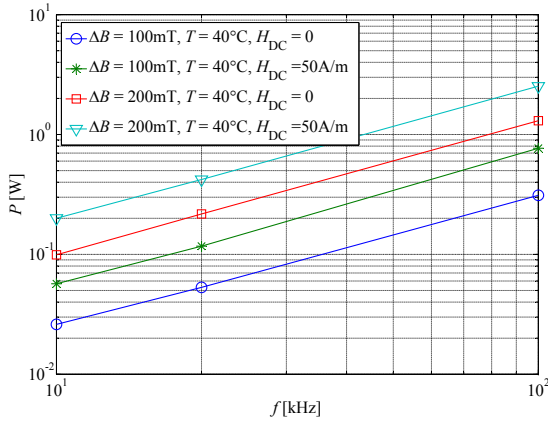


**Figure 3.21:** Core losses vs. frequency (ferrite N87; measured on R42 core),  $T = 40^\circ\text{C}$ .

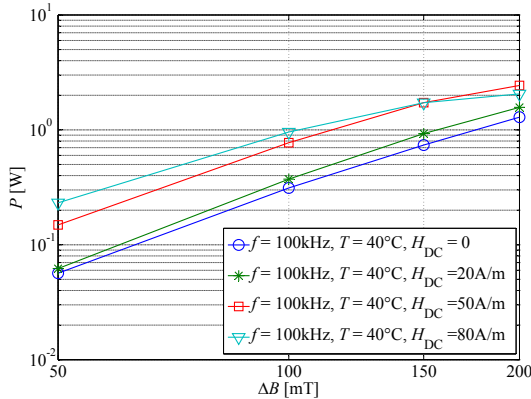


**Figure 3.22:** Core losses vs. flux density (ferrite N87; measured on R42 core),  $T = 40^\circ\text{C}$ .

been extracted. A least square algorithm has been implemented that fits measured losses with calculated data by minimizing the relative error at 3 different values of  $\Delta B$ , each measured at two frequencies. The markers on top of the curves in Figure 3.23 represent these values. As not only the Steinmetz parameters at discrete operating points are of

interest, a curve fitting algorithm has been implemented to extract the dependencies  $\beta = f(H_{\text{DC}})$  and  $k_i = f(H_{\text{DC}})$ . Its derivation is discussed in Appendix A.4.

For the material N87 from EPCOS the dependencies  $\beta = f(H_{\text{DC}})$  and  $k_i = f(H_{\text{DC}})$  are given in Figure 3.23, and normalized to  $\beta_0$  and  $k_{i0}$  in Figure 3.24.  $\beta_0$  and  $k_{i0}$  are the Steinmetz parameters at zero premagnetization. We call the graph illustrated in Figure 3.24 the *Steinmetz Premagnetization Graph* (SPG). The SPG is very useful and it would be valuable to have such a graph in the data sheet of a magnetic material as it would then be possible to calculate core losses under a DC bias condition. Figure 3.25 shows how the measured and, based on the SPG, calculated curves compare. For the considered working points the accuracy obtained has always been  $\leq \pm 15\%$ .

In Appendix A.3 SPGs of other materials (Ferroxcube 3F3 (ferrite), EPCOS N27 (ferrite), and VAC VITROPERM 500F (nanocrystalline material)) are given. Furthermore, a discussion how to extract the Steinmetz parameter value  $k$  from the SPG is given in Appendix A.5. The markers on top of the curves in the SPG represent the Steinmetz parameter values that are directly supported by measurement data. The SPG could be improved by an increase of the  $H_{\text{DC}}$  resolution to minimize interpolation errors. All given SPGs consider only the premagnetization range where it is still appropriate to use the Steinmetz approach, i.e. the losses still follow a power equation.

In the SPG, the Steinmetz parameters are plotted as a function of  $H_{\text{DC}}$ . For an ideal toroid  $H_{\text{DC}}$  can be calculated according to (3.10) as

$$H_{\text{DC}} = \frac{I_{\text{DC}} N_1}{l_e}, \quad (3.34)$$

where  $I_{\text{DC}}$  is the DC current,  $N_1$  is the number of excitation winding turns and  $l_e$  the effective magnetic path length of the CUT. It would also be possible to use  $B_{\text{DC}}$  instead of  $H_{\text{DC}}$ . For cores without air gaps,  $H_{\text{DC}}$  has the advantage that it is directly calculable from the current (as it is done in this work). For gapped cores, one would need to set up an accurate reluctance model (cf. Chapter 2) to calculate  $H_{\text{DC}}$  inside the core. The relationship  $B_{\text{DC}}(H_{\text{DC}})$  is customarily assumed to be the initial magnetization curve [14].

For the derivation of the SPG the losses are calculated according to (3.33). For the frequency  $f$  the unit Hertz (Hz) has been used and for the peak-to-peak flux density  $\Delta B$  the unit Tesla (T) has been used. Consequently, the SPG is only valid when this set of units is used.

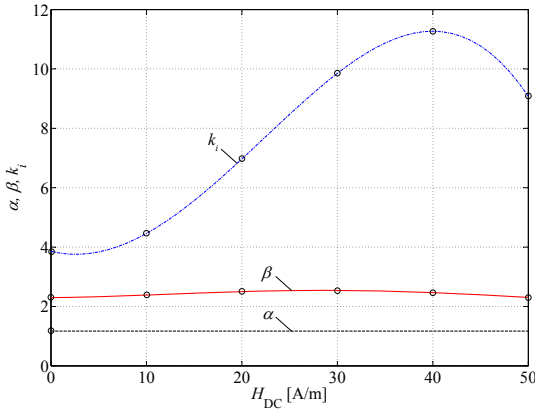


**Figure 3.23:** Steinmetz parameters as a function of premagnetization  $H_{DC}$  (ferrite N87),  $T = 40^\circ\text{C}$ .

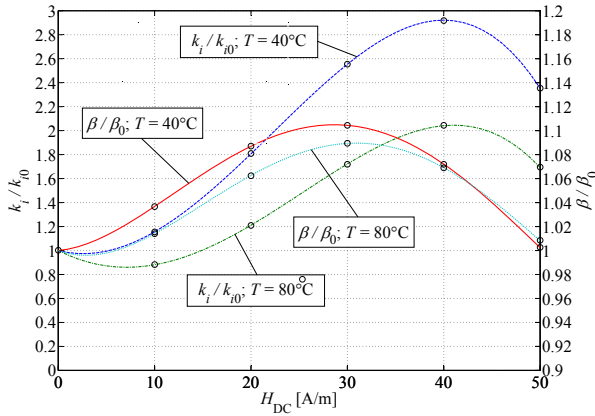


**Figure 3.24:** SPG of the material ferrite N87 (EPCOS).

### 3.7.2 Influence of Temperature

For an accurate core calculation, the temperature is another important parameter that considerably influences core losses. In Figure 3.26 the losses normalized to losses  $P_0$  at zero premagnetization are given for different temperatures. As can be seen for the material ferrite N87, at

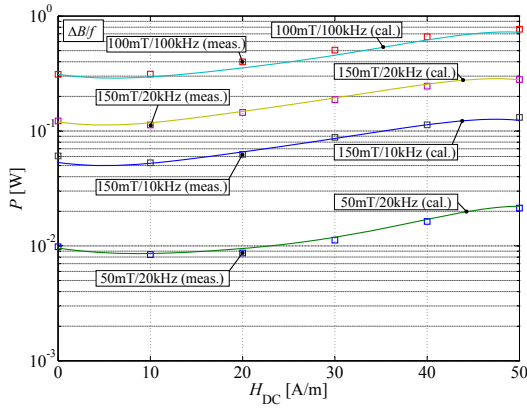


**Figure 3.25:** Core losses under DC bias conditions: measured (meas.) and calculated (cal.) curves (ferrite N87),  $T = 40^\circ\text{C}$ .

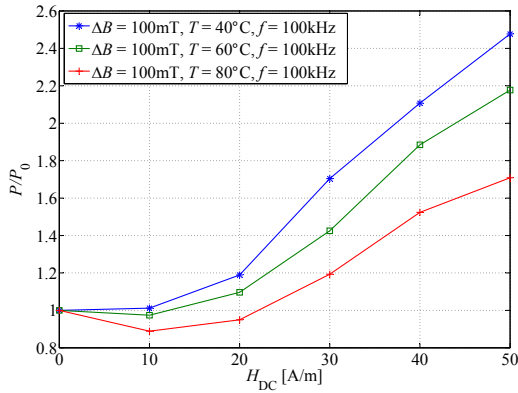


**Figure 3.26:** Core losses under DC bias conditions: measured at different operating temperatures. Normalized to losses  $P_0$  at zero premagnetization. Material N87.

higher temperatures the influence of a premagnetization on core losses reduces. The temperature influence is described by extending the SPG to curves of different operating temperatures, as shown in Figure 3.24.

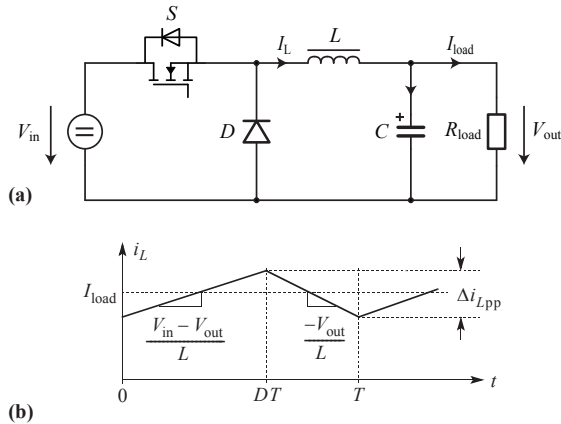


**Figure 3.27:** Buck converter schematic (a) and current waveform (b) with specifications given in Table 3.6.

|                    |  |
|--------------------|--|
| $V_{in} / V_{out}$ | 12 V / 6 V   |
| $f$                | 100 kHz  |
| $P$                | 2 W  |
| $I_{load}$         | 0.33 A   |
| $L$                | 150 $\mu$ H (EPCOS N87; R25; $N=8$ ; no air gap)<br>(core part number: B64290L618X87 [29]) |

**Table 3.6:** Buck converter specifications.

### 3.7.3 Example How to Use the SPG

In the previous sections the SPG has been introduced. This section presents now an easy-to-follow example that illustrates how to calculate core losses of the inductor of a power electronics converter with help of the SPG. In Figure 3.27 the schematic and the inductor current waveform of a buck converter, and in Table 3.6 the corresponding specifications are given. For the inductor  $L$  a DC bias of  $H_{DC} = 44$  A/m (according to (3.34)), and a peak-to-peak flux density ripple of  $\Delta B = 73$  mT is calculated. The following steps lead to the core losses that occur in the inductor:

- ▶ For the material used, the corresponding Steinmetz parameters are extracted from the datasheet. This is done by solving (3.3) at three operating points for  $\alpha$ ,  $\beta$ , and  $k$ :  $\alpha = 1.25$ ,  $\beta = 2.46$ ,  $k = 15.9$  (values for temperature = 40 °C, at zero premagnetization).
- ▶ Next,  $k_i$  is calculated according to (3.5):  $k_i = 1.17$ .
- ▶  $k_i$  and  $\beta$  are now adjusted according to the SPG of the material N87 (cf. Figure 3.24) for an operating point with  $H_{DC} = 44$  A/m:  $k'_i = 2.8 \cdot k_i = 3.28$  and  $\beta' = 1.04 \cdot \beta = 2.56$ .
- ▶ Now, the losses are calculated according to (3.4). For piecewise linear waveforms, as is the case in the presented example, the integral of (3.4) may be split into one piece for each linear segment, such that a complicated numerical integration is avoided [35]. The losses follow as

$$\begin{aligned}
 P &= V_e \frac{k'_i (\Delta B)^{\beta' - \alpha}}{T} \\
 &\cdot \left( \left| \frac{\Delta B}{DT} \right|^\alpha DT + \left| \frac{\Delta B}{(1-D)T} \right|^\alpha (1-D)T \right) \\
 &= V_e \frac{k'_i (\Delta B)^{\beta' - \alpha}}{T} \\
 &\cdot \left( \left| \frac{V_{in} - V_{out}}{NA_e} \right|^\alpha DT + \left| \frac{-V_{out}}{NA_e} \right|^\alpha (1-D)T \right) \\
 &= 52.8 \text{ mW}, \tag{3.35}
 \end{aligned}$$

where  $V_e = 3079 \text{ mm}^3$  is the effective core volume,  $A_e = 51.26 \text{ mm}^2$  is the effective core cross section,  $T = 1/f$  is the period length, and  $D = 0.5$  is the duty cycle.

Under the assumption that the Steinmetz parameters had not been adjusted according to the SPG in the example above, the losses would have been calculated as  $P = 24.5 \text{ mW}$ , which is an underestimation by a factor of more than two.

In case of a load change one has to redo the core loss calculation as a load change leads to a change in the premagnetization and, accordingly, to a change of the core losses. This fact is rarely considered when modeling magnetic components.

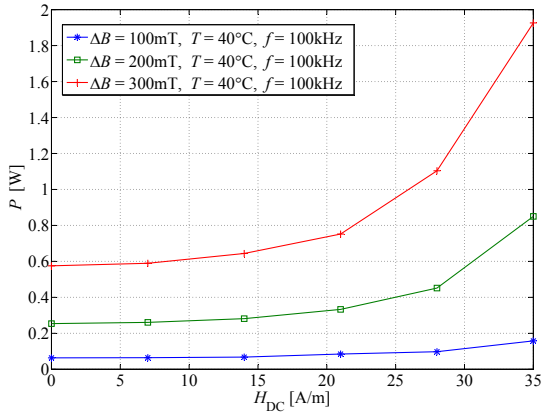


**Figure 3.28:** Core losses under DC bias conditions; material VITROPERM 500F (VAC); core: W452;  $f = 100\text{ kHz}$ ,  $T = 40^\circ\text{C}$ .

### 3.7.4 Core Losses under DC Bias Conditions of Different Materials

Different materials have been tested to gain information how core losses are influenced by a premagnetization. Measurements on the nanocrystalline material VITROPERM 500F and on a molypermalloy powder core (Magnetics MPP 300u) and cores of silicon steel (tested: M165-35S grain-oriented steel with lamination thickness 0.35 mm, M470-50A non-oriented steel with lamination thickness 0.5 mm) have been conducted. The measurements on the silicon steel cores have been performed up to a DC magnetic flux density of 1 T, which is before the core starts to saturate. A loss increase of approximately 50 % has been observed. The tested powder core (Magnetics MPP 300u; part number: C055433A2) has been tested up to a DC magnetic field strengths of 1200 A/m; up to that operating point the loss change is negligibly small.

Losses in the nanocrystalline material VITROPERM 500F from Vacuumschmelze increase under DC bias condition, as can be seen in Figure 3.28. The SPGs of the material VITROPERM 500F and of some more ferrites are given in Appendix A.3. In Table 3.7 an overview of the tested materials is given. The reason for the distinctive behavior of each material class hasn't been studied for this work and could be investigated as part of future work. Tests have been performed only on

| Material Class       | Measured Material(s)   | Impact on Losses |
|----------------------|--|------------------|
| Soft Ferrites        | EPCOS N87, N27, T35<br>Ferroxcube 3F3                        | very high        |
| Nanocrystalline      | VITROPERM 500F (VAC)   | yes              |
| Silicon Steel        | M470-50A non-oriented steel<br>M165-35S grain-oriented steel | yes              |
| Molypermalloy Powder | Magnetics MPP300   | negligible       |

**Table 3.7:** Impact of DC bias to core losses, an overview of different material classes.

the above listed components; hence, a general declaration of the whole material class cannot be made with 100 % certainty.

### 3.7.5 Conclusion and Future Work

A graph that shows the dependency of the Steinmetz parameters ( $\alpha$ ,  $\beta$  and  $k$ ) on premagnetization, i.e. the *Steinmetz Premagnetization Graph* (SPG) has been introduced. Based on the SPG, the calculation of core losses under DC bias condition becomes possible. For the considered frequency range it is shown that the graph is independent of the frequency  $f$ . This new approach how to describe losses under DC bias condition is promising due to its simplicity. Graphs are given for different materials and different operating temperatures.

Furthermore, different material classes have been tested to gain information how core losses are influenced by a premagnetization. Measurements on molypermalloy powder, silicon steel, nanocrystalline material, and ferrite cores have been performed.

## 3.8 Minor and Major B-H Loops

In the previous sections, different aspects of core loss modeling have been discussed; it became clear how to model core losses of a single B-H loop of different shape. However, in many power electronic applications, e.g. in PFC rectifiers, a high frequency flux ripple is superimposed on a

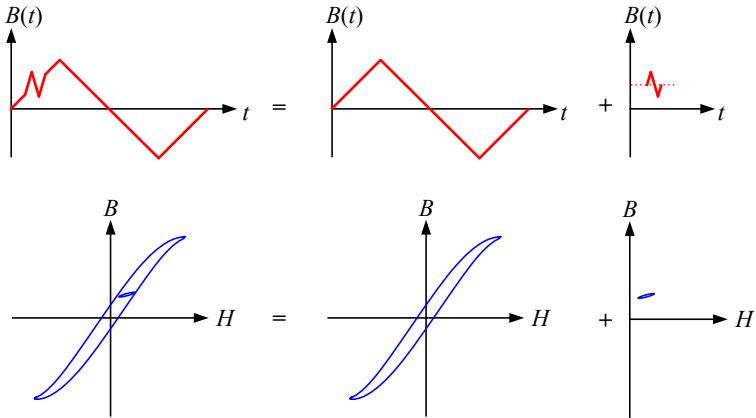


**Figure 3.29:** Illustration of minor and major loop separation.

low frequency flux waveform. When plotting the traversed B-H-curve, one sees a large loop and many small loops, i.e. one large major loop and many small minor loops. The large loop originates in the fundamental current waveform, while the small loops originate in the HF ripple. According to [10, 35], the total loop can be separated into its major and minor loops and then the loss energy of each loop can be calculated independently and summed. The concept is illustrated in Figure 3.29. This has been experimentally verified in [10, 35]. In the following, measurement results are presented to reconfirm the concept.

This loop separation has been confirmed on the amorphous alloy 2605SA1 from Metglas (core PowerLite AMCC8) as core material. The measured current waveform consists of a sinusoidal low frequency part and, superimposed to it, piecewise-linear high frequency segments, as plotted in Figure 3.30. The flux waveform can be divided into its fundamental flux waveform and into piecewise linear flux waveform segments. The loss energy is then calculated for the fundamental and all piecewise linear segments, summed and divided by the fundamental period length in order to determine the average core loss. Actually, when doing this, one does not consider how the minor loop closes: each piecewise linear segment is modeled as having half the loss energy of its corresponding closed loop. This leads to a high accuracy, as measurements confirm.

For the loss energy calculation of each piecewise linear flux segment and for the fundamental waveform, a loss map has been built up in

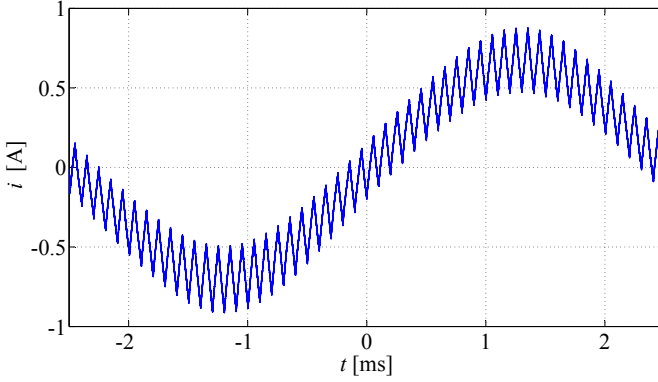


**Figure 3.30:** Measured (and low-pass filtered) current waveform of superposition experiment;  $f_{\text{LF}} = 200$  Hz,  $\Delta B_{\text{LF}} = 1.2$  T (peak-to-peak),  $f_{\text{HF}} = 10$  kHz, and  $\Delta B_{\text{HF}} = 0.2$  T (peak-to-peak).

| Operating Point  | Loss cal. [W] | Loss meas. [W] |
|--|---------------|----------------|
| $f_{\text{LF}} = 200$ Hz, $\Delta B_{\text{LF}} = 1.2$ T | 0.82          | 0.76           |
| $f_{\text{HF}} = 10$ kHz, $\Delta B_{\text{HF}} = 0.2$ T |               |                |
| $f_{\text{LF}} = 50$ Hz, $\Delta B_{\text{LF}} = 2$ T    | 2.27          | 2.14           |
| $f_{\text{HF}} = 10$ kHz, $\Delta B_{\text{HF}} = 0.4$ T |               |                |

**Table 3.8:** Results of minor major loop measurements.

advance. For it, sinusoidal low frequency measurements and triangular high frequency measurements at different operating points have been performed first. How exactly such a loss map is built up and used will be discussed in the next section.

The calculated losses for different operating points agree well with measurements, as can be seen in Table 3.8.

### 3.9 Hybrid Core Loss Calculation Approach

In the previous sections, different aspects of core loss modeling have been discussed. With the derived knowledge it is now possible to ac-

curately determine core losses in inductive components employed in power electronic systems. In order to improve the model accuracy a loss database has been built up. The applied core loss approach can be seen as a hybrid of the improved version of the empirical Steinmetz equation (i<sup>2</sup>GSE) and an approach based on a material loss database, i.e. a loss map.

As mentioned in Section 3.3, until core manufacturers provide data for loss calculation based on i<sup>2</sup>GSE, SPG, or DPF, core losses can be calculated with a loss map that is based on measurements. This loss map stores the loss information for different operating points, each described by the flux density ripple  $\Delta B$ , the frequency  $f$ , the temperature  $T_c$ , and a DC bias  $H_{DC}$ . This has been implemented e.g. in [37, 38, 39]. This approach is independent of a parameter set, e.g. Steinmetz parameter set, hence a higher accuracy over a wide frequency and flux density range can be expected since the problem that Steinmetz parameters are only valid for a limited frequency and flux density range does not appear. A novel loss map structure has been developed in the course of this thesis and will be presented within this section.

The loss map stores loss densities (in our case losses per volume) as the data should be applicable for all different type of core shapes. A core with homogenous flux density distribution is basically needed for measuring loss densities. This would be the case when having an "ideal" toroid with very small radial thickness. If the radial thickness is not small, the flux density is not distributed homogeneously over the radius and the situation is more complicated. In this case "effective" dimensions (effective length  $l_e$  and effective cross-sectional area  $A_e$ ) are needed to permit calculation as if it were an ideal toroid. The core losses per volume can then be extracted by dividing the measured losses by the effective volume of the core  $V_e = A_e l_e$ . These effective dimensions for a toroid can be calculated as (cf. Section 3.10)

$$A_e = \frac{h \ln^2 r_2 / r_1}{1/r_1 - 1/r_2}, \quad (3.36)$$

and

$$l_e = \frac{2\pi \ln r_2 / r_1}{1/r_1 - 1/r_2}. \quad (3.37)$$

After it has been clarified on what cores measurements for setting up a loss map can be performed, it has to be further discussed what type of waveforms are to be measured. In some applications, e.g. PFC

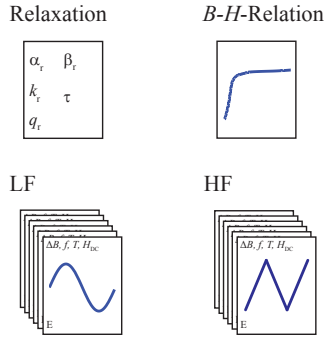


**Figure 3.31:** Content of loss map.

rectifiers, a high frequency (piecewise-linear) flux ripple is superimposed to a low frequency (sinusoidal) flux waveform. This well illustrates the typical situation in modern power electronic systems: the low frequency fundamental waveform usually has a sinusoidal shape, while the high frequency ripple consists of piecewise-linear segments. The B-H loop of the low frequency fundamental flux part is called the major loop, while the high frequency loops are called minor loops. According to the discussion in Section 3.8, the flux waveform can be divided into its fundamental flux waveform and into piecewise linear flux waveform segments. The loss energy is then calculated for the fundamental and all piecewise linear segments, summed and divided by the fundamental period length in order to determine the average core loss. As mentioned before, when doing this, one does not consider how the minor loop closes: each piecewise linear segment is modeled as having half the loss energy of its corresponding closed loop. This led to a high accuracy, as measurement have confirmed.

Loss information for different operating points is stored in the loss map, each described by the flux density ripple  $\Delta B$ , the frequency  $f$ , the temperature  $T_c$ , and a DC bias  $H_{DC}$ . On the basis of the above discussion, sinusoidal waveform measurement results are stored for frequencies below 1 kHz and triangular, i.e. piecewise-linear, waveform measurement results are stored for frequencies above 1 kHz. The classification limit of 1 kHz has been selected as 1 kHz is slightly above the fundamental frequency of the mains in modern aircraft (up to 800 Hz [49]). In addition, the loss database contains the initial B-H curve and one

set of relaxation parameters  $\alpha_r$ ,  $\beta_r$ ,  $k_r$ ,  $\tau$ , and  $q_r$ . The extraction of the relaxation parameters has been carried out as described in Section 3.6. The initial B-H curve enables introducing a reluctance model that takes the non-linearity of the core material into consideration (cf. Chapter 2). The relaxation parameters permit the taking of relaxation effects into consideration by using the i<sup>2</sup>GSE (3.25). In Figure 3.31 an overview of the loss map content is illustrated. The B-H relation as well as the loss map operating points have to be measured and stored at different temperatures in order to consider the temperature behavior of the core material.

### 3.9.1 Use of Loss Map

As mentioned before, the applied core loss approach in this work can be described as a hybrid of the Steinmetz approach and a loss map approach: a loss map is taken in order to provide accurate parameters for the i<sup>2</sup>GSE or SE. This principle is illustrated in Figure 3.32. The fundamental principle of the implemented hybrid approach can also be interpreted differently: a loss map is taken to calculate core losses, while the interpolation and extrapolation between operating points is made with the SE or the i<sup>2</sup>GSE.

The flux density waveform for which the losses have to be calculated could, for instance, be simulated in a circuit simulator. This simulated waveform is then broken up into its fundamental (mostly sinusoidal) flux waveform and into piecewise linear flux waveform segments, as illustrated in Figure 3.32. The loss energy is then calculated for all segments, summed and divided by the fundamental period length. The piecewise-linear waveforms are translated into a symmetric triangular flux waveform with the same peak-to-peak flux density  $\Delta B$ , the same flux density slope  $dB/dt$  and the same DC premagnetization  $H_{DC}$ , resulting in a symmetric triangular operating point that is defined as  $(\Delta B^*, f^*, H_{DC}^*, T_c^*)$ . The translation is necessary as the loss map stores operating points of symmetric triangular waveforms.

The losses to the (sinusoidal or triangular flux waveform) operating point  $(\Delta B^*, f^*, H_{DC}^*, T_c^*)$  are calculated by the following steps:

1. The close-by operating points of the loss map have to be found. Nine operating points are necessary for the interpolation: three for the interpolation of  $f$  and  $\Delta B$ , multiplied by three for the interpolation of the temperature  $T_c$  and DC magnetic field strength

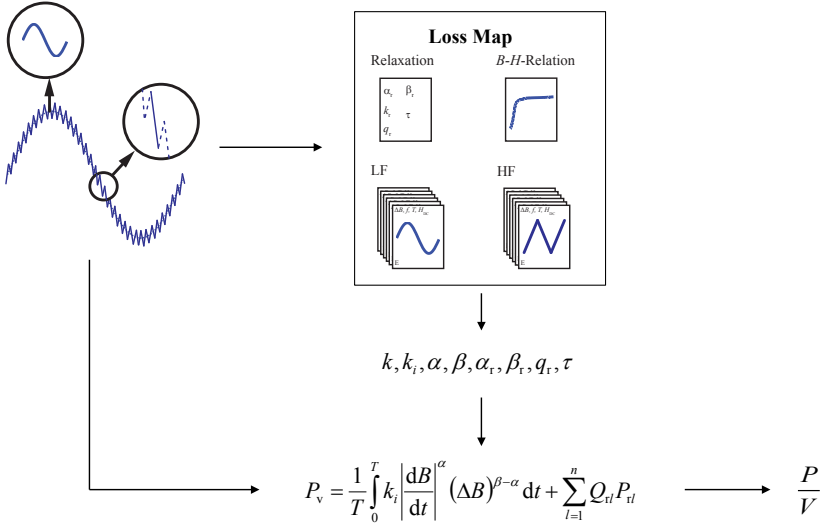


**Figure 3.32:** Illustration of hybrid approach: a loss map is built in order to provide accurate parameters for the  $i^2$ GSE or SE.

$H_{DC}$ . This is illustrated in Figure 3.33 and will be discussed below.

2. In a second step, a linear interpolation for the temperature  $T_c$  and the DC magnetic field strength  $H_{DC}$  is performed. This is illustrated in Figure 3.33(a) and carried out for each pair  $\Delta B/f$ . Therefore the following points are derived:  $(\Delta B_1, f_1, H_{DC}^*, T_c^*)$ ,  $(\Delta B_2, f_1, H_{DC}^*, T_c^*)$ ,  $(\Delta B_1, f_2, H_{DC}^*, T_c^*)$ , i.e. three operating points remain with inter-/extrapolated temperature  $T_c$  and magnetic field strength  $H_{DC}$ .
3. The peak-to-peak flux density  $\Delta B$  and the frequency  $f$  are inter-/extrapolated by extracting the Steinmetz parameters from the three remaining operating points and calculating the losses by the SE (in the case of a sinusoidal flux waveform) or the  $i^2$ GSE (in the case of a piecewise linear waveform). This is illustrated in Figure 3.33(b). The relaxation term of the  $i^2$ GSE can directly be evaluated with the relaxation parameters from the loss map; for this, information about the antecedent piecewise-linear flux phase

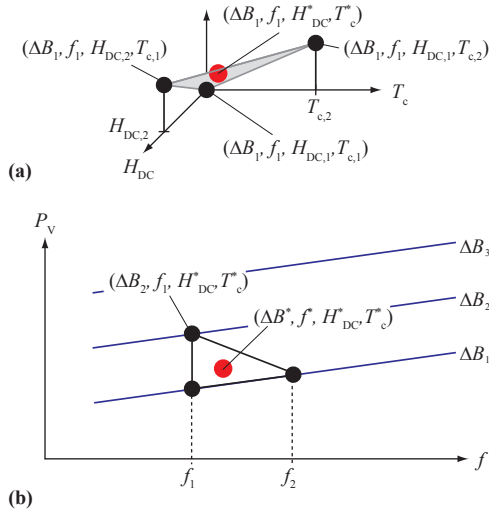


**Figure 3.33:** Illustration of interpolation.

is required.

This hybrid approach already enables a high degree of accuracy for a limited number of pre-measured operating points in the loss map as the inter/extrapolation by the SE or  $i^2$ GSE takes the basic core loss behavior into account.

As the frequency increases, the loss map operating points change from sinusoidal to triangular waveforms; hence, for the Steinmetz extraction the curve fitting function changes from the SE to the  $i^2$ GSE. In one case the Steinmetz parameter  $k$ , and in the other case the Steinmetz parameter  $k_i$  is extracted. However, with (3.5) they can be translated into each other.

### 3.10 Influence of Core Shape on Core Losses

The Steinmetz equation and its improvements, such as the  $i^2$ GSE, give information about losses per volume (or per weight). But, simply multiplying the loss density by the volume may lead to substantially wrong results. Within this section it is discussed how to model core losses of cores of general shape.

In a first step, in Section 3.10.1, it is given how to calculate the effective dimensions of a toroid in order to perform calculations as if the flux density distribution were homogenous. These effective dimensions are important to characterize core materials, as they allow determining the loss densities (loss per volume or loss per weight) of a material from the measured losses. Later, in Section 3.10.2, it is analyzed how the core losses for cores of general shapes can be calculated. By introducing a reluctance model of the core, and with it, calculating the flux density in every core section of (approximately) homogenous flux density, one can calculate the losses of each core section. The core losses of each section are then summed to obtain the total core losses. This leads to a generally high accuracy. However, under certain circumstances, in tape wound cores a flux orthogonal to the tape layers can lead to high eddy currents and therewith to high core losses. This will be discussed in Section 3.10.5. Additionally, discussions about eddy-current losses in general and dimensional resonance are given in Section 3.10.3 and Section 3.10.4 respectively.

### 3.10.1 Effective Dimensions of Toroidal Cores

When considering an ideal toroid with a very small radial thickness, it is possible to speak of its magnetic lengths  $l$  and cross section  $A$ . In case the radial thickness is not small, the flux density is not homogeneously distributed over the radius, and the core property is more complicated. However, it is possible to find effective dimensions  $l_e$  and  $A_e$ , which allow to proceed calculations as if it were an ideal toroid. When measuring core losses of a toroid, one can approximate the core losses per volume with these effective dimensions. The flux in the core divided by the effective cross-sectional area  $A_e$  gives an average flux density. This allows approximating the core losses per volume to this flux density.

The effective dimensions for toroidal cores are

$$A_e = \frac{h \ln^2 r_2/r_1}{1/r_1 - 1/r_2}, \quad (3.38)$$

and

$$l_e = \frac{2\pi \ln r_2/r_1}{1/r_1 - 1/r_2}. \quad (3.39)$$

The derivation of (3.38) and (3.39) is given in Appendix A.6.

These effective dimensions are important to characterize core materials, as they allow determining the loss densities (loss per volume or loss per weight) of a material from the measured losses.

### 3.10.2 General Core Shape

[22] proposes a method to find the dimensions  $l_e$  and  $A_e$  for general core shapes, which allows to calculate the inductance value as if it were an ideal toroid. The variation of permeability with field strengths is neglected, and the core is divided into sections with approximately constant flux densities. Core factors are introduced as

$$C_1 = \sum_i \frac{l_i}{A_i}, \quad (3.40)$$

and

$$C_2 = \sum_i \frac{l_i}{A_i^2}, \quad (3.41)$$

where  $l_i$  and  $A_i$  are the length and cross section of section  $i$ . The effective dimensions are then

$$l_e = \frac{C_1^2}{C_2} \quad (3.42)$$

and

$$A_e = \frac{C_1}{C_2}. \quad (3.43)$$

These effective dimensions are only suitable for an inductance calculation and may lead to substantial errors in loss estimation. For instance in case of an E-core, a simple multiplication of the loss density with  $A_e$  and  $l_e$  leads to wrong loss values. This is because the flux density is not uniform at every position of the core. The calculation of losses with effective dimensions is only valid in case of an uniform flux density distribution.

The core losses have to be calculated differently. By setting up a reluctance model of the core, and with it, calculating the flux density in every core section of (approximately) homogenous flux density, one can calculate the losses of each core section. The core losses of each section are then summed to obtain the total core losses. This also allows to consider an air gap. How to set up a reluctance model has been shown

| Working Point<br>( $\Delta B$ ; $f$ ; $H_{DC}$ ) | Loss Density<br>[kW/m <sup>3</sup> ] | Steinmetz<br>Parameters |
|--|--------------------------------------|-------------------------|
| (0.05 T; 50 kHz; 0 A/m)                          | 3.09                                 | $k_i = 6.84$            |
| (0.05 T; 100 kHz; 0 A/m)                         | 6.89                                 | $\alpha = 1.16$         |
| (0.1 T; 100 kHz; 0 A/m)                          | 36.5                                 | $\beta = 2.41$          |

**Table 3.9:** Steinmetz parameters of material EPCOS N87.

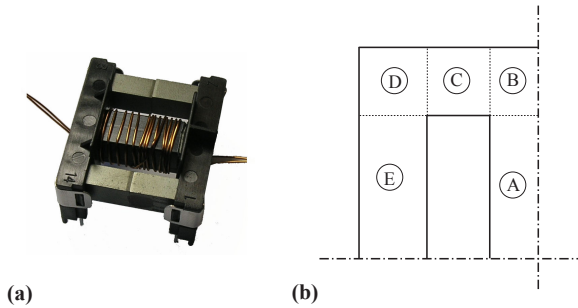


**Figure 3.34:** Photo and the section segmentation of the core under test EPCOS B66319G0X187.

in Chapter 2. The fact that the flux density in core parts very close to the air gap is (slightly) reduced as part of the flux already left the core has been neglected. In the following, some experimental results, which illustrate and confirm this approach, are given.

In a first step, the selected material is characterized, i.e. the core loss densities of the selected material are measured on a toroid. The material N87 from EPCOS has been selected, and the characterizing measurements have been conducted on the toroidal core EPCOS B64290L22X87 [29]. The effective magnetic length  $l_e$  and effective core cross section  $A_e$  are 103 mm and 95.75 mm<sup>2</sup> respectively. The Steinmetz parameters have been extracted from three operating points. They are given in Table 3.9, where  $k_i$  is the parameter of (3.4).

The core for which the core losses are calculated is the E-core EPCOS B66319G0X187. In Figure 3.34 a photo and the section segmentation of the core are given. For every core section the length  $l_i$  and cross section in  $A_i$  is calculated as proposed in Figure 2.10. The results

| Section | $l_i$ [mm] | $A_i$ [mm <sup>2</sup> ] |
|---------|------------|--------------------------|
| A       | 9.7        | 26.3                     |
| B       | 3.6        | 33.2                     |
| C       | 6.2        | 40.2                     |
| D       | 4.2        | 39.2                     |
| E       | 9.7        | 38.3                     |

**Table 3.10:** Dimensions of core EPCOS B66319G0X187.

are summarized in Table 3.10. The peak-to-peak flux  $\Delta\phi$  in one outer leg is calculated as

$$\Delta\phi = \Delta B \cdot A_A, \quad (3.44)$$

where  $A_A$  is the cross section of core section A. Note that section A of the core represents only half of the middle leg (symmetry).  $\Delta B$  represents the peak-peak flux density in the middle leg. With it, in every section the flux density can be calculated as

$$\Delta B_i = \frac{\Delta\phi}{A_i}. \quad (3.45)$$

The losses per core section for a triangular current shape can be calculated with (3.33) as

$$P_i = l_i \cdot A_i \cdot k_i (2f)^\alpha \Delta B_i^\beta. \quad (3.46)$$

The total core losses, including the right leg, are then

$$P = 2 \cdot (2P_A + 2P_B + 2P_C + 2P_D + 2P_E). \quad (3.47)$$

The calculated losses for different operating points agree well with measurements, as can be seen in Table 3.11.

### 3.10.3 Impact of Core Shape on Eddy Current Losses

An alternating magnetic flux inside the core material induces an electric field which leads to eddy currents and, consequently, to eddy current core losses. Eddy current core losses are referred to the losses that originate from Maxwell's equation when the presence of magnetic domains is ignored, i.e. only the macroscopic net magnetization is considered.

| Working Point<br>( $\Delta B; f$ ) $H_{DC} = 0$ | Loss Meas.<br>[mW] | Loss Cal.<br>[mW] |
|---|--------------------|-------------------|
| (0.1 T; 50 kHz)                                 | 42.7               | 40.9              |
| (0.1 T; 100 kHz)                                | 91.6               | 91.2              |
| (0.15 T; 50 kHz)                                | 117                | 108               |
| (0.15 T; 100 kHz)                               | 257                | 242               |
| (0.2 T; 50 kHz)                                 | 233                | 217               |
| (0.2 T; 100 kHz)                                | 509                | 483               |

**Table 3.11:** Results of loss calculations and measurements of core EPCOS B66319G0X187; Steinmetz parameters from Table 3.9.

Eddy currents and their corresponding losses depend a lot on the electrical conductivity and geometry of the core. In case of a core material with high electrical conductivity, eddy currents of high magnitude are induced; these eddy currents lead to high core losses. The material can be divided into electrically insulated segments, e.g. laminations or grains, in order to reduce eddy current losses. The eddy current losses per unit volume depend then not on the shape of the bulk material, but on the size and geometry of the insulated regions [22]. Particularly, iron-based material (e.g. silicon steel) has to be laminated in order to limit eddy current losses.

The eddy currents are such that the magnetic field generated by them is opposed to the applied magnetic field. In other words, the eddy currents have a shielding effect: the resulting magnetic field, which is the sum of the applied field and the field originating from eddy currents, decreases exponentially towards the inside of the core. The distance from the outer boundary to where the resulting magnetic field has fallen to  $1/e$  of the outer boundary field value, is called the skin depth (or penetration depth)  $\delta$ , and can be calculated as [5]

$$\delta = \frac{1}{\sqrt{\pi\mu\sigma f}}, \quad (3.48)$$

where  $\mu$  is the permeability of the core material,  $\sigma$  is the conductivity of the core material, and  $f$  is the frequency of the sinusoidal applied magnetic field. At lower frequencies, where the applied field penetrates (almost) the entire core, the eddy current losses per unit volume for

| Geometry                     | $k_{ec}$ |
|------------------------------|----------|
| laminations of thickness $d$ | 6        |
| cylinder of diameter $d$     | 16       |
| sphere of diameter $d$       | 20       |

**Table 3.12:** The eddy current loss coefficient  $k_{ec}$  for some geometries.

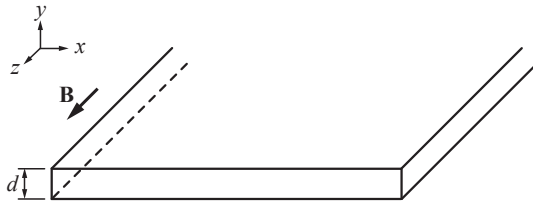


**Figure 3.35:** Geometry of considered lamination layer.

sinusoidal excitation can be calculated with [22]

$$P_{ce} = \frac{(\pi \hat{B} f d)^2}{k_{ec} \rho}, \quad (3.49)$$

where  $\hat{B}$  is the peak value of the flux density, which is perpendicular to the plane with cross-sectional dimension  $d$ ,  $\rho$  is the resistivity of the core material, and  $k_{ec}$  is a dimensionless eddy current loss coefficient. The eddy current loss coefficients for some geometries are given in Table 3.12. The power loss density of the lamination geometry shown in Figure 3.35 is then calculated as

$$P_{ce} = \frac{(\pi \hat{B} f d)^2}{6\rho} = \frac{\pi^2}{6} \hat{B}^2 f^2 d^2 \sigma, \quad (3.50)$$

where  $\sigma$  is the conductivity of the core material. The same equation has been derived in [33]. In case of a solid material or at very high frequencies, where eddy currents shield the applied magnetic field to entirely penetrate the core material, other equations than (3.49) or (3.50) have to be taken. Equations for these situations are given e.g. in [5, 33].

One important conclusion of the above discussion is the fact that, in case of laminated iron cores or tape wound cores such as amorphous

or nanocrystalline iron material, it is still appropriate to calculate with core loss densities that have been measured on a sample core with a geometrically different bulk material, but with the same lamination or tape thickness. This is because the eddy current losses per unit volume depend on the size and geometry of the insulated regions and not on the geometry of the core itself. In other words, it is appropriate to set up a reluctance model, calculate the flux density in each core section of approximately homogenous flux density and calculate the core losses based on a previously measured loss density.

In iron based core materials, the skin depth  $\delta$  is small and the core has to be laminated in order to prevent from high core losses. Ferrites, on the other hand, are usually considered as homogeneous materials with respect to eddy current losses [22]. However, the conductivity  $\sigma$ , in return, is much smaller and eddy current core losses can be neglected in most practical cases. Typical resistivity values for Manganese Zinc (MnZn) ferrites are in the range of 2...100  $\Omega\text{m}$  [31]. The dominating loss effects in ferrites are the static hysteresis and residual (relaxation) losses. However, there might be situations in which eddy current losses are not negligible; particularly at very high frequencies, in cores with a relative high conductivity and with large cross sectional area, eddy currents are observed. For instance, in [50] measurements on different ferrite materials on different toroidal core sizes have been conducted. On the material 3E6 from Ferroxcube with a comparably low resistivity of 0.1  $\Omega\text{m}$  [51] the loss density increased about 50% at 100 kHz when the toroid is changed from size R16 to size R36. In such situations, it is important to extract the loss density for the loss map on small core samples where the eddy currents are still low. In the modeling process of larger cores, eddy current losses, calculated with (3.49), are added to the core losses subsequently. However, in most practical cases, eddy currents can be neglected in ferrites.

### 3.10.4 Dimensional Resonance

In MnZn ferrites at very high frequencies dimensional resonances may occur in which standing electromagnetic waves are established [22, 30, 52]. A greater amount of energy is then dissipated. In [52] it was discovered that the observed permeability of brick-shaped core samples decrease rapidly to a very low value at about 2 MHz. The reason is that the very high permittivity  $\epsilon$  and the high permeability  $\mu$  leads to

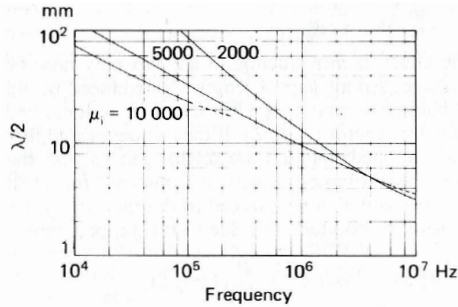


**Figure 3.36:** Dimensional resonance in MnZn ferrite cores, calculated from typical properties and three different permeabilities. If the smallest cross-sectional dimension of the core is half of the wavelength  $\lambda$  then the fundamental mode standing wave will be established. Figure copied from [22].

relatively low wavelengths of electromagnetic waves.

The wavelength  $\lambda$  in a loss-free medium is

$$\lambda = \frac{1}{f\sqrt{\mu\epsilon}}, \quad (3.51)$$

where  $\mu$  is the permeability of the medium,  $\epsilon$  is the permittivity of the medium, and  $f$  is the frequency of the electromagnetic wave. In a typical MnZn ferrite the permeability is  $\mu = 10^3\mu_0$  and the permittivity is  $\epsilon = 10^5\epsilon_0$  [22]. This leads to a wavelength of  $\lambda = 30$  mm at a frequency of 1 MHz. If the smallest cross-sectional dimension of the core is half of the wavelength then the fundamental mode standing wave will be established [22]. In case of a dimensional resonance, the observed permeability is decreasing to a very low value. The frequencies at which dimensional resonances occur differ if the medium is not loss-free. In Figure 3.36 the according wavelengths of a typical MnZn ferrite as a function of the frequency are given.

This topic is somewhat outside the scope of this thesis, as the effect occurs mainly at very high frequencies in the megahertz range. However, in case of very large core samples, the frequencies where dimensional resonance occurs drops and therefore, for the sake of completeness, one should be aware of the existence of dimensional resonances.

### 3.10.5 Losses in Gapped Tape Wound Cores

The core losses can be calculated based on an accurate reluctance model, which, if needed, consists of an accurate air gap reluctance. However, it has been found that gapped cores of amorphous alloys or nanocrystalline materials show a behavior that cannot be modeled by a reluctance model: gapped tape wound cores have higher core losses compared to un-gapped cores [53, 54, 55, 56, 57]. There are two causes assumed to be dominant for this distinctive behavior: (1) in the cutting process, interlamination short circuits may be introduced (insulation layer damage) and (2) flux lines that are orthogonal to the lamination layers due to fringing flux. Both effects would result in higher eddy-current core losses.

In [53] a doubling of the core losses of an iron-based amorphous alloy after the cutting process has been observed. However, additional core losses could be partly reduced by polishing the cut surface after the cutting process. In [57], the cut core has been put in an 40% ferric chloride solution, in order to remove short circuits introduced by the cutting process. The losses could be substantially (more than 50%) decreased. Both cited papers confirmed the existence of interlamination short circuits and showed a way how to (partly) get rid of them.

The second cause for this distinctive behavior has been observed, for instance, in [55, 56, 57]. In [55, 56] it has been observed that the core losses in amorphous cut cores with air gaps increase with an increase of the air gap length. This increase has been attributed to the in-plane eddy-current losses generated by the fringing flux perpendicular to the layers of the tape wound cores. Losses originating in flux lines orthogonal to the layers of the tape wound core have also been observed in [57], where their existence has been confirmed with an experiment which is illustrated in Figure 3.37. Two core halves of nanocrystalline core material are taken, one of the halves is shifted, first in horizontal, later in vertical direction. In case of a shift in horizontal direction a flux orthogonal to the layers of the tape wound core close to the region of contact occurs, while in the case of a shift in vertical direction no orthogonal flux is generated. As can be seen in Figure 3.37(c), in case of an orthogonal flux, the core losses substantially increase. These experiments have also been conducted with ferrites, where no difference between the two shift directions has been observed. The results with the tape wound cores show clearly that an orthogonal flux substantially increases core losses in these types of core. In [57] it is furthermore

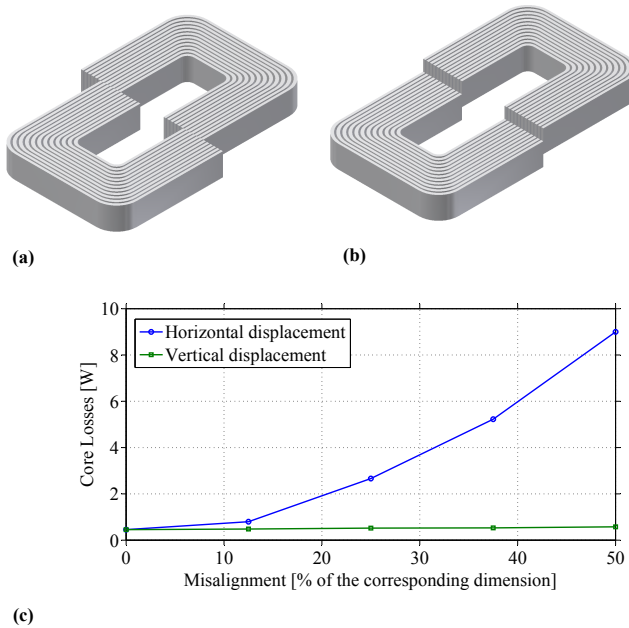


**Figure 3.37:** Displacement of the core halves in (a) horizontal direction or (b) vertical direction. (c) Results. Figures from [57].

pointed out that the leakage flux in transformers built of tape wound cores may generate significant core losses.

In [54] the loss increase in cut tape wound cores has been observed as well. However, an increase in the air gap length didn't lead to a further core loss increase. A possible explanation can be given by the fact that there is a trade-off between the two causes: an increase of the air gap length results in more orthogonal flux; however, on the other hand, the flux through the cut surface, where the short circuits are located, is reduced. It seems that in [54] the two effects balance each other.

For the sake of completeness, it should be briefly discussed why in stacked laminated iron cores, e.g. silicon steel cores, the effect of a loss increase in gapped cores is much smaller. It is obvious that interlamination short circuits are not present in these type of cores (different machining process, mechanically less fragile). Furthermore, the layer

orientation is different; the laminations are normally stacked, hence, the flux through the core window doesn't lead to a flux orthogonal to the layer.

In this thesis only a brief overview about this important topic is given. The interested reader is referred to the cited articles. This topic gives opportunities for further research, since, to the author's knowledge, there exists no approach which allows analytically describing the presented effects.



## Chapter 4

# Winding Loss Modeling

The second source of losses in inductive components is the ohmic losses in the windings. The resistance of a conductor increases with an increase of frequency due to eddy currents. Self-induced eddy currents inside a conductor lead to the skin-effect. Eddy currents due to an external alternating magnetic field, e.g. the air gap fringing field or the magnetic field from other conductors, lead to the proximity effect. In order to limit losses related to skin- and proximity effects, a careful winding design is important.

Most windings are realized with solid round conductors since they are low priced. However, in return, they have high skin- and proximity-effect losses. In order to reduce these high frequency (HF) losses, different other types of windings are available, such as foil and litz wire windings. However, there are situations in which foil or litz wires are even lossier than solid round windings. The winding arrangement is another degree of freedom that allows controlling winding losses. For instance, interleaved transformer windings substantially reduce proximity-effect losses.

In Section 4.1 and Section 4.2 the skin- and proximity-effects are qualitatively explained. Later, the different winding types are discussed, including a discussion about the determination of the external magnetic field which is needed in order to calculate the proximity-effect losses. In Section 4.3 round conductors (including litz wires in Section 4.3.5), and in Section 4.4 foil conductors are discussed. Analytical equations are given which allow calculating winding losses.

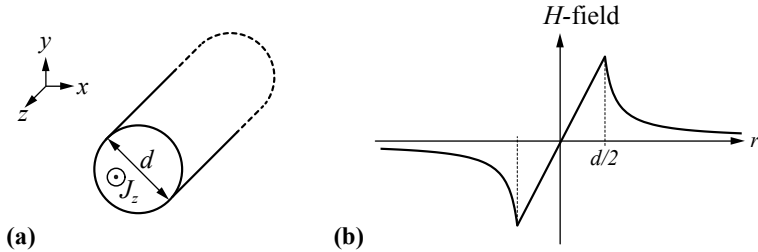


**Figure 4.1:** (a) Cross section of a round conductor that is infinitely long in the  $z$ -direction with homogenous current density  $J_z$ . (b) Magnitude of the corresponding  $H$ -field.

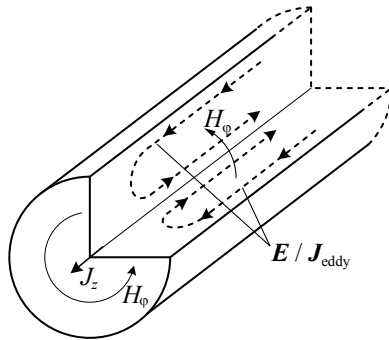


**Figure 4.2:** Self-induction of eddy currents due to Faraday's law.

## 4.1 Skin Effect

The magnetic field of a current through a conductor can be determined with Ampere's law. Ampere's law is given as

$$\oint \mathbf{H} d\mathbf{l} = \iint \mathbf{J} d\mathbf{A}, \quad (4.1)$$

where  $\mathbf{H}$  is the magnetic field strength vector and  $\mathbf{J}$  is the current density vector. The magnitude of the resulting  $H$ -field of a current through a round conductor is qualitatively illustrated in Figure 4.1.

In case the current through the conductor is an alternating current (AC), the associated alternating magnetic field self-induces an electric field inside the conductor. Faraday's law of induction is the basic law

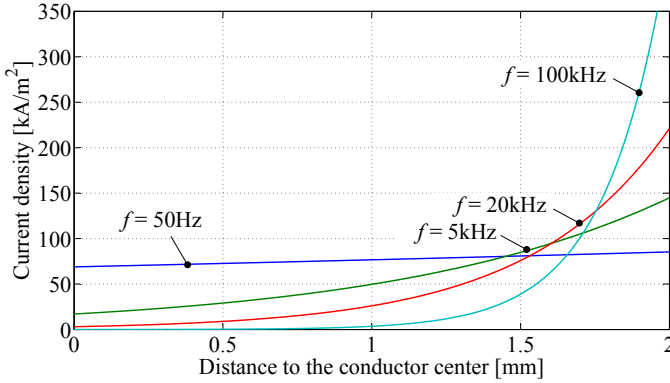


**Figure 4.3:** Current distribution for different frequencies in a round conductor with a radius of 2 mm. The current magnitude is 1 A.

that describes this effect; it is given as

$$\oint \mathbf{E} d\mathbf{l} = -\frac{d}{dt} \iint \mathbf{B} d\mathbf{A}, \quad (4.2)$$

where  $\mathbf{E}$  is the electric field vector and  $\mathbf{B}$  is the magnetic flux density vector. The effect in case of a round conductor is illustrated in Figure 4.2. The induced electric field results in a current, which counteracts the excitation current in the center of the conductor, hence, the major part of the current is flowing in an outer layer (skin) of the conductor. This change in the current distribution is illustrated in Figure 4.3 for different frequencies using the example of a round conductor.

The current density is decreasing from the outer conductor boundary to the conductor center. The distance from the outer boundary to where the current density falls to  $1/e$  of the maximum is called the skin depth (or penetration depth)  $\delta$ , and, for  $\mu_r = 1$ , can be approximated as [5]

$$\delta = \frac{1}{\sqrt{\pi\mu_0\sigma f}}, \quad (4.3)$$

where  $\mu_0$  is the magnetic constant,  $\sigma$  is the conductivity of the conductor material, and  $f$  is the frequency of the sinusoidal current. The assumption that  $\mu_r$  is one is valid for conductor materials such as copper, aluminum, etc. As a simplification, the current can be considered

as concentrated in a skin layer with width  $\delta$  and with a constant current density.

The skin-effect losses (including DC losses) per unit length can be calculated as

$$P_S = F_{R/S}(f) \cdot R_{DC} \cdot \hat{I}^2, \quad (4.4)$$

where  $R_{DC}$  is the DC resistance,  $\hat{I}$  is the peak current, and  $F_{R/S} = R_{AC}/R_{DC}$  is a factor that describes the increase of the conductor resistance due to the skin effect. Different formulae for  $F_{R/S}(f)$  are taken for different conductor geometries, whereas the subscribed letter stands for the conductor type (e.g.  $F_R(f)$  for round conductors).

The term "skin-effect losses"  $P_S$  describes the losses due to the current through the conductor, including the losses due to self-induced eddy currents. Therewith, the DC losses are included in the skin-effect losses.

## 4.2 Proximity Effect

The proximity effect is illustrated in Figure 4.4 using the example of a round conductor. A current in conductor A results in a magnetic field that induces eddy currents in conductor B. On the facing side, the induced current in conductor B has a direction opposite to the current in conductor A. In other words, the current distribution of a conductor that is penetrated by an external magnetic field changes and additional winding losses occur. The induced current distribution of a round conductor is illustrated in Figure 4.5 for different frequencies. In Figure 4.6 the current density of two neighboring conductors is illustrated; in Figure 4.6(a) the currents have opposite directions, while in Figure 4.6(b) both conductors have the same current direction. As can be seen, the current concentrates there where the magnetic field  $H$  concentrates.

The losses due to the proximity effect are described as

$$P_P = R_{DC} \cdot G_{R/S}(f) \cdot \hat{H}_e^2, \quad (4.5)$$

where  $R_{DC}$  is the DC resistance,  $\hat{H}_e$  is the peak external magnetic field, and  $G_{R/S}(f)$  is a factor that describes the amount of winding losses due to the proximity effect. Different formulae for  $G_{R/S}(f)$  are taken for different conductor geometries, whereas the subscribed letter stands for the conductor type (e.g.  $G_R(f)$  for round conductors).

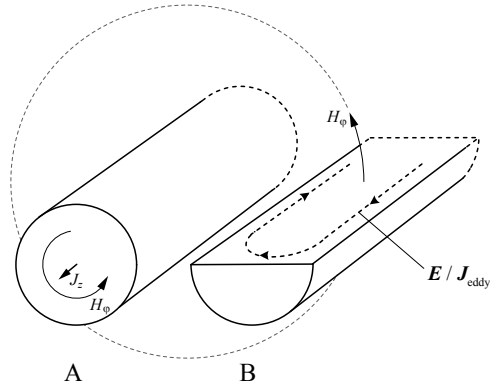


**Figure 4.4:** Induction of eddy currents due to Faraday's law.

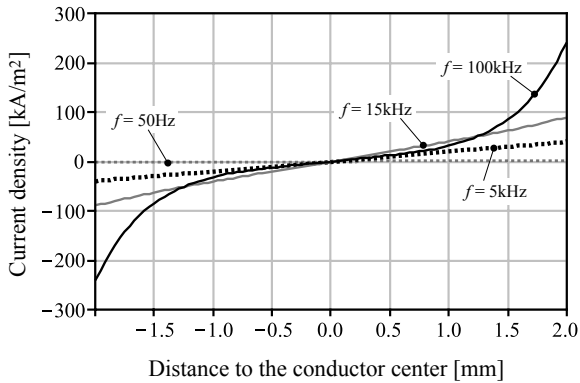


**Figure 4.5:** Induced current distributions of a conductor with a radius of 2 mm. The conductor is penetrated by an external alternating  $H$ -field of amplitude  $\hat{H}_e = 50\text{ A/m}$  and of different frequencies. Figure from [58].

The term "proximity-effect losses"  $P_P$  describes the losses due to eddy currents induced by an external magnetic field  $H_e$ .

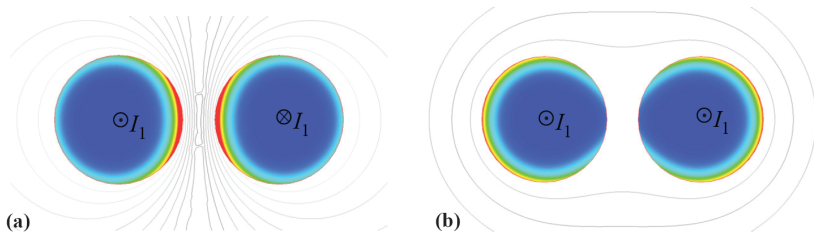


**Figure 4.6:** Current density of two neighboring conductors; The currents in the two conductors have in (a) opposite directions, and in (b) same directions.

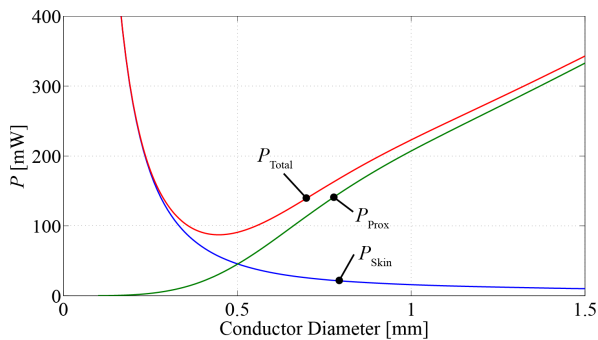


**Figure 4.7:** Skin- and proximity-effect losses per unit length of a round conductor.  $f = 100$  kHz,  $\hat{I} = 1$  A, and the magnitude of the external magnetic field  $\hat{H} = 1000$  A/m.

### 4.3 Round Conductor

Most windings are realized of solid round conductors since they are low priced. However, in return, they have high skin- and proximity-effect losses. In order to keep these losses low, the diameter must be selected well. The skin effect losses in solid round conductors decrease for increasing conductor diameters, while the proximity effect losses increase with increasing diameters; accordingly, there is an optimum conductor diameter to a given problem. This is illustrated in Figure 4.7.

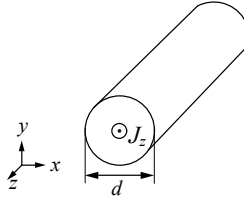


**Figure 4.8:** Cross section of the considered round conductor with a current density in  $z$ -direction. The conductor is infinitely long in  $z$ -direction.

In Section 4.3.1 and Section 4.3.2 the expressions to determine analytically skin- and proximity-effect losses are given. The external magnetic field strength  $H_e$  of every conductor has to be known in order to calculate the proximity-effect losses. In Section 4.3.3 a 1D calculation of the external field for un-gapped transformers is given. In the case of gapped cores, such 1D approximations are not applicable since the fringing field of the air gap cannot be described in a 1D manner. A 2D approach is introduced in Section 4.3.4. Winding losses can be reduced by using litz-wire windings, which are discussed in Section 4.3.5. In Section 4.3.6 calculations are compared to FEM simulations.

### 4.3.1 Skin Effect

The geometry considered to calculate the skin effect in round conductors is illustrated in Figure 4.8. The round conductor has the diameter  $d$ , and the length  $l$ , whereas it is assumed that  $d \ll l$ , thus the round conductor is considered as infinitely long in  $z$ -direction. The skin-effect losses (including DC losses) per unit length can be calculated as

$$P_S = R_{\text{DC}} \cdot F_R(f) \cdot \hat{I}^2 \quad (4.6)$$

with

$$\delta = \frac{1}{\sqrt{\pi \mu_0 \sigma f}},$$

$$\xi = \frac{d}{\sqrt{2} \delta},$$

$$R_{\text{DC}} = \frac{4}{\sigma \pi d^2},$$

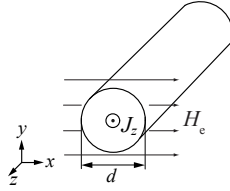


**Figure 4.9:** Cross section of a round conductor that is influenced by an external magnetic field in  $x$ -direction. The conductor is infinitely long in  $z$ -direction.

and<sup>1</sup>

$$F_R = \frac{\xi}{4\sqrt{2}} \left( \frac{\text{ber}_0(\xi)\text{bei}_1(\xi) - \text{ber}_0(\xi)\text{ber}_1(\xi)}{\text{ber}_1(\xi)^2 + \text{bei}_1(\xi)^2} - \frac{\text{bei}_0(\xi)\text{ber}_1(\xi) + \text{bei}_0(\xi)\text{bei}_1(\xi)}{\text{ber}_1(\xi)^2 + \text{bei}_1(\xi)^2} \right). \quad (4.7)$$

The derivation of (4.6) is from [58, 60] and is given in Appendix A.8.

### 4.3.2 Proximity Effect

A round conductor with diameter  $d$  that is positioned parallel to the  $z$ -axis, is penetrated by an alternating magnetic field with magnitude  $\hat{H}_e$ . The considered situation is illustrated in Figure 4.9. The resulting proximity-effect losses per unit length can be calculated as

$$P_P = R_{\text{DC}} \cdot G_R(f) \cdot \hat{H}_e^2 \quad (4.8)$$

with

$$\begin{aligned} \delta &= \frac{1}{\sqrt{\pi\mu_0\sigma f}}, \\ \xi &= \frac{d}{\sqrt{2}\delta}, \\ R_{\text{DC}} &= \frac{4}{\sigma\pi d^2}, \end{aligned}$$

<sup>1</sup>The solution is based on a *Bessel differential equation* that has the form  $x^2y'' + xy' + (k^2x^2 - v^2)y = 0$ . With the general solution  $y = C_1\mathbb{J}_v(kx) + C_2\mathbb{Y}_v(kx)$ , whereas  $\mathbb{J}_v(kx)$  is known as *Bessel function of the first kind* and order  $v$  and  $\mathbb{Y}_v(kx)$  is known as *Bessel function of the second kind* and order  $v$  [59]. Furthermore, to resolve  $\mathbb{J}_v(kx)$  into its real- and imaginary part, the *Kelvin functions* can be used:  $\mathbb{J}_v(j^{\frac{3}{2}}x) = \text{ber}_v x + j \text{bei}_v x$ .

and

$$G_R = -\frac{\xi\pi^2 d^2}{2\sqrt{2}} \left( \frac{\text{ber}_2(\xi)\text{ber}_1(\xi) + \text{ber}_2(\xi)\text{bei}_1(\xi)}{\text{ber}_0(\xi)^2 + \text{bei}_0(\xi)^2} + \frac{\text{bei}_2(\xi)\text{bei}_1(\xi) - \text{bei}_2(\xi)\text{ber}_1(\xi)}{\text{ber}_0(\xi)^2 + \text{bei}_0(\xi)^2} \right). \quad (4.9)$$

The derivation of (4.8) is from [58, 60] and is given in Appendix A.8.

### 4.3.3 Multi-Layer Windings Without Air Gap

With (4.6) and (4.8) the losses in a single solid round conductor can be calculated. For it, the current  $\hat{I}$  through the conductor and the external magnetic field  $\hat{H}_e$ , mostly present due to neighboring windings, has to be known. In this section it is shown how the winding losses of an un-gapped transformer with many round conductor turns are calculated. The applied method to calculate the external magnetic field has been derived in [61].

The case considered is illustrated in Figure 4.10(a). The conductors are assumed to be enclosed by an ideal magnetic conductor ( $\mu \rightarrow \infty$ ). The magnetic field is assumed to have only a direction as illustrated. The following considerations are made for only one winding shown in Figure 4.10 (i.e. winding 1); the solution for winding 2 is the same due to symmetry. The magnetic field strength  $H_z$  parallel to every conductor has to be known to calculate the proximity-effect losses. This magnetic field can be determined with Ampere's law. For instance, for the field calculation between the first and second layer, Ampere's law can be written as

$$\hat{H}_{z,1} b_F = N_L \hat{I}_1, \quad (4.10)$$

where  $N_L$  is the number of conductors per layer and  $b_F$  is the core window width (cf. Figure 4.10). Hence, the magnetic field between the first and second conductor is

$$\hat{H}_{z,1} = \frac{N_L \hat{I}}{b_F}, \quad (4.11)$$

between the second and third conductor

$$\hat{H}_{z,2} = \frac{2N_L \hat{I}}{b_F}, \quad (4.12)$$

etc.

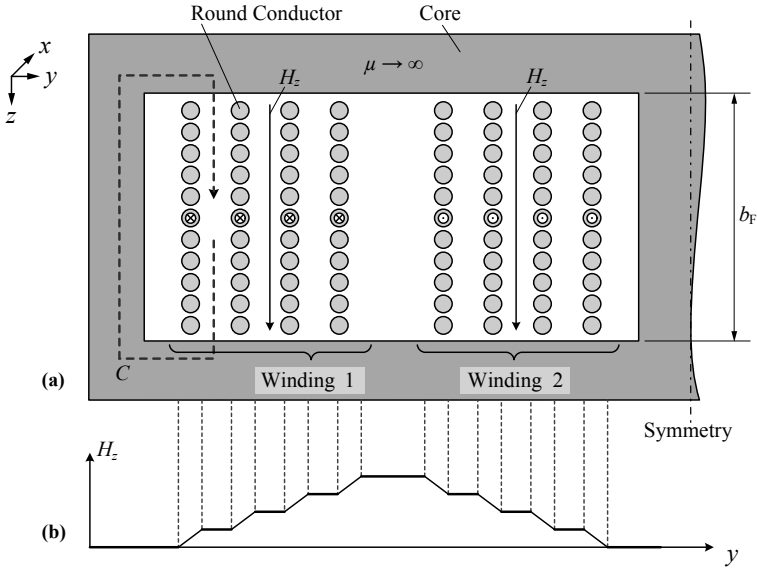


**Figure 4.10:** (a) Cross section of the left core-winding window of an E-core transformer that is built of solid round conductors. (b) Corresponding  $H$ -field distribution.

The distribution of the magnetic field is illustrated in Figure 4.10(b). The magnetic field is constant between two conductors, and ascending within a conductor. The same magnetic field strength has to be assumed on both sides of the conductor in order to use (4.8). The average value of the two magnetic fields of the two sides is taken ( $H_{\text{avg}} = \frac{1}{2}(H_{\text{left}} + H_{\text{right}})$ ).

Hence, for a setting as in Figure 4.10 with  $N_L M_L$  turns ( $M_L$ : the number layers), the average magnetic field for layer  $m$  is

$$\hat{H}_{\text{avg}} = \frac{2m - 1}{2} \frac{N_L \hat{I}}{b_F}, \quad (4.13)$$

with  $m = 1 \dots M_L$ .

The total losses for a winding with an average winding length  $l_m$

are then

$$\begin{aligned}
 P &= R_{\text{DC}} \left( F_{\text{R}} \hat{I}^2 N_{\text{L}} M_{\text{L}} + N_{\text{L}} G_{\text{R}} \sum_{m=1}^{M_{\text{L}}} \hat{H}_{\text{avg}}^2 \right) l_{\text{m}} \\
 &= R_{\text{DC}} \hat{I}^2 \left( N_{\text{L}} M_{\text{L}} F_{\text{R}} + N_{\text{L}}^3 M_{\text{L}} G_{\text{R}} \frac{4M_{\text{L}}^2 - 1}{12b_{\text{F}}^2} \right) l_{\text{m}}
 \end{aligned} \tag{4.14}$$

with

$$R_{\text{DC}} = \frac{4}{\sigma \pi d^2},$$

$N_{\text{L}}$  the number of conductors per layer, and  
 $M_{\text{L}}$  the number layers.

### 4.3.4 Multi-Layer Windings With Air Gap

The external magnetic field strength  $H_e$  of every conductor has to be known when calculating the proximity-effect losses. In the case of an un-gapped transformer core and windings that are fully-enclosed by core material, a 1D approximation to calculate the magnetic field exist, as shown in the preceding section. However, in the case of gapped cores, this 1D approximation is not applicable since the fringing field of the air gap cannot be described in a 1D manner. An approach has to be selected to overcome this limitation. The approach selected for this thesis can be used for inductive components with and without air gaps and is based on the work presented in [5, 62]. The approach is presented in the following.

A winding arrangement as illustrated in Figure 4.11(a) leads to an external field vector  $\hat{\mathbf{H}}$  across conductor  $q_{x_i, y_k}$  due to the current  $\hat{i}_{x_u, y_l}$  of conductor  $q_{x_u, y_l}$  of

$$\begin{aligned}
 \hat{\mathbf{H}} &= -\text{j} \frac{\hat{i}_{x_u, y_l}}{2\pi \sqrt{(x_u - x_i)^2 + (y_l - y_k)^2}} \\
 &\cdot \frac{(x_u - x_i) + \text{j}(y_l - y_k)}{\sqrt{(x_u - x_i)^2 + (y_l - y_k)^2}} \\
 &= \frac{\hat{i}_{x_u, y_l} ((y_l - y_k) - \text{j}(x_u - x_i))}{2\pi ((x_u - x_i)^2 + (y_l - y_k)^2)}.
 \end{aligned} \tag{4.15}$$

Complex numbers are used to identify the conductor position as this simplifies the calculation. The magnitude of the total external field  $\hat{H}_e$

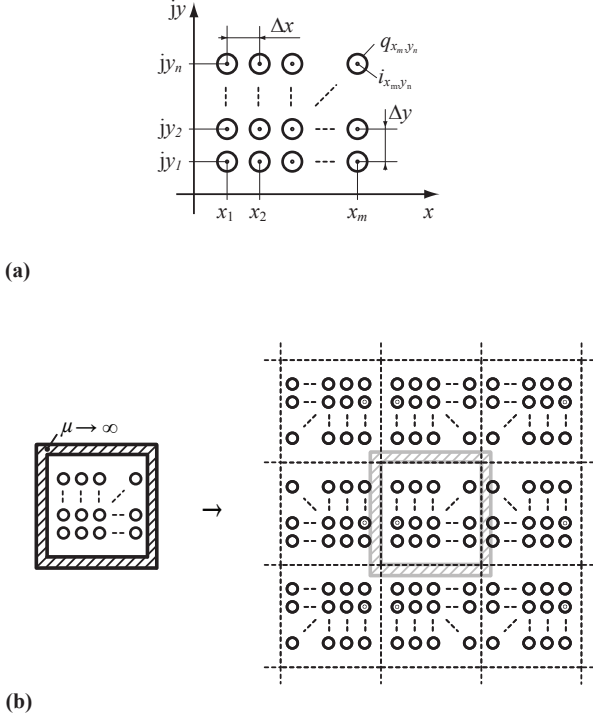


**Figure 4.11:** (a) Illustration of winding arrangement. (b) Illustration of mirroring.

across conductor  $q_{x_i, y_k}$  can be calculated with

$$\hat{H}_e = \left| \sum_{u=1}^m \sum_{l=1}^n \epsilon(u, l) \frac{\hat{i}_{x_u, y_l} ((y_l - y_k) - j(x_u - x_i))}{2\pi ((x_u - x_i)^2 + (y_l - y_k)^2)} \right|, \quad (4.16)$$

where  $\epsilon(u, l) = 0$  for  $u = i$  and  $l = k$ , and  $\epsilon(u, l) = 1$  for  $u \neq i$  or  $l \neq k$ . The proximity-effect losses can be calculated based on (4.8) with the determined external magnetic field  $\hat{H}_e$ .

The impact of a magnetic conducting material can be modeled with the *method of images* (also known as *mirroring*). There, the shape of the magnetic field can be modeled by removing the magnetic material and injecting currents in a way such that the magnetic field remains

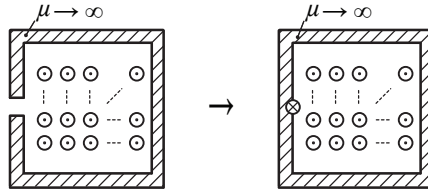


**Figure 4.12:** Illustration of modeling an air gap as a fictitious conductor.

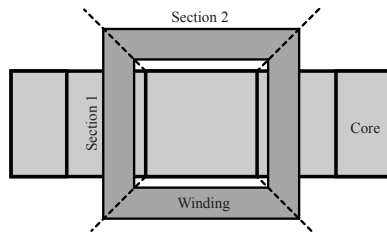


**Figure 4.13:** Illustration of different sections in the winding path of an E-core.

unchanged. The additional currents are the mirrored version of the original currents, as illustrated in Figure 4.11(b). In case of windings that are fully-enclosed by magnetic material (i.e. in the core window), a new wall is created at each mirroring step as the walls have to be mirrored as well. The mirroring can be continued to push the walls away. This is illustrated in Figure 4.11(b).

The presence of an air gap can be modeled as a fictitious conductor without eddy currents equal to the magneto-motive force (MMF) across the air gap [5] as illustrated in Figure 4.12.

In the case of an E-core, for instance, the winding losses have to be calculated differently for each section illustrated in Figure 4.13 as the mirroring leads to different results.

In the case of a non-sinusoidal current it is permissible to express the current as a Fourier series, calculate the losses for each frequency component independently, and then total them up. It is also permissible to total up the independently calculated skin effect and proximity-effect losses [63]. Both are shown in Appendix A.9.

It is possible to accurately model winding losses of solid conduc-

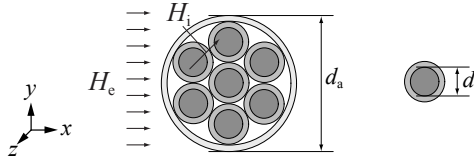


**Figure 4.14:** Cross-sectional area of litz-wire winding.

tors based on the above discussion. In Section 4.3.6 a discussion about the expected accuracy and comparisons with FEM simulations are presented. Based on the above derivations, a litz wire calculation is also possible, which will be shown in the following Section 4.3.5.

### 4.3.5 Litz-Wire Windings

Winding losses can be reduced by using litz-wire windings. Litz-wire windings are made up of multiple individually-insulated strands as illustrated in Figure 4.14. In litz-wire windings, skin- and proximity effects can be further divided into strand-level and bundle-level effects [64]. The effect related to eddy currents circulating in paths involving multiple strands is called the bundle-level effect, whereas strand-level effects take place within individual strands. The strands are twisted such that, ideally, each strand equally occupies each position in the bundle. Therewith, bundle-level effects can be strongly reduced and are neglected in the following formulae. However, bundle-level effects may have an impact on winding losses in case the litz wire is not ideally twisted, as have been reported in [65].

The skin-effect losses, including DC losses, of a litz-wire winding that consists of  $n$  strands, each with strand diameter  $d_i$  are calculated as [58, 62]

$$P_{S,L} = n \cdot R_{DC} \cdot F_R(f) \cdot \left( \frac{\hat{I}}{n} \right)^2, \quad (4.17)$$

where  $R_{DC} = \frac{4}{\sigma \pi d_i^2}$ , and  $F_R(f)$  is calculated as (4.7) with the strand diameter  $d = d_i$ .

The magnetic field that leads to proximity-effect losses is the sum of the external magnetic field  $H_e$  and the internal magnetic field  $H_i$ . The external magnetic field  $H_e$  originates from the neighboring conductors

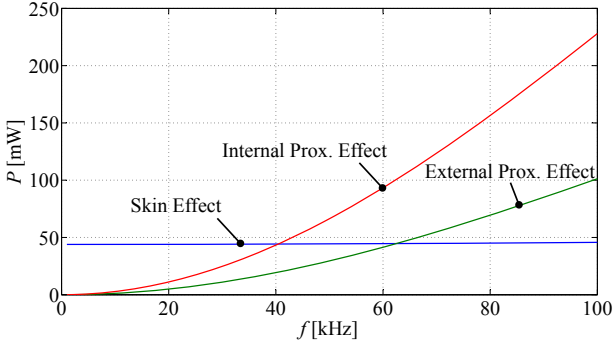


**Figure 4.15:** Skin, internal prox. and external prox. effect losses per unit length in a litz wire as a function of the frequency  $f$ . With  $25 \times (d_i = 0.5 \text{ mm})$ ,  $\hat{I} = 5 \text{ A}$ , and the magnitude of the external magnetic field  $\hat{H} = 300 \text{ A/m}$ .

or the air gap fringing field and can be calculated in the same manner as described for the case of solid round conductors. The internal magnetic field  $H_i$  across one strand originates from its neighboring strands. It is assumed that the current is equally distributed over the litz-wire cross-sectional area for the calculation of the internal magnetic field. Each strand is, furthermore, assumed to be penetrated by the average internal magnetic field.

The proximity-effect losses in litz-wire windings can then be calculated as [58, 62]

$$\begin{aligned}
 P_{P,L} &= P_{P,L,e} + P_{P,L,i} \\
 &= n \cdot R_{DC} \cdot G_R(f) \left( \hat{H}_e^2 + \frac{\hat{I}^2}{2\pi^2 d_a^2} \right) \quad (4.18)
 \end{aligned}$$

where  $R_{DC} = \frac{4}{\sigma \pi d_i^2}$ , and  $G_R(f)$  is calculated as (4.9) with the strand diameter  $d = d_i$ . The losses  $P_{P,L,e}$  are named the external proximity-effect losses, since they originate from the external magnetic field. The losses  $P_{P,L,i}$  are named the internal proximity-effect losses, since they originate from the internal magnetic field (the field from the neighboring strands). In Figure 4.15 the skin-, internal proximity- and external proximity-effect losses of a litz wire are plotted as a function of the frequency  $f$ .

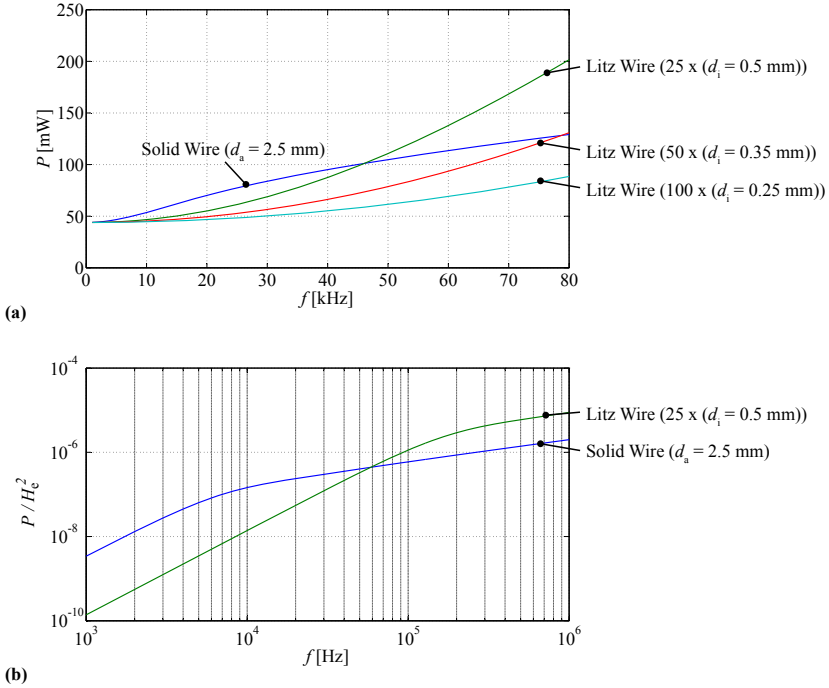


**Figure 4.16:** Losses (per unit length) of litz wires and a solid round wire with all the same cross-sectional area, as a function of the frequency  $f$ ; the current per wire is  $\hat{I} = 5$  A. (a) Skin and internal proximity effects (no external magnetic field); (b) external proximity effect.

An important question is whether litz wires are always better than solid round conductors. In Figure 4.16 losses of litz wires and a solid round wire are compared to each other. All wires have the same cross-sectional area. As can be seen in Figure 4.16(a), above a certain frequency the litz wire losses exceed the solid wire losses; the reason is that the internal proximity-effect losses become dominant and deteriorate the performance of litz wires. But, not only because of the internal proximity-effect losses, but also because of the external proximity-effect losses, litz wire become worse above a certain frequency. This can be seen in Figure 4.16(b), where the external proximity-effect losses of a

litz wire above some frequency exceed the (external) proximity-effect losses of a solid round conductor. Generally, it can be said that the higher the number of strands the better the litz wire (in case the copper cross-sectional area is kept constant). A high number of strands is favorable in case the copper cross-sectional area is kept constant; however, a higher number of strands brings the disadvantage that the space occupied by insulation is high. In [64] this issue is addressed and it is shown how to optimally select the number and diameter of strands.

### 4.3.6 Accuracy Analysis

The formulae above are based on analytical equations. The major simplification that has been made is to neglect the magnetic field of the induced eddy currents. The calculated field  $H_e$  is assumed to penetrate completely thorough the conductors. According to [5] this approximation is valid if the largest dimension of the conductor, i.e. the diameter for a round conductor/strand, is less than 1.6 times the skin depth  $\delta$ . Consequently, the frequency  $f_{\max}$ , up to which the calculation for a given conductor diameter  $d$  is accurate, can be calculated as

$$f_{\max} = \frac{2.56}{\pi \mu_0 \sigma d^2}. \quad (4.19)$$

Another simplification that has been made is that it was neglected that the external field might be bent within the conductor, i.e. the field might not be homogeneous inside the conductor. However, for the considered cases, the approach at hand showed to have a high accuracy. Solutions to overcome the two mentioned problems, i.e. high frequency effects or bent flux lines, can be found in literature, e.g. in [5].

Three winding arrangements have been calculated and compared to 2D FEM simulations. The FEM simulations have been carried out with the software FEMM<sup>2</sup>. The results are given in Figure 4.17. Simulations for frequencies below  $f_{\max}$  lead to deviations of always less than 5%, above  $f_{\max}$  more than 5%, but, in all illustrated cases, never more than 25%.

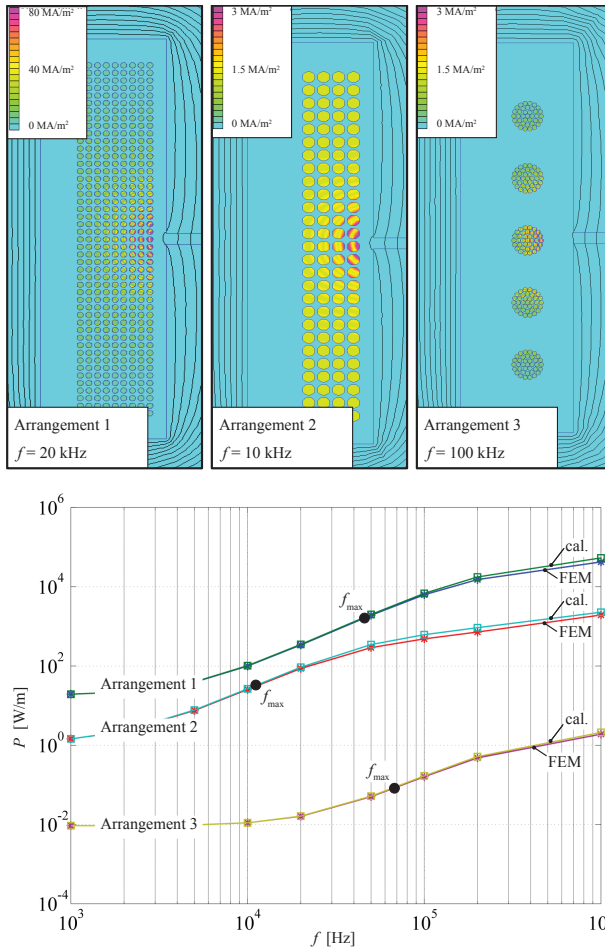


**Figure 4.17:** Comparison of winding loss calculation to FEM simulation. Size of core window: 37 mm x 10.15 mm. Air gap length 1 mm. Winding arrangement 1: number of turns  $N = 423$ ;  $\hat{I} = 1$  A; winding diameter  $d = 0.5$  mm. Winding arrangement 2: number of turns  $N = 108$ ;  $\hat{I} = 1$  A; winding diameter  $d = 1$  mm. Winding arrangement 3: number of turns  $N = 5$ ; number of strands  $n = 37$ ;  $\hat{I} = 1$  A; strand diameter  $d_i = 0.4$  mm.

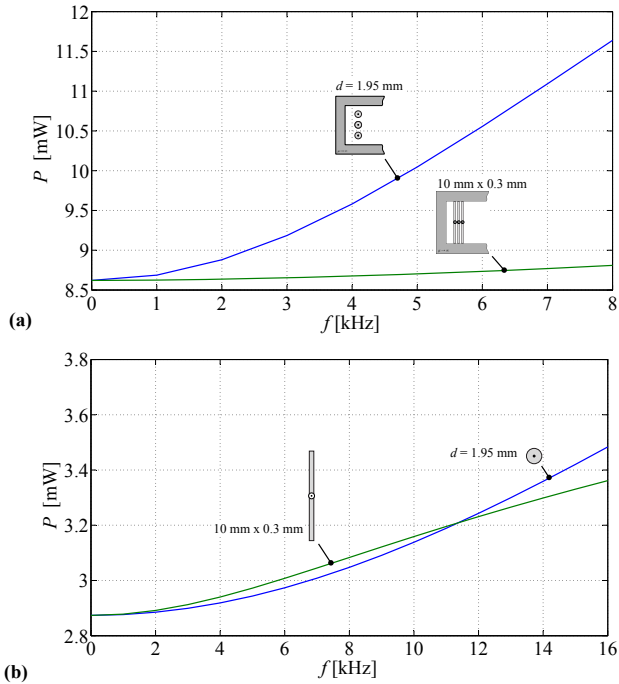


**Figure 4.18:** Comparison between the losses of solid round and foil conductors. Size of foil conductors: 10 mm x 0.3 mm; diameter of round conductor  $d = 1.95$  mm; current per conductor  $\hat{I} = 1$  A. All losses per unit length. (a) Windings enclosed by magnetic material; (b) single conductors not enclosed by magnetic material.

## 4.4 Foil Conductor

Foil windings are another winding type that allow reducing high frequency losses. Furthermore, they show advantages compared to litz wires such as a higher filling factor or lower price. However, they have drawbacks such as increased winding capacitances and the risk of an orthogonal flux. A flux orthogonal to the foil conductor leads to high eddy current losses.

In Figure 4.18(a) foil and solid round windings are compared to

<sup>2</sup>FEMM 4.2, freeware from [www.femm.info](http://www.femm.info) (date of download: February 2011).

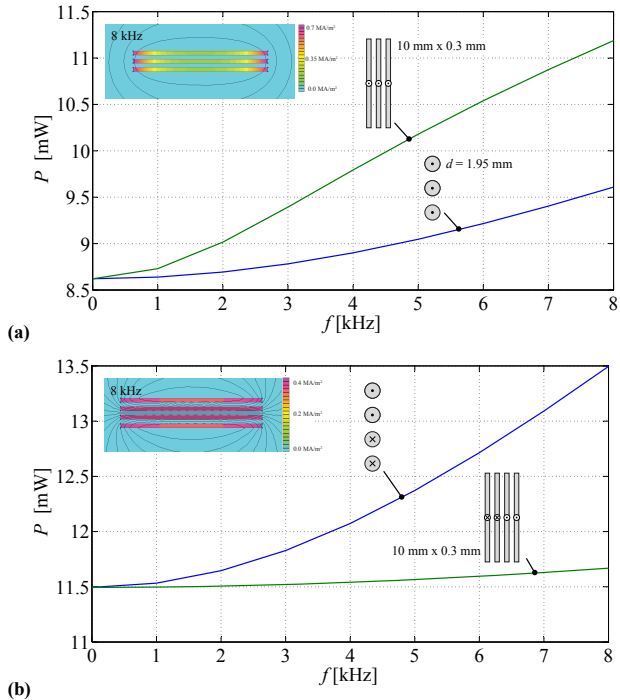


**Figure 4.19:** Comparison between the losses of solid round and foil conductors. Size of foil conductors: 10 mm x 0.3 mm; diameter of round conductor  $d = 1.95$  mm; current per conductor  $\hat{I} = 1$  A. All losses per unit length. (a) Three windings not enclosed by magnetic material, all conductors with current in one direction. (b) Windings with return conductors not enclosed by magnetic material.

each other. As can be seen the foil winding has substantially lower losses compared to a solid round winding. The reason is that the "skin" of a foil conductor with the same cross-sectional area is larger compared to the "skin" of a solid round conductor, hence the skin-effect losses are substantially reduced. In Figure 4.18(a) the foil winding is enclosed by magnetic material which guarantees that the magnetic field is always parallel to the conductor, i.e. no orthogonal flux is present. In Figure 4.18(b) and Figure 4.19(a) the situation is different. The foil winding is not enclosed by a magnetic material, i.e. the parallel field

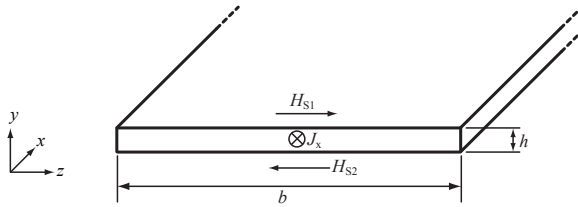


**Figure 4.20:** Cross section of a foil conductor with a current density in  $x$ -direction. The conductor is infinitely long in  $x$ -direction.

lines are not guaranteed. In this situation, the current density is not constant along the width, i.e. the current is concentrated at the ends of the windings. This increases the winding losses in the foil windings substantially. The losses can be higher than in solid round conductors. The current is concentrated on the ends of the winding, since there is a flux orthogonal to the foil conductors, as can be seen in Figure 4.19(a). In the situation where return conductors are placed anti-parallel to the main conductors, as illustrated in Figure 4.19(b), the field is parallelized and the losses in foil conductors are reduced. It can be concluded that HF losses can be substantially reduced by the use of foil windings. However, a careful design, in which orthogonal flux is avoided, is crucial.

In Section 4.4.1 and Section 4.4.2 the analytical expressions for skin and proximity-effect losses in foil windings are given. The external magnetic field strength  $H_e$  of every conductor has to be known when calculating the proximity-effect losses. In Section 4.4.3 a 1D derivation of the external field for un-gapped transformers is given. However, in the case of gapped inductors, such 1D approximations are not applicable as the fringing field of the air gap cannot be described in a 1D manner. In Section 4.4.5 an approach how to calculate losses in gapped inductors is given. In Section 4.4.6 calculations are compared to FEM simulations.

#### 4.4.1 Skin Effect

The geometry considered to calculate the skin-effect losses in foil windings is illustrated in Figure 4.20. The conductor has a width  $b$  and a height  $h$ , whereas  $h \ll b$ . It is assumed that the current is flowing in  $x$ -direction, with frequency  $f$  and magnitude  $\hat{I}$ . The skin-effect losses (including DC losses) per unit length of this geometry can be calculated

as

$$P_S = F_F(f) \cdot R_{DC} \cdot \hat{I}^2 \quad (4.20)$$

with

$$\delta = \frac{1}{\sqrt{\pi\mu_0\sigma f}},$$

$$\nu = \frac{h}{\delta},$$

$$R_{DC} = \frac{1}{\sigma b h},$$

and

$$F_F = \frac{\nu \sinh \nu + \sin \nu}{4 \cosh \nu - \cos \nu}.$$

The derivation of (4.20) is from [58, 60] and is given in Appendix A.7.

#### 4.4.2 Proximity Effect

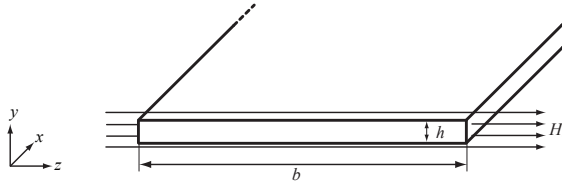


**Figure 4.21:** Cross section of a foil conductor that is influenced by an external magnetic field in  $z$ -direction. The conductor is infinitely long in  $x$ -direction.

The geometry considered to calculate the proximity-effect losses in foil windings is illustrated in Figure 4.21. On both conductor sides the magnetic field strength in  $z$ -direction has the magnitude  $\hat{H}_e$ . The proximity-effect losses per unit length of this geometry can be calculated as

$$P_P = R_{DC} \cdot G_F(f) \cdot \hat{H}_e^2 \quad (4.21)$$

with

$$\delta = \frac{1}{\sqrt{\pi\mu_0\sigma f}},$$

$$\nu = \frac{h}{\delta},$$

$$R_{\text{DC}} = \frac{1}{\sigma b h},$$

and

$$G_{\text{F}} = b^2 \nu \frac{\sinh \nu - \sin \nu}{\cosh \nu + \cos \nu}.$$

The derivation of (4.21) is from [58, 60] and is given in Appendix A.7.

### 4.4.3 Foil Multi-Layer Without Air Gap

With (4.20) and (4.21) the losses in a single foil conductor can be calculated. For it, the current  $\hat{I}$  through the conductor and the external magnetic field  $\hat{H}_e$ , mostly present due to neighboring windings, has to be known.

In the following, the winding losses of an un-gapped transformer with many foil conductor turns are calculated. The case considered is illustrated in Figure 4.22(a). The conductors are assumed to be enclosed by a magnetic ideal conductor ( $\mu \rightarrow \infty$ ). The magnetic field between two layers is then calculated with Ampere's law similar as in the approach for round conductors (cf. Section 4.3.3). For instance, the magnetic field between the first and second conductor is

$$\hat{H}_{z,1} = \frac{\hat{I}}{b_{\text{F}}}. \quad (4.22)$$

The distribution of the magnetic field is illustrated in Figure 4.22(b). The average value of the two magnetic fields of the two sides is taken to calculate the proximity-effect losses for each conductor.

Hence, the losses in winding 1 of an un-gapped transformer with foil windings with average winding length  $l_{\text{m}}$  (cf. Figure 4.22) is

$$P = R_{\text{DC}} (F_{\text{F}} \hat{I}^2 N + G_{\text{F}} \sum_{m=1}^N \hat{H}_{\text{avg}}^2) l_{\text{m}} \quad (4.23)$$

$$= R_{\text{DC}} \hat{I}^2 \left( F_{\text{F}} + G_{\text{F}} \frac{4N^2 - 1}{12b_{\text{F}}^2} \right) N l_{\text{m}} \quad (4.24)$$

with

$$R_{\text{DC}} = \frac{1}{\sigma b h},$$

and  $N$  the number of turns per winding.

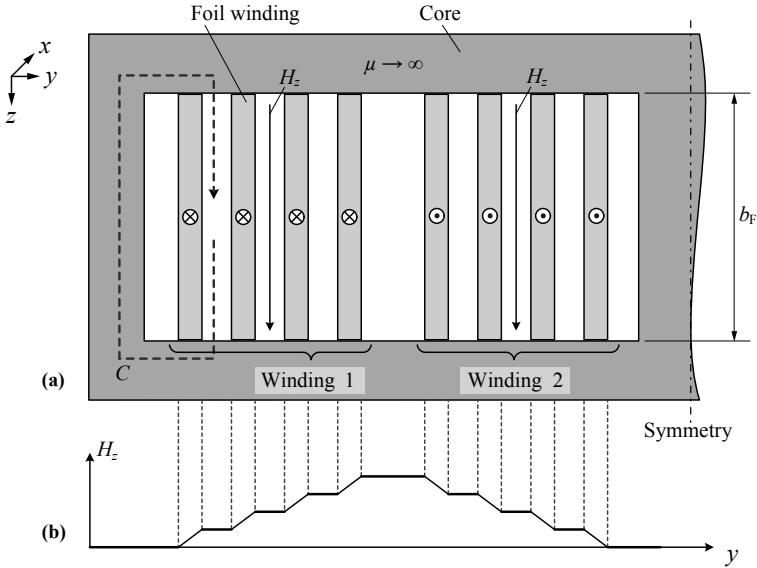


**Figure 4.22:** (a) Cross section of the left core-winding window of an E-core transformer that is built of foil conductors. (b) Corresponding  $H$ -field distribution. Figure from [58].

#### 4.4.4 Short Foil Conductors

The width  $b_L$  of foil conductors are in practical implementations smaller than the width of the core window  $b_F$ . There are also situations in which more than one foil conductor per layer is present. Short foil conductors can be transformed into an equivalent foil conductor with width  $b'_L = b_F$  in order to be able to use the equations derived in the previous section. The transformation is illustrated in Figure 4.23. Dowell introduced this transformation in [61] such that the DC resistances of the original and the transformed foils are the same. For it, Dowell introduced the "porosity factor"  $\eta$ , which is calculated as

$$\eta = \frac{N_L b_L}{b_F}, \quad (4.25)$$

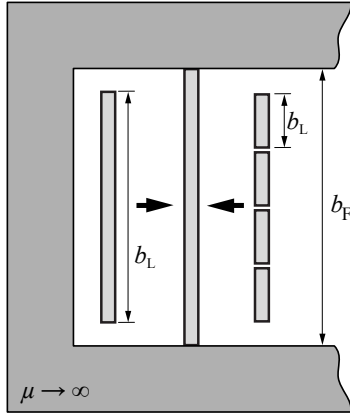


**Figure 4.23:** Transformation of short foil conductors into foils of window size height.

with  $N_L$  the number of foil conductors per layer. The conductivity  $\sigma$ , skin depth  $\delta$ , and variable  $\nu$  are accordingly redefined as

$$\sigma' = \eta\sigma, \quad (4.26)$$

$$\delta' = \frac{1}{\sqrt{\pi f \sigma' \mu_0}}, \quad (4.27)$$

and

$$\nu' = \frac{h}{\delta'}. \quad (4.28)$$

Equations (4.26), (4.27), and (4.28), together with the adapted width  $b'_L = b_F$ , can directly be used in the equations for the skin- and proximity-effect losses, (4.20) and (4.21). In case more than one foil conductor per layer is present, (4.24) has to be (slightly) adapted in order to consider that the field is now generated by the current  $N_L \hat{I}$  per layer (and not only  $\hat{I}$ ).

#### 4.4.5 Foil Multi-Layer With Air Gap

In case of gapped inductors with a foil winding, it is not appropriate to use the equations of the previous sections since the air gap leads to a field orthogonal to the foils of the winding. This field has to be taken into consideration when modeling winding losses. References

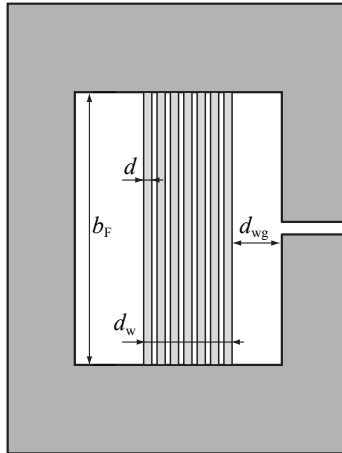


**Figure 4.24:** Illustration of situation considered for winding loss modeling of gapped foil winding inductors.

[5, 66] give approaches how to calculate losses in gapped inductors. The approach in [66] is based on a superposition of the losses from the 1-D field calculation of the previous sections and losses due to eddy currents caused by the air gap fringing field calculated with a 2-D field calculation. The derivation of approach [66] leads to relatively complex, difficult to handle formulae. The approach derived in [5] is much easier and straight forward to implement, therefore, this approach has been selected to be briefly discussed in the following.

The situation considered for the winding loss modeling of gapped foil winding inductors is illustrated in Figure 4.24. It is assumed that the tip of the foil winding is very close to the magnetic material, the air gap is very small compared to the distance between air gap and first foil conductor  $d_{wg}$ , and the skin depth  $\delta$  is considerably larger than the foil thickness.

The winding loss per unit length for a foil winding structure as

illustrated in Figure 4.24 with a single air gap becomes

$$P = \frac{\rho' \left( N \frac{\hat{I}}{\sqrt{2}} \right)^2}{\delta'} \left( \int_{-b_F/2}^{b_F/2} \left[ \sum_{k=-\infty}^{\infty} \frac{1}{2d_{wg} \cosh \left( \frac{(x+kb_F)\pi}{2d_{wg}} \right)} \right]^2 dx - \frac{1}{b_F} \right) \quad (4.29)$$

with

$$\rho' = \rho \frac{Nd}{d_w},$$

$$\delta' = \delta \sqrt{\frac{d_w}{Nd}},$$

where  $\rho$  is the resistivity of the foil material and  $\delta = 1/\sqrt{\pi\mu_0\sigma f}$  is the skin depth.

For cases where  $d_{wg}/b_F < 0.25$ , (4.29) can further be simplified to

$$P = \frac{\rho' \left( N \frac{\hat{I}}{\sqrt{2}} \right)^2}{\delta' \pi d_{wg}} \left( 1 - \pi \frac{d_{wg}}{b_F} \right). \quad (4.30)$$

#### 4.4.6 Accuracy Analysis

Four winding arrangements have been calculated and compared to 2D FEM simulations. The FEM simulations have been carried out with the software FEMM<sup>3</sup>. The results are given in Figure 4.25. The winding arrangements 1 and 2 are in transformer configuration, i.e. with a primary and a secondary winding. The winding arrangements 1 and 2 are calculated based on the discussion given in Section 4.4.3 and Section 4.4.4. The winding arrangements 3 and 4 are in gapped inductor configuration, i.e. with only a primary winding. The winding arrangements 3 and 4 are calculated based on the discussion given in Section 4.4.5.

It can be seen in Figure 4.25, that the calculation of winding arrangement 1 is very accurate, with a deviation of always less than 3.1%. The winding arrangement 1 has windings with the same width as the core window, i.e.  $b_L = b_F$ . For the winding arrangement 2 the winding width is smaller than the core window width, i.e.  $b_L = 33 \text{ mm} < b_F = 37 \text{ mm}$ , hence, the windings have to be transformed as discussed in Section 4.4.4. The accuracy is still good, with a deviation of always less than 6.5%.

<sup>3</sup>FEMM 4.2, freeware from [www.femm.info](http://www.femm.info) (date of download: February 2011).

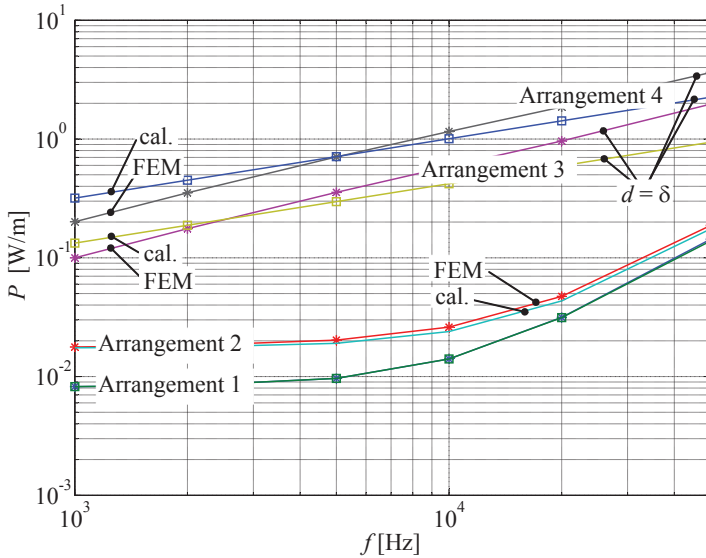


**Figure 4.25:** Comparison of winding loss calculation to FEM simulation. Size of core window: 37 mm x 10.15 mm ( $b_F = 37$  mm).

**Winding arrangement 1:** number of turns  $N = 2 \times 7$ ;  $\hat{I} = 1$  A; foil thickness  $h = 0.4$  mm; winding width  $b_L = 37$  mm; distance between foils 0.2 mm; distance between core leg and first winding  $d_{wg} = 1.0$  mm; no air gap; transformer configuration.

**Winding arrangement 2:** number of turns  $N = 2 \times 10$ ;  $\hat{I} = 1$  A; foil thickness  $h = 0.3$  mm; winding width  $b_L = 33$  mm; distance between foils 0.1 mm; distance between core leg and first winding  $d_{wg} = 1.0$  mm; no air gap; transformer configuration.

**Winding arrangement 3:** number of turns  $N = 14$ ;  $\hat{I} = 1$  A; foil thickness  $h = 0.4$  mm; winding width  $b_L = 37$  mm; distance between foils 0.2 mm; distance between core leg and first winding  $d_{wg} = 1.0$  mm; air gap length 0.5 mm; inductor configuration.

**Winding arrangement 4:** number of turns  $N = 20$ ;  $\hat{I} = 1$  A; foil thickness  $h = 0.3$  mm; winding width  $b_L = 37$  mm; distance between foils 0.1 mm; distance between core leg and first winding  $d_{wg} = 1.0$  mm; air gap length 0.5 mm; inductor configuration.

The winding arrangements 3 and 4 have been calculated with (4.30). The winding arrangements 3 and 4 have windings with the same width

as the core window, i.e.  $b_L = b_F$ . The deviation between (4.29) and (4.30) has been determined to be very small, hence, the losses have been calculated with (4.30). However, the accuracy is not very high. In both arrangements, the highest accuracy has been achieved in a range where the winding thickness  $d$  is smaller than the skin depth  $\delta$ , as can be seen in Figure 4.25 where the points of  $d = \delta$  are labeled. However, for very high and for very low frequencies the accuracy is worse. In conclusion, the approach introduced in Section 4.4.5 gives, in a limited range, a reasonable good estimation of the losses. Nevertheless, before building the inductor, a confirmation with a FEM simulation is indispensable.



# Chapter 5

## Thermal Modeling

In the last two chapters, the losses occurring in magnetic components have been discussed. Another important aspect in the design phase of inductive components is the expected temperature of the component. This is not only important to avoid overheating, it has also importance to correctly model losses, since the losses are influenced by the temperature. Hence, a thermal model is indispensable for an accurate loss model. This chapter illustrates ways to model the thermal behavior of the components. The thermal modeling is based on a simplified two dimensional resistor network. Each resistor is determined based on calculations of heat conduction, radiation, and natural convection. In this thesis, only natural convection and no forced convection is considered. In Section 5.1 a brief overview about thermal modeling is presented, and in Section 5.2 the heat transfer mechanisms are summarized and the formulae needed for modeling are given.

### 5.1 Overview of Thermal Models

Basically, the three physical mechanisms conduction, radiation, and convection lead to transported heat. These three mechanisms have to be considered when modeling the thermal behavior of a given geometry. Generally, in order to avoid a computationally intensive finite element simulation, a common approach is to calculate the thermal behavior via thermal resistor networks. In the following the concept of thermal resistor networks is discussed.

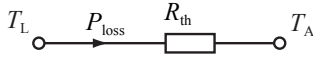


**Figure 5.1:** Thermal model with only one thermal resistance.

### 5.1.1 Total Thermal Resistance

The temperature of a magnetic component is often considered as homogeneous and the thermal behavior is characterized by a single resistance  $R_{\text{th}}$ . Such a model is illustrated in Fig. 5.1. The resistor is formally determined according to the thermal-electric analogy and the ohmic law with

$$R_{\text{th}} = \frac{\Delta T}{\sum P}, \quad (5.1)$$

where  $\Delta T$  is the difference between the ambient and magnetic component temperature and  $\sum P$  is the sum of the occurring losses inside the magnetic component. Major drawback of this approach is that a linear function as (5.1) is not valid, i.e.  $R_{\text{th}}$  changes with changing (absolute) temperature. However, when one defines  $R_{\text{th}}$  as a function of the ambient and magnetic component temperatures, the approach improves substantially. The resistor is then determined based on calculations of heat conduction, radiation, and convection.

### 5.1.2 Thermal Resistor Networks

The above introduced model can be improved by taking into consideration that the temperature is unequally distributed inside the magnetic component. For this, the resolution of nodes of constant temperature can be chosen arbitrarily. Models of different complexity have been derived in the past. For example, in [10] for each winding turn a new temperature node is introduced, that leads to a quite complex resistor network. Simpler approaches have been implemented e.g. in [7] or [22], where one node of constant temperature represents the core temperature, and one node of constant temperature represents the winding temperature. This simplification is motivated by the fact that the core and winding materials are usually good heat conductors. The according resistor networks for inductors and transformers are illustrated in Figure 5.2. Generally, the goal of any modeling task is to evaluate a model that is as simple as possible, but still guarantees a reasonably high accuracy.

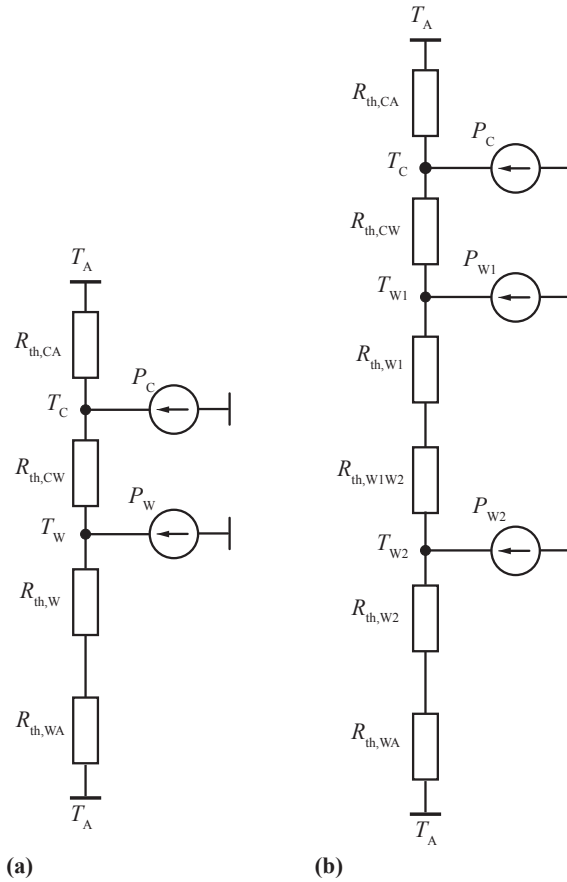


**Figure 5.2:** Thermal model of (a) inductor and (b) transformer (with two windings).

In a model such as illustrated in Figure 5.2, it is recommended to add a resistor for the heat conduction from the inside to the outside of the winding. This is favorable, as otherwise only the winding surface temperature would be calculated, which is lower compared to the inner temperature. This resistor is important to model the temperature drop within the winding. By doing this, the winding losses are assumed to occur all on the inner winding side, which leads to a presumed higher

temperature. However, the simplification is justified by the reduced complexity that is achieved with it.

For the sake of completeness, it is mentioned that only the steady state temperature is calculated. The dynamics of the temperature is not modeled. This could be done by adding capacitors representing the heat capacity.

The major difficulty is to calculate the values of the network resistances correctly. This is done based on calculations of heat radiation, conduction and convection, and will be introduced in the following.

## 5.2 Heat Transfer Mechanisms

Heat is energy transferred from one body to another due to thermal contact. Energy can only be transferred by heat between bodies of different temperatures, where the sink has to be cooler. The physical mechanisms of heat transfer that occur in magnetic components are conduction and radiation. The term "convection" is used to describe the combined effect of conduction and fluid flow, which for this work is considered as an additional heat transfer mechanism. Each network resistance is determined based on calculations of heat conduction, convection, and radiation. In the following, the three heat transfer mechanisms are explained one by one. Formulae that allow to determine the resistor network are given.

### 5.2.1 Thermal Conduction

Thermal conduction (or heat conduction) is the transfer of heat between neighboring molecules in a substance due to a temperature gradient

$$\vec{q} = -\lambda \cdot \nabla T, \quad (5.2)$$

where  $\vec{q}$  is the heat flux,  $\lambda$  is the heat conductivity, and  $\nabla T$  the temperature gradient. The heat conductivity  $\lambda$  is a material parameter and can be considered as constant for most materials employed in magnetic components. Material parameters can e.g. be extracted from [67].

The thermal resistance for a cuboid as illustrated in Figure 5.3 with length  $l$  and cross section  $A$  is calculated with

$$R_{\text{th}} = \frac{\Delta T}{P} = \frac{l}{A\lambda}. \quad (5.3)$$

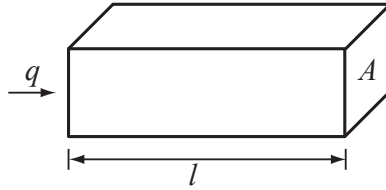


**Figure 5.3:** Thermal resistance of a cuboid:  $R_{\text{th}} = l/(A\lambda)$ .

Although (5.3) looks rather simple, the calculation of heat conduction can be challenging. For instance, one difficulty is to model interfaces between materials.

## 5.2.2 Thermal Natural Convection

The term convection is used to describe the combined effect of conduction and fluid flow. When a body is facing a fluid, the fluid absorbs and transports heat. Convection can be calculated by solving the differential Navier Stokes equations analytically or numerically. However, empirical approaches that overcome solving this complex mathematical problem exist. They are widely applicable for different geometries. Basically, the heat transfer via convection is described with

$$P = \alpha A(T_b - T_g), \quad (5.4)$$

where  $P$  is the heat flow,  $A$  the surface area,  $T_b$  the body surface temperature, and  $T_g$  the fluid temperature.  $\alpha$  is a coefficient that is influenced by [10]

- ▶ the absolute temperature,
- ▶ the material property of the fluid,
- ▶ the flow rate of the fluid,
- ▶ the dimensions of the considered surface,
- ▶ orientation of the considered surface,
- ▶ and the surface texture.

A set of characteristic dimensionless numbers has been introduced to determine  $\alpha$ ; they are summarized in Table 5.1. In the following, this characteristic numbers are described one by one.

| Name            | Symbol | Measure of ...   |
|-----------------|--------|--|
| Nusselt number  | $Nu$   | ...improvement of heat transfer compared to the case with hypothetical static fluid. |
| Grashof number  | $Gr$   | ...ratio between buoyancy and frictional force of fluid.                             |
| Prandtl number  | $Pr$   | ...ratio between viscosity and heat conductivity of fluid.                           |
| Rayleigh number | $Ra$   | ...flow condition (laminar or turbulent) of fluid.                                   |

**Table 5.1:** Characteristic numbers to describe convection empirically [10].

### Characteristic Dimensionless Numbers

- The *Nusselt* number is a measure of improvement of heat transfer compared to the case with hypothetical static fluid. The fluid next to a hot surface heats up and transports heat constantly away, hence the heat transfer capability is improved. The Nusselt number is calculated with

$$Nu = \frac{\alpha l}{\lambda}, \quad (5.5)$$

where  $\lambda$  is the heat conductivity of the fluid,  $\alpha$  is the coefficient of (5.4), and  $l$  is the characteristic length that will be discussed later. Interesting is that the Nusselt number follows a law that can be described with an empirical equation as

$$Nu = f(Gr, Pr), \quad (5.6)$$

where  $Gr$  and  $Pr$  are other characteristic numbers. Formulae for (5.6) are given in literature, e.g. in [67], for different heat transfer problems. Equations (5.5) and (5.6) lead to an equation for  $\alpha$

$$\alpha = \frac{Nu(Gr, Pr)\lambda}{l}. \quad (5.7)$$

Equation (5.7) inserted in (5.4) solves the heat transfer problem.

- ▶ The *Grashof* number approximates the ratio of the buoyancy to viscous force acting on a fluid. The Grashof number is calculated with

$$Gr = \frac{gl^3}{\nu^2} \beta \Delta T, \quad (5.8)$$

where  $g$  is the acceleration due to Earth's gravity,  $\beta$  is the volumetric thermal expansion coefficient (equal to approximately  $1/T_g$  for ideal fluids, where  $T_g$  is the absolute fluid temperature),  $\nu$  is the kinematic viscosity<sup>1</sup>,  $l$  the characteristic length, and  $\Delta T$  the temperature difference between fluid and considered surface temperature.

- ▶ The *Prandtl* number is approximating the ratio of kinematic viscosity and thermal diffusivity. It is dependent only on the fluid and the fluid state. For air at 20 °C ... 100 °C it is [67]

$$Pr = 0.7081 \dots 0.7004 (= 0.7). \quad (5.9)$$

- ▶ The *Rayleigh* number is defined as

$$Ra = Gr \cdot Pr \quad (5.10)$$

It is a measure of flow condition (laminar or turbulent) of the fluid. When the Rayleigh number is below a critical value for that fluid, laminar flow occurs. Above that critical value the flow condition is turbulent. There exists a third fluid state, where the air is basically not moving, hence for very low Rayleigh numbers the heat transfer is mainly in the form of conduction.

### Formulae for Nusselt numbers

In the last section, the characteristic dimensionless numbers have been introduced, wherewith the thermal problem can be solved. The remaining open question is to find the appropriate function for the Nusselt number  $Nu = Nu(Gr, Pr)$ . For this, in literature empirical formulae are given. The presented equations in this work are from [67]. Formulae for different geometries that are of interest for magnetic components are introduced in the following.

<sup>1</sup>kinematic viscosity of air at 30 °C [67]:  $\nu = 162.6 \cdot 10^{-7} \text{ m}^2/\text{s}$ .

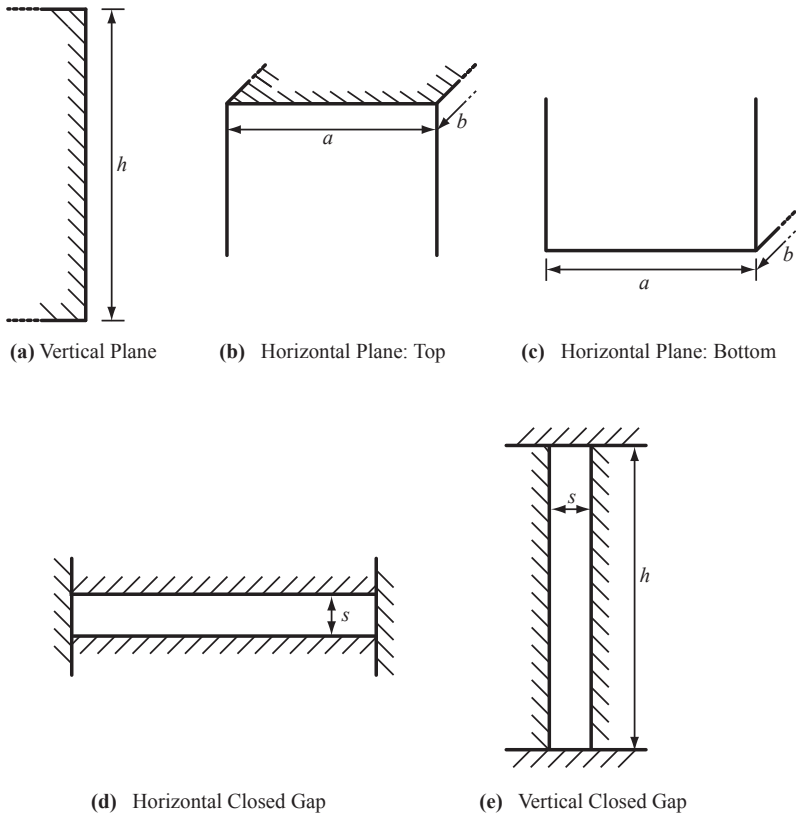


**Figure 5.4:** Illustration of convection geometries.

► **Vertical Plane**

The formula for the Nusselt number to determine the mean heat transfer capability of a vertical plane as illustrated in Figure 5.4(a) is

$$Nu = \left[ 0.825 + 0.387 (Ra \cdot f_1(Pr))^{1/6} \right]^2, \quad (5.11)$$

with

$$f_1 = \left[ 1 + \left( \frac{0.492}{Pr} \right)^{9/16} \right]^{-16/9}. \quad (5.12)$$

The formula above is valid for  $Ra = 10^{-1} \dots 10^{12}$  and  $Pr > 0.001$ . For the characteristic length in (5.5), (5.7), and (5.8) the height  $h$  of the plane is chosen.

► **Horizontal Plane: Heat Emission on Top Side**

The formula for the Nusselt number to determine the mean heat transfer capability of a horizontal plane with heat emission on top side (cf. Figure 5.4(b)) is

$$Nu = \begin{cases} 0.766 (Ra \cdot f_2(Pr))^{1/5} & \text{for } Ra \cdot f_2(Pr) \leq 7 \cdot 10^4 \\ 0.15 (Ra \cdot f_2(Pr))^{1/3} & \text{for } Ra \cdot f_2(Pr) > 7 \cdot 10^4 \end{cases} \quad (5.13)$$

with

$$f_2 = \left[ 1 + \left( \frac{0.322}{Pr} \right)^{11/20} \right]^{-20/11}. \quad (5.14)$$

The characteristic length in (5.5), (5.7), and (5.8) is calculated for rectangular planes of size  $a \times b$  with

$$l = \frac{ab}{2(a+b)}, \quad (5.15)$$

and for circular disks with diameter  $d$  with

$$l = \frac{d}{4}. \quad (5.16)$$

► **Horizontal Plane: Heat Emission on Bottom Side**

The formula for the Nusselt number to determine the mean heat transfer capability of a horizontal plane with heat emission on bottom side (cf. Figure 5.4(c)) is

$$Nu = 0.6 (Ra \cdot f_1(Pr))^{1/5} \quad (5.17)$$

with  $f_1$  according to (5.12). The characteristic length in (5.5), (5.7), and (5.8) is calculated according to (5.15) or (5.16), depending on the geometry.

► **Horizontal Gap**

The air is static in case of a heat transfer from top to bottom in a horizontal gap as illustrated in Figure 5.4(d), hence  $Nu = 1$ .

In case the heat transfer is from bottom to top, the formula for the Nusselt number for the mean heat transfer capability of a horizontal gap is

$$Nu = \begin{cases} 1 & \text{for } Ra < 1708 \\ 0.208Ra^{0.25} & \text{for } 1708 \leq Ra < 2.2 \cdot 10^4 \\ 0.092Ra^{0.33} & \text{for } Ra \geq 2.2 \cdot 10^4 \end{cases} \quad (5.18)$$

For the characteristic length in (5.5), (5.7), and (5.8) the gap length  $s$  of Figure 5.4(d) is chosen.

► **Vertical Gap**

The formula for the Nusselt number for the mean heat transfer capability of a vertical gap as illustrated in Figure 5.4(e) is

$$Nu = \begin{cases} 0.42Pr^{0.012}Ra^{0.25} \left(\frac{h}{s}\right)^{-0.25} & \text{for } 10^4 \leq Ra < 10^7 \\ 0.049Ra^{0.33} & \text{for } 10^7 \leq Ra < 10^9 \end{cases} \quad (5.19)$$

The dimensions  $s$  and  $h$  are illustrated in Figure 5.4(e). For the characteristic length in (5.5), (5.7), and (5.8) the gap length  $s$  is chosen.

Formulae for other geometries and for forced convection are given e.g. in [67].

### 5.2.3 Thermal Radiation

Each surface of an object that has a temperature above absolute zero radiates its thermal energy in the form of electromagnetic waves. The Stefan-Boltzmann law states the total energy radiated per unit surface area of a black body in vacuum

$$q = \sigma T^4, \quad (5.20)$$

with

$$\sigma = \frac{2\pi^5 k^4}{15c^2 h^3}, \quad (5.21)$$

where  $k = 1.38 \cdot 10^{-23}$  J/K is the Boltzmann constant,  $h = 6.62 \cdot 10^{-34}$  Js is Planck's constant, and  $c = 3 \cdot 10^8$  m/s is the speed of light in vacuum.

(5.20) is an idealized equation for a black body that in reality does not exist. The radiation property of a real surface deviates from the

| Material             | $\epsilon$ |
|----------------------|------------|
| Silver (polished)    | 0.02       |
| Copper               | 0.1-0.2    |
| Aluminium (oxidized) | 0.2-0.3    |
| Enamel               | 0.8-0.95   |
| Ceramic              | 0.9-0.95   |

**Table 5.2:** Values for selected emissivities (for an industrial temperature range) [10].

radiation property of a surface of a black body. This is taken into consideration by an empirical correction factor, the emissivity  $\epsilon$ . The emissivity  $\epsilon$  is a function of temperature, emission angle, and wavelength. The Stefan-Boltzmann law for the heat transfer between two surfaces with emissivities  $\epsilon_1$  and  $\epsilon_2$  becomes then [10]

$$P = \epsilon_{\text{eff}} A_1 \sigma (T_1^4 - T_2^4). \quad (5.22)$$

with

$$\epsilon_{\text{eff}} = \begin{cases} \frac{1}{\frac{1}{\epsilon_1} + \frac{A_1}{A_2} \left( \frac{1}{\epsilon_2} - 1 \right)}, \\ \epsilon_1 & \text{for } A_2 \gg A_1. \end{cases} \quad (5.23)$$

In Table 5.2 the emissivities of some selected materials are given. Important to note is that optically transparent materials are not necessarily transparent for heat radiation. For example, for an enamel-insulated wire, the emissivity of enamel has to be taken, not the one of copper.

The linear resistance value of a resistor network can be calculated with (5.22) for one thermal operating point with

$$R = \frac{\Delta T}{P} = \frac{T_1 - T_2}{\epsilon_{\text{eff}} A_1 \sigma (T_1^4 - T_2^4)}. \quad (5.24)$$

## 5.3 Practical Implementation Issues

With above formulae, an arbitrarily magnetic component can be thermally modeled. However, the thermal resistors are nonlinear with tem-



**Figure 5.5:** Illustration of increased winding surface.

perature; therefore, the thermal calculation has to be iteratively performed: first a starting temperature is assumed, then the network is linearized and the calculation is conducted. The calculation is then redone with the new calculated temperature. This is repeated until the algorithm has converged.

Another important thing to be discussed is the actual surface of the component to be modeled. The shape of conductors may increase the surface of the winding-ambient boundary. In case of having round conductors and modeling heat convection, one has to multiply the idealized flat surface with  $\pi/2$  in order to consider the conductor shape. This is illustrated in Figure 5.5. Note that this is not valid for heat radiation, as the round surface does not improve the heat transfer capability and simply leads to heat transfer between nearby conductors.

## Chapter 6

# Magnetic Design Environment and Experimental Results

It is difficult to conduct a calculation that combines all loss and thermal aspects discussed in the previous chapters. The impact of peak-to-peak flux density  $\Delta B$ , frequency  $f$ , DC premagnetization  $H_{DC}$ , temperature, core shape, minor and major loops, flux waveform, and material on core loss calculation have been considered in Chapter 3. In order to calculate winding losses, formulae for round, foil and litz wire conductors, each including skin- and proximity-effects (including the influence of an air-gap fringing field) have been given in Chapter 4. Furthermore, thermal models in order to avoid overheating and improve the model accuracy have been discussed in Chapter 5. In order to handle these models and enable others to determine losses accurately, in the course of this thesis a *Magnetic Design Environment* has been implemented. This environment is introduced in Section 6.1.

Experimental tests that confirm the overall accuracy have been conducted. The experimental results are presented in Section 6.2 and Section 6.3. It will be shown that a high level of accuracy is achieved by combining all loss and thermal models introduced in the previous chapters. More experimental results will be given in Chapter 7, where a design procedure for the mains side LCL filter of an active three-phase rectifier is introduced.

## 6.1 Overview of Implemented Loss Modeling Environment

In order to increase the power density of magnetic components, it is indispensable to model their losses and their thermal behavior accurately. For it, a *Magnetic Design Environment* consisting of a core loss measurement system, a core material database, and magnetic design software has been built. The system is illustrated in Figure 6.1. It applies all models that have been introduced in the previous chapters.

The *Automated Core Loss Measurement System* is being built to analyze core losses under general flux waveform excitation. The built test system is performing all measurements automatically (starts excitation, controls current, regulates flux, triggers the oscilloscope, reads value). Rectangular and sinusoidal voltage excitation is possible when performing such automated measurements. Furthermore, it is possible to automatically extract the relaxation parameters. The idea is to automatically set up the loss map introduced in Section 3.9, which enables an accurate core loss calculation.

The *Core Material Database (Loss Map)* is a database linked to the Automated Core Loss Measurement System. It allows a standardized storage of measurement results. Loss density data are stored in order to calculate core losses of cores of general shapes.

The *Magnetic Design Software* is being built to make magnetic component modeling as simple as possible, while still taking all important loss and thermal effects into consideration. With its graphical user interface it enables a straightforward design of magnetic components. It is possible to read data from the database in order to improve the core loss calculation. Furthermore, it is possible to import voltage and current waveforms simulated on a circuit simulator, such as e.g. Matlab/Simulink, Simplorer, or Gecko Circuits. With it, it is possible to model inductive components under actual in-circuit conditions.

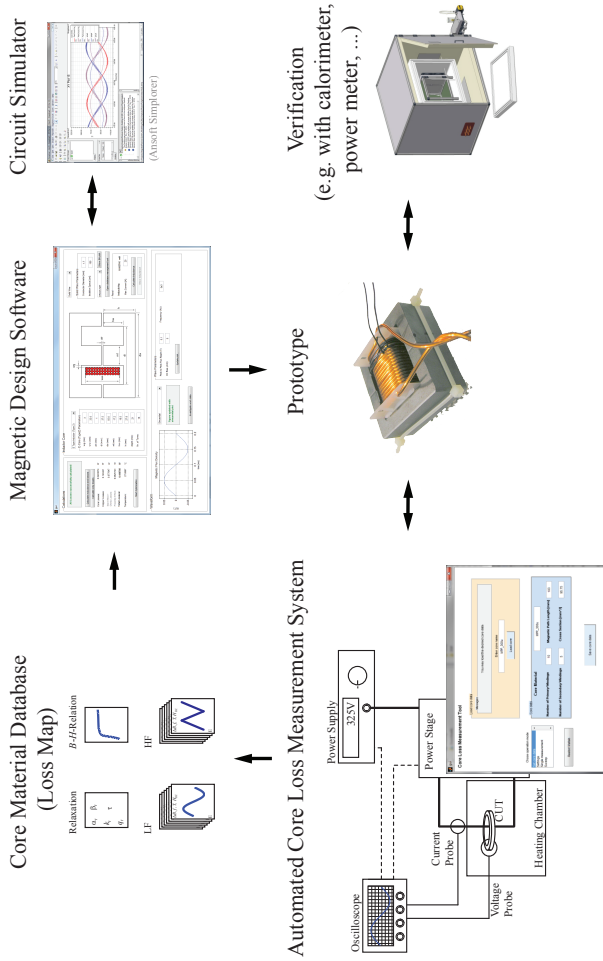


**Figure 6.1:** Illustration of the implemented Magnetic Design Environment.

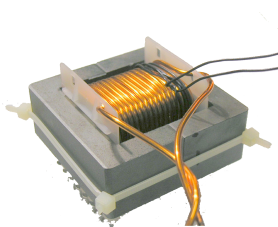


**Figure 6.2:** E-core used for measurements in Experiment I.

## 6.2 Experiment I

Loss measurements have been conducted on an inductor to verify the loss calculations. The inductor has been built with two E-cores having an air gap in the center leg (EPCOS Ferrite N27; Core E55/28/21; air gap length  $l_g = 1$  mm [29]). The windings are made of a solid copper wire with diameter 1.7 mm. The number of turns has been  $N = 18$ . A photo of the inductor is given in Figure 6.2. The measurements have been carried out with a Yokogawa WT3000 Precision Power Analyzer.

Two different types of loss measurements have been performed and compared to loss calculations. The first type of measurements have been conducted with symmetric triangular flux waveforms at different operating points for which the results are given in Table 6.1. The second type of measurements have been conducted with a low frequency LF (100 Hz) sinusoidal current with a superimposed high frequency HF (10 kHz) triangular current ripple. A low modulation index has been chosen, hence the high frequency peak-to-peak flux density  $\Delta B_{HF}$  is (almost) constant over the full low frequency period. The results of the second measurement are given in Table 6.2. A high level of overall accuracy with a maximum deviation of 10% has been achieved.

| Operating Points  |              | Calculated Losses  |                       |                     | Measured Losses     |                   | Comparison |
|-------------------|--------------|--------------------|-----------------------|---------------------|---------------------|-------------------|------------|
| $\Delta B$<br>[T] | $f$<br>[kHz] | Core Losses<br>[W] | Winding Losses<br>[W] | Total Losses<br>[W] | Total Losses<br>[W] | Rel. Error<br>[%] |            |
| 0.25              | 1            | 0.06               | 0.11                  | 0.17                | 0.18                | -5.56             |            |
| 0.5               | 1            | 0.32               | 0.42                  | 0.74                | 0.77                | -3.90             |            |
| 0.25              | 2            | 0.14               | 0.12                  | 0.26                | 0.27                | -3.70             |            |
| 0.5               | 2            | 0.72               | 0.49                  | 1.21                | 1.21                | 0.00              |            |
| 0.25              | 5            | 0.4                | 0.23                  | 0.63                | 0.61                | 3.28              |            |
| 0.5               | 5            | 2.04               | 0.92                  | 2.96                | 2.70                | 9.63              |            |
| 0.1               | 10           | 0.11               | 0.08                  | 0.19                | 0.20                | -3.06             |            |
| 0.2               | 10           | 0.56               | 0.33                  | 0.89                | 0.88                | 1.14              |            |
| 0.3               | 10           | 1.36               | 0.74                  | 2.10                | 2.01                | 4.48              |            |

**Table 6.1:** Results to measurements with symmetric triangular flux waveforms (Experiment I).

| Operating Points      |                        | Calculated Losses  |                       |                     | Measured Losses     |                   | Comparison |
|-----------------------|------------------------|--------------------|-----------------------|---------------------|---------------------|-------------------|------------|
| $\hat{I}_{LF}$<br>[A] | $\Delta B_{LF}$<br>[T] | Core Losses<br>[W] | Winding Losses<br>[W] | Total Losses<br>[W] | Total Losses<br>[W] | Rel. Error<br>[%] |            |
| 5                     | 0.25                   | 0.44               | 0.35                  | 0.79                | 0.76                | 3.95              |            |
| 10                    | 0.5                    | 1.83               | 1.51                  | 3.35                | 3.6                 | -6.94             |            |

**Table 6.2:** Results to measurements with sinusoidal current with a superimposed high frequency triangular current ripple (Experiment I). LF: 100 Hz; HF: 10 kHz.

| Label | Core     | Air gap<br>length [mm] | $N$ | Wire diam.<br>[mm] |
|-------|----------|------------------------|-----|--------------------|
| $L_1$ | E25/13/7 | 1.05                   | 27  | 0.8                |
| $L_2$ | E32/16/9 | 0.55                   | 18  | 0.8                |
| $L_3$ | E20/10/6 | 1                      | 80  | 0.45               |

**Table 6.3:** Different investigated designs in Experiment II for thermal and loss measurements. Cores from EPCOS (material N87).

## 6.3 Experiment II

In the second experiment, thermal and loss measurements on different inductors have been conducted. The different designs are listed in Table 6.3. The loss measurements have been carried out with a Yokogawa WT3000 Precision Power Analyzer. The surface core and surface winding temperatures have been measured with the infrared camera FLIR ThermoCAM. The results are given in Table 6.4, Table 6.5, and Table 6.6. Again, a high level of accuracy with a maximum deviation of 12% in losses and temperatures has been observed.

| Op. Points |              | Calculated Losses and Temperature |                          |                        |                       | Meas. Losses and Temperatures |                      |                       |                          |
|------------|--------------|-----------------------------------|--------------------------|------------------------|-----------------------|-------------------------------|----------------------|-----------------------|--------------------------|
| $\Delta B$ | $f$<br>[kHz] | Core<br>Losses<br>[W]             | Winding<br>Losses<br>[W] | Total<br>Losses<br>[W] | Core<br>Temp.<br>[°C] | Winding<br>Temp.<br>[°C]      | Total<br>Loss<br>[W] | Core<br>Temp.<br>[°C] | Winding<br>Temp.<br>[°C] |
| 0.3        | 10           | 0.07                              | 0.40                     | 0.47                   | 35.6                  | 44.2                          | 0.50                 | 40                    | 49                       |
| 0.3        | 20           | 0.14                              | 0.59                     | 0.73                   | 40.6                  | 52.5                          | 0.74                 | 43                    | 58                       |
| 0.35       | 20           | 0.18                              | 0.81                     | 0.99                   | 45                    | 60.9                          | 1.01                 | 49                    | 66                       |

Table 6.4: Results to inductor  $L_1$  in Experiment II.

| Op. Points |              | Calculated Losses and Temperature |                          |                        |                       | Meas. Losses and Temperatures |                      |                       |                          |
|------------|--------------|-----------------------------------|--------------------------|------------------------|-----------------------|-------------------------------|----------------------|-----------------------|--------------------------|
| $\Delta B$ | $f$<br>[kHz] | Core<br>Losses<br>[W]             | Winding<br>Losses<br>[W] | Total<br>Losses<br>[W] | Core<br>Temp.<br>[°C] | Winding<br>Temp.<br>[°C]      | Total<br>Loss<br>[W] | Core<br>Temp.<br>[°C] | Winding<br>Temp.<br>[°C] |
| 0.3        | 10           | 0.14                              | 0.31                     | 0.45                   | 33.3                  | 38.0                          | 0.45                 | 35                    | 43                       |
| 0.3        | 20           | 0.28                              | 0.37                     | 0.65                   | 37.2                  | 41.4                          | 0.60                 | 37                    | 45                       |
| 0.35       | 20           | 0.38                              | 0.52                     | 0.90                   | 40.7                  | 46.5                          | 0.94                 | 44                    | 52                       |

Table 6.5: Results to inductor  $L_2$  in Experiment II.

| Op. Points |              | Calculated Losses and Temperature |                          |                        |                       | Meas. Losses and Temperatures |                      |                       |                          |
|------------|--------------|-----------------------------------|--------------------------|------------------------|-----------------------|-------------------------------|----------------------|-----------------------|--------------------------|
| $\Delta B$ | $f$<br>[kHz] | Core<br>Losses<br>[W]             | Winding<br>Losses<br>[W] | Total<br>Losses<br>[W] | Core<br>Temp.<br>[°C] | Winding<br>Temp.<br>[°C]      | Total<br>Loss<br>[W] | Core<br>Temp.<br>[°C] | Winding<br>Temp.<br>[°C] |
| 0.3        | 10           | 0.04                              | 0.24                     | 0.28                   | 34.2                  | 40.6                          | 0.27                 | 37                    | 42                       |
| 0.3        | 20           | 0.07                              | 0.33                     | 0.40                   | 37.8                  | 45.7                          | 0.38                 | 39                    | 46                       |
| 0.35       | 20           | 0.10                              | 0.45                     | 0.55                   | 41.5                  | 52.2                          | 0.52                 | 44                    | 52                       |
| 0.4        | 50           | 0.22                              | 1.44                     | 1.66                   | 63.9                  | 96.7                          | 1.60                 | 60                    | 91                       |

**Table 6.6:** Results to inductor  $L_3$  in Experiment II.

## Chapter 7

# Multi-Objective Optimization of Inductive Power Components

The models introduced in the previous chapters will form the basis for the optimization of inductive components employed in key power electronic applications. The aim of this chapter is to use these previously derived models and to show the optimization procedure on a particular example. The chosen example is an LCL input filter structure for a three-phase Power Factor Correction (PFC) rectifier.

LCL input filters are an attractive solution to attenuate switching frequency current harmonics of active voltage source rectifiers [68, 69]. The design procedure for LCL filters based on a generic optimization approach is introduced guaranteeing low volume and/or low losses. Different designs are calculated showing the trade-off between filter volume and filter losses. Furthermore, the converter (consisting of semiconductor switches, DC link capacitor, and cooling system) is also taken into consideration in the optimization procedure. This is necessary as, for instance, a high switching frequency leads to a lower filter volume and losses, but on the other hand, leads to higher switching losses in the semiconductors of the converter. To find the overall optimum, such

| Parameter              | Variable           | Value |     |
|------------------------|--------------------|-------|-----|
| Input Phase Voltage AC | $V_{\text{mains}}$ | 230   | V   |
| Mains Frequency        | $f_{\text{mains}}$ | 50    | Hz  |
| DC-Voltage             | $V_{\text{DC}}$    | 650   | V   |
| Load Current           | $I_L$ (nominal)    | 15.4  | A   |
| Switching Frequency    | $f_{\text{sw}}$    | 8     | kHz |

**Table 7.1:** Specification of the three-phase PFC rectifier.

trade-offs have to be considered. Generally, it is important to consider the system to be optimized as a whole, since there are parameters that bring advantages for one subsystem while deteriorating another subsystem.

In Section 7.1 the three-phase PFC rectifier is introduced, in Section 7.2 the applied models of the LCL filter components are discussed, and in Section 7.3 the optimization algorithm for the LCL filter is described. Simulation and experimental results are given in Section 7.4 and Section 7.5 respectively. In Section 7.6 the converter volume and losses are taken into consideration, i.e. an overall system optimization is performed.

## 7.1 Three-Phase PFC Rectifier with Input Filter

The three-phase PFC rectifier investigated in this work is shown in Figure 7.1. The rectifier comprises in each phase a boost inductor  $L_2$ , a damped LC filter  $L_1/C/C_d/R_d$  and a pair of switches with free-wheeling diodes. The load is assumed to be a DC current source. The considered operating point of the PFC rectifier is described in Table 7.1. A Space Vector Modulation (SVM) scheme with loss-optimal clamping has been implemented and the system is operated with a fundamental displacement factor of  $\cos \phi = 1$ . The functionality and the detailed properties of the used SVM scheme are described in [70]. The three-phase PFC rectifier with input filter has been simulated in MATLAB/Simulink, where the non-linearity of the core material of the inductors, i.e. the change of the inductance value with changing current, is taken into account.

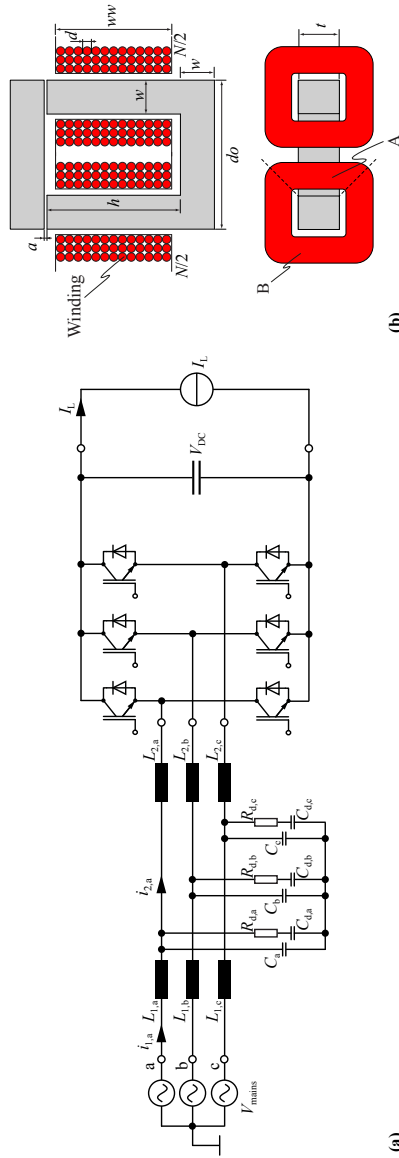


**Figure 7.1:** (a) Three-phase PFC rectifier with LCL input filter. (b) Cross-sections of inductors employed in the input filter.

The three inductors  $L_{1,a}$ ,  $L_{1,b}$ , and  $L_{1,c}$ , and the three capacitors  $C_a$ ,  $C_b$ , and  $C_c$  in star arrangement, together with the three boost inductors  $L_{2,a}$ ,  $L_{2,b}$  and  $L_{2,c}$ , result in a third order LCL low pass filter between the mains and the switching stage. The capacitor/resistor branches  $C_{d,a}/R_{d,a}$ ,  $C_{d,b}/R_{d,b}$ , and  $C_{d,c}/R_{d,c}$  are necessary to damp the resonance of the LC input filter. All inductors are assumed to have the same geometry, which is illustrated in Figure 7.1(b). The cores are made of grain-oriented steel (M165-35S, lamination thickness 0.35 mm). Solid copper wire is taken for the conductors. The windings are divided into two halves arranged on the two legs which leads to a more distributed winding structure. A more distributed winding structure has advantages such as better heat dissipation capabilities, lower inductor volume, etc.

## 7.2 Modeling of Input Filter Components

The modeling of the inductive components has been made according to the discussions in Chapters 2 - 5. In the following, these models are briefly recapitulated. Furthermore, models for capacitors are given, and it is introduced how the damping branch is designed.

### 7.2.1 Calculation of the Inductance

The inductance of an inductive component with  $N$  winding turns and a total magnetic reluctance  $R_{m,tot}$  is calculated as

$$L = \frac{N^2}{R_{m,tot}}. \quad (7.1)$$

Accordingly, the reluctance of each section of the flux path has to be determined first in order to calculate  $R_{m,tot}$ . The total reluctance for a general inductor is calculated as a function of the core reluctances and air gap reluctances. The core and air gap reluctances can be determined applying the methods described in Chapter 2. The reluctances of the core depend on the relative permeability  $\mu_r$  which is extracted from the nonlinear initial B-H-relation of the core material, hence the reluctance is described as a function of the flux. Therefore, as the flux depends on the core reluctance and the reluctance depends on the flux, the system can only be solved iteratively by using a numerical method. In the case at hand, the problem has been solved by applying the Newton approach.

The reluctance model of the inductor of Figure 7.1(b) consists of one voltage source (representing the two separated windings), one air gap reluctance (representing the two air gaps) and one core reluctance.

### 7.2.2 Core Losses

The applied core loss approach is described in Chapter 3 in detail and can be seen as a hybrid of the *improved-improved Generalized Steinmetz Equation*  $i^2$ GSE and a loss map approach: a loss map is experimentally determined and the interpolation and extrapolation for operating points in between the measured values is then made with the  $i^2$ GSE.

The flux density waveform for which the losses have to be calculated is e.g. simulated in a circuit simulator, where the magnetic part is modeled as a reluctance model. This simulated waveform is then divided into its fundamental flux waveform and into piecewise linear flux waveform segments. The loss energy is then calculated for the fundamental and all piecewise linear segments, summed and divided by the fundamental period length in order to determine the average core loss. The DC flux level of each piecewise linear flux segment is considered, as this influences the core losses. Furthermore, the relaxation term of the  $i^2$ GSE is evaluated for each transition from one piecewise linear flux segment to another.

Another aspect to be considered in the core loss calculation is the effect of the core shape/size. By introducing a reluctance model of the core, the flux density can be calculated. Subsequently, for each core section with (approximately) homogenous flux density, the losses can be determined. In the case at hand, the core has been divided into four straight core sections and four corner sections. The core losses of the sections are then summed to obtain the total core losses.

### 7.2.3 Winding Losses

The second source of losses in inductive components are the ohmic losses in the windings. The resistance of a conductor increases with increasing frequency due to eddy currents. Self-induced eddy currents inside a conductor lead to the skin effect. Eddy currents due to an external alternating magnetic field, e.g. the air gap fringing field or the magnetic field from other conductors, lead to the proximity effect.

The sum of the DC losses and the skin effect losses per unit length in round conductors can be calculated with (4.6). The proximity effect



**Figure 7.2:** Thermal model with only one thermal resistance.

losses in round conductors per unit length can be calculated with (4.8). The external magnetic field strength  $H_e$  of every conductor has to be known when calculating the proximity losses. The applied approach is a 2D approach and is described in detail in Chapter 4.

## 7.2.4 Thermal Modeling

A thermal model is important when minimizing the filter volume, since the maximum temperature allowed is the limiting factor when reducing volume. The model used in this work consists of only one thermal resistance  $R_{th}$  and is illustrated in Figure 7.2. The inductor temperature  $T_L$  is assumed to be homogenous; it can be calculated as

$$T_L = T_A + P_{loss}R_{th}, \quad (7.2)$$

where  $P_{loss}$  are the total losses occurring in the inductor, consisting of core and winding losses, and  $T_A$  is the ambient temperature. The ambient temperature  $T_A$  is assumed to be constant at 25 °C.

The heat transfer due to convection is described with

$$P = \alpha A(T_L - T_A), \quad (7.3)$$

where  $P$  is the heat flow,  $A$  the surface area,  $T_L$  the body surface temperature (i.e. inductor temperature), and  $T_A$  the fluid (i.e. ambient air) temperature.  $\alpha$  is a coefficient that is determined by a set of characteristic dimensionless numbers, the Nusselt, Grashof, Prandtl, and Rayleigh numbers. Radiation has to be considered as a second important heat transfer mechanism and is described by the Stefan-Boltzmann law. Details about thermal modeling are given in Chapter 5.

## 7.2.5 Capacitor Modeling

The filter and damping capacitors have been selected from the EPCOS X2 MKP film capacitor series; which have a rated voltage of 305 V. The dissipation factor is specified as  $\tan \delta \leq 1 \text{ W/kvar}$  (at 1 kHz) [71],

which enables an approximation of the capacitor losses. The capacitance density to calculate the capacitors volume can be approximated with  $0.18 \mu\text{F}/\text{cm}^3$ . The capacitance density has been approximated by dividing the capacitance value of several components by the according component volume.

### 7.2.6 Damping Branch

An LC filter is added between the boost inductor and the mains to meet a THD constraint. The additional LC filter changes the dynamics of the converter and may even increase the current ripple at the filter resonant frequency. Therefore, a  $C_d/R_d$  damping branch has been added for damping. In [72, 73] it is described how to optimally choose  $C_d$  and  $R_d$ . Basically, there is a trade-off between the size of damping capacitor  $C_d$  and the damping achieved. For this work,  $C_d = C$  has been selected as it showed to be a good compromise between additional volume needed and a reasonable damping achieved. The value of the damping resistance that leads to optimal damping is then [72, 73]

$$R_d = \sqrt{2.1 \frac{L_1}{C}}. \quad (7.4)$$

The  $C_d/R_d$  damping branch increases the reactive power consumption of the PFC rectifier system. Therefore, often other damping structures, such as the  $R_f-L_b$  series damping structure, are selected [73]. For this work, however, the  $C_d/R_d$  damping branch has been favored as its practical realization is easier and lower losses are expected. Furthermore, as will be seen in Section 7.4, the reactive power consumption of the PFC rectifier system including the damped LC input filter is in the case at hand rather small, and, if necessary, could be actively compensated by the rectifier.

The losses in the damping branch, which occur mainly in the resistors, are calculated and taken into consideration in the optimization procedure as well.

## 7.3 Optimization of the Input Filter

The aim is to optimally design a harmonic filter of the introduced three-phase PFC rectifier. For the evaluation of different filter structures, a

cost function is defined that weights the filter losses and filter volume according to the designer needs. In the following, the steps towards an optimal design are described. All steps are illustrated in Figure 7.4. The optimization constraints are discussed first.

### 7.3.1 Optimization Constraints and Conditions

The high-frequency ripple in the current  $i_{2,a/b/c}$  is limited to the value  $I_{HF,pp,max}$ , which is important as a too high  $I_{HF,pp,max}$ , e.g., impairs controllability (for instance, an accurate current measurement becomes more difficult). Furthermore, the THD of the mains current is limited. In industry a typical value for the THD that is required at the rated operating point is 5% [74]. In the design at hand, a THD limit of 4% is selected in order to have some safety margin. Two other design constraints are the maximum temperature  $T_{max}$  and the maximum volume  $V_{max}$  the filter is allowed to have. A fixed switching frequency  $f_{sw}$  is assumed. The DC link voltage  $V_{DC}$  and the load current  $I_L$  of the converter are also assumed to be given and constant. All constraints/condition values for the current system are given in Figure 7.4.

### 7.3.2 Calculation of $L_{2,min}$

The minimum value of the inductance  $L_{2,min}$  can be calculated based on the constraint  $I_{HF,pp,max}$  as

$$L_{2,min} = \delta_{(100)} \cdot \frac{\frac{2}{3}V_{DC} - \sqrt{2}V_{mains}}{I_{HF,pp,max} \cdot f_{sw}}, \quad (7.5)$$

with the relative turn-on time of the space vector (100) when the current of phase "a" peaks of  $\delta_{(100)} = \frac{\sqrt{3}M}{2} \cos(\pi/6)$ . Equation (7.5) is based on the fact that, in case of a fundamental displacement factor of  $\cos \phi = 1$ , the maximum current ripple  $I_{HF,pp,max}$  occurs when the current reaches the peak value  $\hat{I}_{LF}$  of the fundamental. As a consequence, the minimum value  $L_{2,min}$  has to be met at the current  $\hat{I}_{LF}$ . With the modulation index  $M = \frac{2\sqrt{2}V_{mains}}{V_{DC}}$ , (7.5) becomes

$$L_{2,min} = \frac{\sqrt{3}\sqrt{2}|V_{mains}|}{V_{DC}} \cos(\pi/6) \cdot \frac{\frac{2}{3}V_{DC} - \sqrt{2}V_{mains}}{I_{HF,pp,max} \cdot f_{sw}}. \quad (7.6)$$

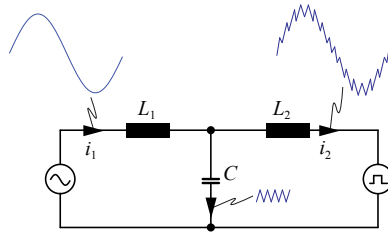


**Figure 7.3:** Idealized current waveforms for each filter component.

### 7.3.3 Loss Calculation of Filter Components

In the foregoing sections (respectively chapters) it has been shown how an accurate loss modeling based on simulated current and voltage waveforms is possible. However, such a calculation based on simulated waveforms is time consuming and therefore, for an efficient optimization, simplifications have to be made. In Figure 7.3, idealized current waveforms for each filter component of a phase are illustrated. The current in  $L_1$  is approximated as purely sinusoidal with a peak value of

$$\hat{I} = \frac{2}{3} \frac{I_L V_{DC}}{\sqrt{2} V_{\text{mains}}}, \quad (7.7)$$

where  $V_{\text{mains}}$  is the RMS value of the mains-phase voltage. The reactive current drawn by the filter capacitors is rather small and has been neglected. With the mains frequency  $f_{\text{mains}} = 50$  Hz, losses, volume, and temperature of  $L_1$  can be calculated.

The current in  $L_2$  has a fundamental (sinusoidal) component, with an amplitude as calculated in (7.7) and a fundamental frequency of  $f_{\text{mains}} = 50$  Hz, and a superimposed ripple current. The ripple current is, for the purpose of simplification, in a first step considered to be sinusoidal with constant amplitude  $I_{\text{HF,pp,max}}$  over the mains period. The losses for the fundamental and the high-frequency ripple are calculated independently, and then summed. By doing this, it is neglected that core losses depend on the DC bias condition and it is neglected that ripple amplitude varies over the cycle.

The ripple current is assumed to be fully absorbed by the filter capacitor  $C$ , hence, with the given dissipation factor  $\tan \delta$ , the losses in the capacitor can be calculated as well.

How the above mentioned simplifications affect the modeling accuracy will be discussed in Section 7.4.

### 7.3.4 Optimization Procedure

After the optimization constraints and the simplifications chosen for the loss calculation have been described, the optimization procedure itself will be explained next.

A filter design is defined by

$$\mathbf{X} = \begin{pmatrix} a_{L_1} & a_{L_2} \\ w_{L_1} & w_{L_2} \\ N_{L_1} & N_{L_2} \\ do_{L_1} & do_{L_2} \\ h_{L_1} & h_{L_2} \\ t_{L_1} & t_{L_2} \\ ww_{L_1} & ww_{L_2} \\ d_{L_1} & d_{L_2} \end{pmatrix}, \quad (7.8)$$

where all inductor parameters are defined as in Figure 7.1(b). The subscripts  $L_1$  and  $L_2$  describe to which inductor each parameter corresponds. The capacitance value of the filter capacitor is calculated based on the  $L_1$  value to guarantee that the THD constraint is met. The parameters in  $X$  are varied by an optimization algorithm to obtain the optimal design. The optimization is based on the MATLAB function `fminsearch()` that applies the Downhill-Simplex-Approach of Nelder and Mead [75].

The optimization algorithm determines the optimal parameter values in  $X$ . A design is optimal when the cost function

$$F = k_{\text{Loss}} \cdot q_{\text{Loss}} \cdot P + k_{\text{Volume}} \cdot q_{\text{Volume}} \cdot V, \quad (7.9)$$

is minimized.  $k_{\text{Loss}}$ ,  $k_{\text{Volume}}$  are weighting factors,  $q_{\text{Loss}}$ ,  $q_{\text{Volume}}$  are proportionality factors, and  $P$ ,  $V$  are the filter losses and filter volume, respectively. The proportionality factors are chosen such that, for a "comparable performance",  $q_{\text{Loss}} \cdot P$  and  $q_{\text{Volume}} \cdot V$  are in the same range<sup>1</sup>. In the case hand, this was achieved with  $q_{\text{Loss}} = 1/W$  and  $q_{\text{Volume}} = 3 \cdot 10^4/\text{m}^3$ .

The following steps are conducted to calculate the filter losses  $P$  and the filter volume  $V$  of (7.9) (cf. Figure 7.4):

---

<sup>1</sup>The filter losses are in the range of approximately 100 W...250 W, whereas the filter volumes are in the range of approximately 0.001 m<sup>3</sup>...0.01 m<sup>3</sup>. With  $q_{\text{Loss}} = 1/W$  and  $q_{\text{Volume}} = 3 \cdot 10^4/\text{m}^3$ , the volume range is lifted to 30...300 and therewith becomes comparable to the losses.

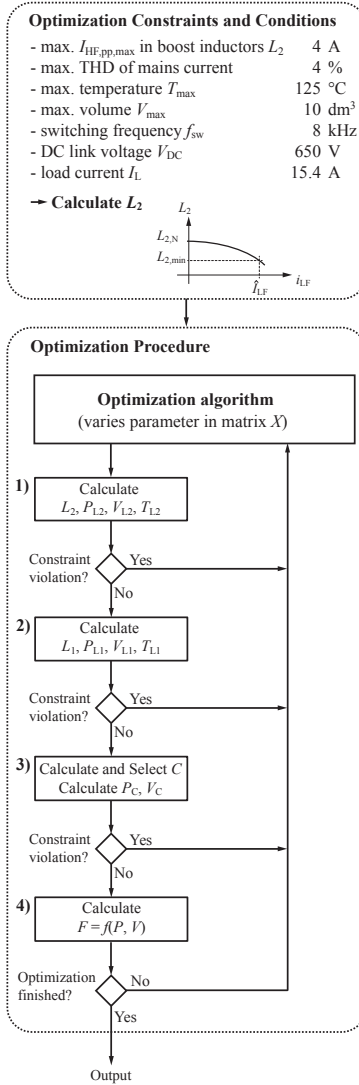


**Figure 7.4:** The design procedure for three-phase LCL filters based on a generic optimization approach.

1. Calculate the inductance value  $L_2$  as a function of the current. Furthermore, the losses  $P_{L_2}$ , the volume  $V_{L_2}$ , and temperature  $T_{L_2}$  of the boost inductors  $L_2$  are calculated. In case a constraint cannot be met, the calculation is aborted and the design is discarded and a new design will be evaluated.
2. Calculate the inductance value  $L_1$  as a function of the current. Furthermore, the losses  $P_{L_1}$ , the volume  $V_{L_1}$ , and temperature  $T_{L_1}$  of the filter inductors  $L_1$  are calculated. In case a constraint cannot be met, the calculation is aborted and the design is discarded and a new design will be evaluated.
3. For the purpose of simplification, the THD without filter is approximated with  $\text{THD} = I_{\text{HF,pp,max}}/I_{(1),\text{pp}}$ , where  $I_{(1),\text{pp}}$  is the fundamental peak-to-peak value of the mains current<sup>2</sup>. Furthermore, it is assumed that the dominant harmonic content appears at  $f_{\text{sw}}$  (this assumption is motivated by simulation results). The LC-filter has then to attenuate the ripple current by

$$A = 20 \log_{10} (I_{(1),\text{pp}} \text{THD}_{\text{max}}/I_{\text{HF,pp,max}}) \quad (7.10)$$

(in dB) at a frequency of  $f_{\text{sw}}$ . Therewith,  $C$  is calculated as

$$C = \frac{1}{L_1 \omega_0^2} = \frac{1}{L_1 (2\pi f_{\text{sw}} \cdot 10^{\frac{A}{40\text{dB}}})^2}, \quad (7.11)$$

where  $\omega_0$  is the filter cutoff frequency. The losses and the volume of the capacitors and damping resistors can then be calculated. In case a constraint cannot be met, the calculation is aborted and the design is discarded and a new design will be evaluated.

4. The volume, temperature, and losses are now known and the cost function (7.9) can be evaluated.

The optimal matrix  $X$  is found by varying the matrix parameters, evaluating these matrixes by repeating the above steps, and minimizing the cost function (7.9). After the optimal design is found, the algorithm quits the loop of Figure 7.4.

---

<sup>2</sup>The THD is defined as  $\text{THD} = \frac{\sqrt{I_2^2 + I_3^2 + I_4^2 + \dots + I_n^2}}{I_1}$ , where  $I_n$  is the RMS value of the  $n^{\text{th}}$  harmonic and  $I_1$  is the RMS value of the fundamental current. Under the assumption that only the dominant harmonic content  $I_{\text{HF,pp,max}}$  (which, for the purpose of simplification, is assumed to appear at one frequency) leads to a harmonic distortion, the THD becomes  $I_{\text{HF,pp,max}}/I_{(1),\text{pp}}$ , consequently.

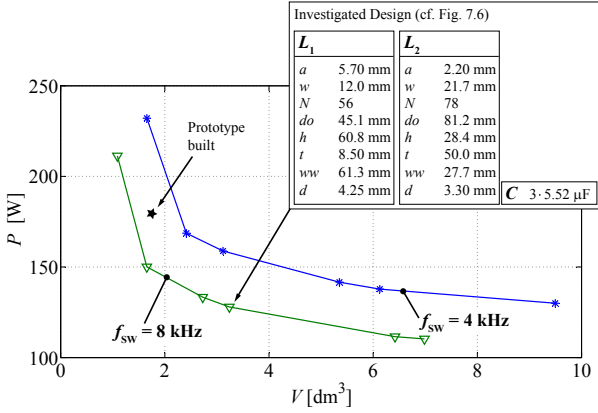


**Figure 7.5:** The  $P$ - $V$ -Pareto front showing filter volumes  $V$  and filter losses  $P$  of different optimal designs.

## 7.4 Optimization Outcomes

The optimization procedure leads to different filter designs depending on the chosen weighting factors  $k_1$  and  $k_2$  in (7.9), i.e. depending whether the aim of the optimization is more on reducing the volume  $V$  or more on reducing the losses  $P$ . Limiting factors are the maximum temperature  $T_{\max}$  (limits the volume from being too low) and a maximum volume  $V_{\max}$  (limits the efficiency from being too high). Different designs are shown by a  $P$ - $V$ -plot, i.e. a  $P$ - $V$ -Pareto front in Figure 7.5; the trade-off between losses and volume can be clearly identified.

One design of Figure 7.5 has been selected for further investigations. Particularly, a comparison between the (for the optimization procedure) simplified and the more elaborate calculation based on voltage / current waveforms from a circuit simulator has been made. The filter parameters of the selected design are detailed in Figure 7.5. The circuit of the three-phase PFC rectifier with the selected input filter has been simulated in MATLAB/Simulink, and the simulated current and voltage waveforms have been taken to calculate the losses according to Section 7.2. The results are given in Figure 7.6. The THD constraint is met and the current  $I_{\text{HF,pp,max}}$  is only insignificantly higher. The simplified loss calculation used for the optimization leads to an over-estimation of the boost inductor losses. This is due to the fact that

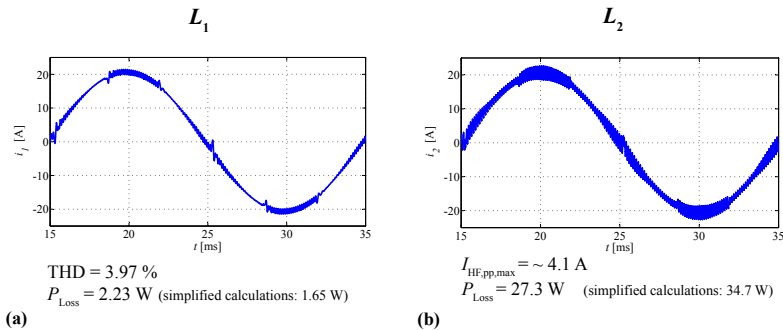


**Figure 7.6:** Simulations and calculations to one selected design (cf. Figure 7.5): (a) filter inductor  $L_{1,a}$ , (b) boost inductor  $L_{2,a}$ .

the maximum ripple current has been assumed to be constant over the mains period. The losses in the filter inductors, on the other hand, have been underestimated as any high frequency ripple in the current through  $L_1$  has been neglected in the simplified calculations. One could try to improve/change the simplifications made for the optimization and therewith improve the simplified loss calculation. However, the difference between the two calculation approaches has been considered as acceptable for this work.

Another important design criteria is the achieved power factor. The reactive power consumption of the the PFC rectifier system, including the damped LC input filter, is in the case at hand rather small (power factor = [real power]/[apparent power] = 0.998).

So far, all results are based on simulations and calculations. The models have to be verified experimentally to prove the validity of the optimization procedure. In the following section experimental results are shown.

## 7.5 Experimental Results

Experimental measurements have been conducted to show that the above introduced calculations are valid. The filter prototype built in the course of this work has been assembled of laminated sheets and coil formers of standard sizes, in order to keep the costs low. This, however, avoids an exact implementation of an optimum as can be seen

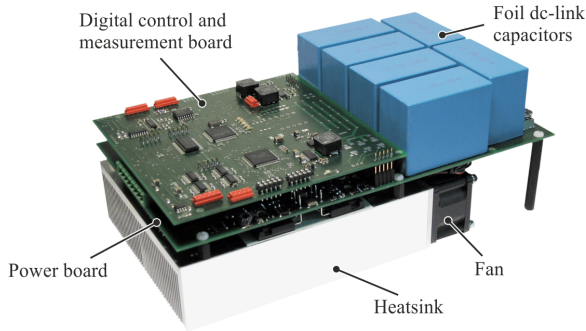


**Figure 7.7:** Photo of the PFC converter.

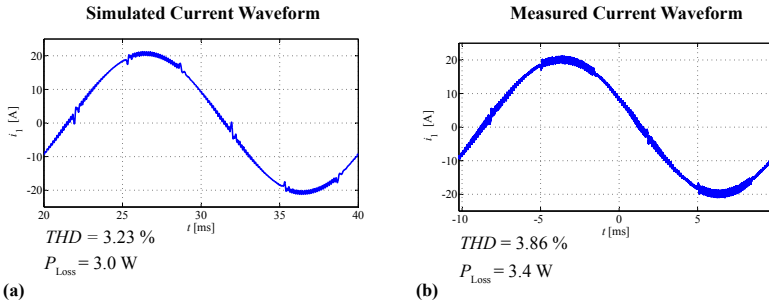


**Figure 7.8:** (a) Simulations and (b) measurements on one of the filter inductors  $L_1$  of the implemented design.

in Figure 7.5 (the prototype built is not on the 8kHz-line). However, this does not impair the significance of the measurement results. Specifications, dimensions and photos of the LCL filter built are given in Figure 7.10. All measurements have been carried out with a Yokogawa WT3000 Precision Power Analyzer.

The measurements have been conducted with the T-type converter introduced in [76]. In Figure 7.7 a photo of the converter is given. The T-type converter is a 3-level converter, however, a 2-level operation is possible as well. A 2-level operation with the same modulation scheme (optimal-loss clamping modulation scheme) as in the MATLAB simulation has been implemented.

The results of the comparative measurements and simulations are given in Figure 7.8 and Figure 7.9. As can be seen, the calculated and

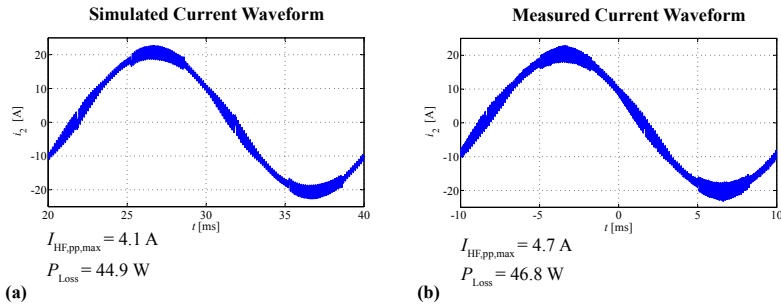


**Figure 7.9:** (a) Simulations and (b) measurements on one of the boost inductors of the implemented design.

measured loss values are very close to each other. The maximum current ripple in the actual system is (slightly) higher than in the simulation. This can be explained by the fact that in the simulation the inductance of the boost inductor is assumed to be constant over the full frequency range. However, in reality the effective inductance decreases with increasing frequency due to inductor losses and parasitic capacitances. The higher THD value can also be explained with the same effect since the filter inductance decreases with increasing frequency as well. The frequency behavior could be modeled analytically by representing the inductors as RLC networks.

## 7.6 Overall Rectifier Optimization

As can be seen in Figure 7.5, an increase in switching frequency leads to lower filter losses and lower filter volumes. However, in return, an increase in switching frequency leads to higher switching losses in the converter semiconductors. In other words, it is important to consider the system as a whole in order to achieve a truly optimal design. In the following, first, a model for the converter is derived, which allows to determine a  $P$ - $V$ -Pareto front of the converter. Later, the trade-off in the switching frequency is illustrated and the optimal frequency for the overall system is determined.

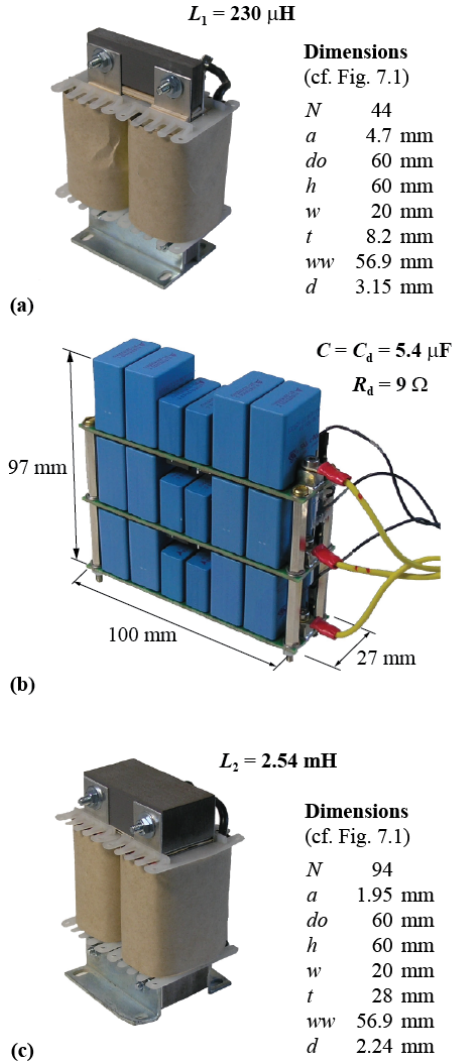


**Figure 7.10:** Specifications, dimensions and photos of (a) one filter inductor  $L_1$ , (b) all filter and damping capacitors/ $C$ ,  $C_d$  and  $R_d$ , and (c) one boost inductor  $L_2$ .



Figure 7.11: Illustration of converter model.

| Parameter                      | Variable                              | Value |                    |
|--------------------------------|---------------------------------------|-------|--------------------|
| Max. junction temp.            | $T_{j,\max}$                          | 125   | $^{\circ}\text{C}$ |
| Max. cooling system vol.       | $V_{\text{CS},\max}$                  | 0.8   | $\text{dm}^3$      |
| Heatsink height                |                                       | 4     | $\text{cm}$        |
| Max. area per chip             | $A_{\text{T},\max}/A_{\text{D},\max}$ | 1     | $\text{cm}^2$      |
| DC link voltage                | $V_{\text{DC}}$                       | 650   | $\text{V}$         |
| Max. DC link voltage overshoot | $\Delta V_{\text{DC}}$                | 50    | $\text{V}$         |
| Fund. peak-peak current        | $I_{(1),\text{pp}}$                   | 20.5  | $\text{A}$         |

Table 7.2: Constraints and conditions for converter optimization.

## 7.6.1 Overall Optimized Designs

The Infineon Trench and Field Stop 1200 V IGBT4 series has been selected to determine the  $P$ - $V$ -Pareto front of the converter. These semiconductors are the same as the ones employed in the converter of Figure 7.7. A converter model has been set up, which determines the junction temperature of the transistors  $T_{j,\text{T}}$ , the junction temperature of the diodes  $T_{j,\text{D}}$ , the volume of the converter  $V$ , and the losses of the converter  $P$ . As input variables it needs the transistor chip area  $A_{\text{T}}$ , the diode chip area  $A_{\text{D}}$ , the cooling system volume  $V_{\text{CS}}$ , and the operating point defined by the switching frequency  $f_{\text{sw}}$  and peak-to-peak fundamental current  $I_{(1),\text{pp}}$ . The high frequency ripple current  $I_{\text{HF},\text{pp}}$  has, as long as  $I_{\text{HF},\text{pp}} \ll I_{(1),\text{pp}}$ , only a negligible impact on the losses and is therewith not taken into consideration. The inputs and outputs of the converter model are illustrated in Figure 7.11 and all optimization constraints and conditions are listed in Table 7.2. This optimization based on the semiconductor chip area is motivated by previously presented works [77, 78].

The thermal resistance of the cooling system, i.e. the heat sink surface to ambient thermal resistance  $R_{\text{th,sa}}$ , has been modeled with the

Cooling System Performance Index (CSPI) [79]; the  $R_{th,sa}$  is then calculated as

$$R_{th,sa} = \frac{1}{CSPI \cdot V_{CS}}, \quad (7.12)$$

where the CSPI can be approximated to be constant for a given cooling concept. The value  $15 \text{ W}/(\text{K} \cdot \text{liter})$  has been calculated for the cooling concept of the converter shown in Figure 7.7 according to [79]. According to [77], for the selected IGBT series the junction-to-sink surface thermal resistance  $R_{th,js}$  can be approximated as a function of the chip area  $A$  as

$$R_{th,js} = 23.94 \frac{\text{K}}{\text{W}} \cdot \left( \frac{A}{\text{mm}^2} \right)^{-0.88}. \quad (7.13)$$

The switching and conduction losses per chip area have been extracted from data sheets. Different IGBTs with different current ratings, but from the same IGBT series have been analyzed. Since the data sheets doesn't provide information about the chip area, the IGBT and diode chip area as a function of the nominal chip current  $I_N$  has to be known in order to determine the losses as a function of the chip area. This chip area-current dependency has been taken from [77] and is for the transistor

$$A_T = 0.95 \frac{\text{mm}^2}{\text{A}} \cdot I_N + 3.2 \text{ mm}^2, \quad (7.14)$$

and for the diode

$$A_D = 0.47 \frac{\text{mm}^2}{\text{A}} \cdot I_N + 3.6 \text{ mm}^2. \quad (7.15)$$

The switching losses scaled to the same current do not vary much with the chip size in the considered range, as a comparison of different data sheets of the selected IGBT series has shown; therefore, for this work, the switching loss energies have been considered as independent of the chip area. The switching loss energies have been extracted at two junction temperatures ( $25^\circ\text{C}$  and  $150^\circ\text{C}$ ) and, for intermediate temperatures, a linear interpolation has been made. These, from the data sheet extracted and interpolated, switching loss energies are then assigned to each switching instant in order to determine the switching losses.

In return, the conduction losses depend on the chip area. This has been modeled as in [78], but with taking the impact of the temperature

into consideration. The following equation describes the conduction losses

$$P_{\text{cond}}(A, i, T_{j,T/D}) = V_f \cdot i + \frac{R_{\text{on},N}(T_{j,T/D}) \cdot A_N}{A} \cdot i^2, \quad (7.16)$$

where  $V_f$  is the forward voltage drop,  $R_{\text{on},N}(T_{j,T/D})$  is the nominal on-resistance,  $A_N$  is the nominal chip area (for which  $R_{\text{on},N}(T_{j,T/D})$  is taken from the data sheet),  $i$  is the current through the transistor, and  $A$  is the actual chip area. The on-resistance has been extracted at two junction temperatures (25 °C and 150 °C) and, for intermediate temperatures, a linear interpolation has been made. The current  $i$  has been calculated for the chosen modulation scheme. Equation (7.16) is evaluated with different values for  $V_f$  and  $R_{\text{on},N}$ , depending whether the conduction losses of the transistor or the diode are calculated.

The converter volume is the sum of the cooling system volume, the DC link capacitor volume, and the volume of the switching devices. The switching device volume has been calculated by multiplying the chip areas by a depth of 1 cm in order to approximate the transistor volume. The cooling system volume is known as it is a model input parameter. The DC link capacitor  $C_{\text{DC}}$  has been selected such that the DC link voltage in case of an abrupt load drop from nominal load to zero load doesn't exceed a predefined value. The maximum DC link voltage increase  $\Delta V_{\text{DC}}$  after the load drop can then be approximated as

$$\Delta V_{\text{DC}} = \frac{1}{C_{\text{DC}}} \frac{3}{2} \frac{\sqrt{2} V_{\text{mains}}}{V_{\text{DC}}} \cdot \left( \frac{\hat{I}_2}{f_{\text{sw}}} + \frac{1}{2} \hat{I}_2 t_{\text{max}} \right),$$

where  $\hat{I}_2$  is the peak value of the phase current through the boost inductor  $L_2$  and  $t_{\text{max}}$  is the time difference between the moment where the system sampled the load drop (i.e. latest  $1/f_{\text{sw}}$  after the load drop occurred, since the sampling interval is  $1/f_{\text{sw}}$ ) and the moment where the DC link voltage peaks (i.e.  $V_{\text{DC}} + \Delta V_{\text{DC}}$  is reached). For the calculation of  $t_{\text{max}}$ , it is assumed that the maximum possible demagnetizing voltage is applied to the boost inductor from the moment the system samples the load drop. The chosen value for the maximum voltage overshoot is  $\Delta V_{\text{DC}} = 50 \text{ V}$ . The DC link capacitors have been selected from the EPCOS MKP DC link film capacitor series; which have a rated voltage of 800 V. The capacitor losses are low and, therefore, have been

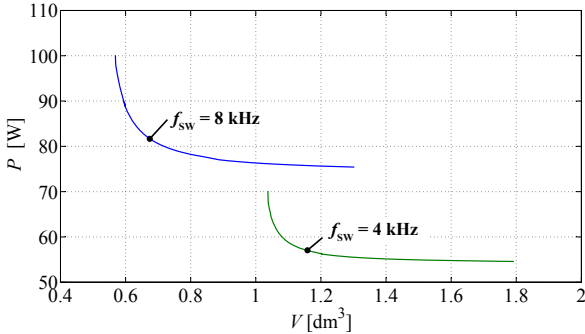


**Figure 7.12:** The  $P$ - $V$ -Pareto front showing converter volumes  $V$  and converter losses  $P$  of different optimal designs.

neglected. The capacitance density to calculate the capacitors volume can be approximated with  $0.6 \mu\text{F}/\text{cm}^3$ .

The losses and volumes of other system parts, such as the DSP, auxiliary supply, gate driver, etc. have not been considered.

An optimization algorithm has been set up similar to that of the filter. A design is characterized by the parameters  $A_T$ ,  $A_D$ , and  $V_{CS}$ . The optimization algorithm varies these parameter in order to find optimal designs. The optimization procedure leads to different designs depending whether the aim of the optimization is more on reducing the volume  $V$  or more on reducing the losses  $P$ . Different designs are shown by a  $P$ - $V$ -plot, i.e. a  $P$ - $V$ -Pareto front in Figure 7.12; the trade-off between losses and volume can be clearly identified. It becomes clear that a higher switching frequency leads to higher losses for a given volume. Therefore, there must exist an overall optimal switching frequency at which the system (including filter) losses are minimized.

Basically, one can combine the results from the filter and from the converter and, therewith, determine the overall system performance. The losses of loss optimized designs for different frequencies have been calculated and are shown in Figure 7.13(a). In the case at hand, the optimal switching frequency is at approximately 5 – 6 kHz. In Figure 7.13(b) the losses of a volumetric optimized designs are given for different frequencies; it can be seen that the optimal switching frequency is in the same range.

In case of loss optimized designs, the major volume part comes from

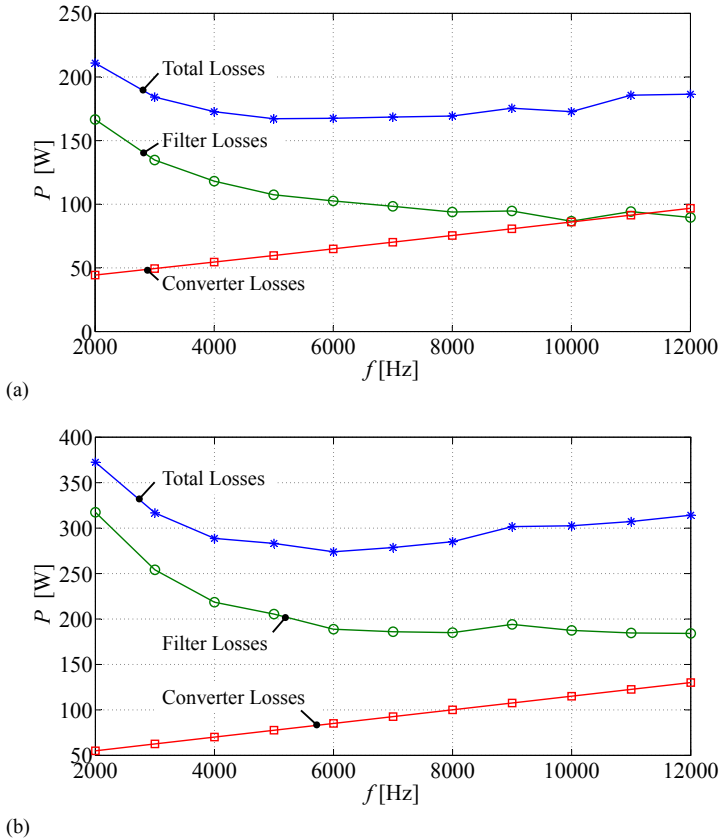


**Figure 7.13:** (a) The losses of loss optimized designs for different frequencies; (b) the losses of volumetric optimized designs for different frequencies.

the filter volume. This becomes clear when Figure 7.5 is compared with Figure 7.12: the maximum filter volume is much higher than the maximum converter volume. This has to do with the selected constraints; however, a further increase of the converter volume wouldn't have a big impact in further decreasing the losses, therefore, it can be concluded that the constraints have been selected well.

In Figure 7.14 the volume of volumetric optimized designs for dif-

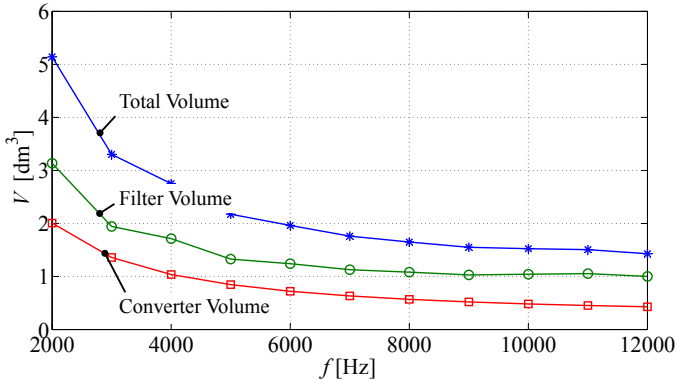


**Figure 7.14:** The volume of volumetric optimized designs for different frequencies.

different frequencies are plotted. As both, the filter size and the converter size, decrease with increasing frequencies, a high frequency is favorable with respect to system size. The converter size decreases with increasing frequency because the DC link capacitance reduces with increasing frequency. The fact that the volume decreases with increasing switching frequency is only true in a limited frequency range; above this frequency range the losses become very high and the size of the components increases again so that the heat can be dissipated. This effect is not visible here.

## 7.7 Conclusion and Future Work

A design procedure for three-phase LCL filters based on a generic optimization approach is introduced guaranteeing low volume and/or low losses. The cost function, which characterizes a given filter design, allows a weighting of the filter losses and of the filter volume according to the designer's need. Different designs have been calculated to show the trade-off between filter volume and filter losses. Experimental results have shown that a very high loss accuracy has been achieved. To improve the THD and current ripple accuracy the frequency behavior of the inductors could be modeled as well.

As can be seen in Figure 7.5, a higher switching frequency leads

to lower filter volume, or, when keeping the volume constant, to lower filter losses. However, higher switching losses are expected in case of higher switching frequencies. Therefore, an overall system optimization, i.e. an optimization of the complete three-phase PFC rectifier including the filter, has been performed. Generally, it is important to consider the system to be optimized as a whole, since there are parameters that bring advantages for one subsystem while deteriorating another subsystem.

# Chapter 8

## Summary & Outlook

### 8.1 Summary

The four steps proposed towards an accurate inductance modeling are:

1. Set up a reluctance model of the inductor that is modeled.
2. Calculate core losses of the inductor.
3. Calculate winding losses of the inductor.
4. Calculate temperatures of the inductor.

The steps 1) to 4) are iteratively repeated until the algorithm has converged.

Step 1 (reluctance model) has been discussed in Chapter 2, where the main focus was put on an accurate air gap reluctance calculation, which is essential when designing inductive components. An approach has been proposed, which is easy-to-handle because of its modular concept (different shapes of air gaps can be built from a simple structure that is easy to calculate), and which still achieves a high level of accuracy as the approach is based on analytical field solutions.

Step 2 (core losses) has been discussed in Chapter 3. For the scientific analysis of core losses as well as for the practical characterization of core materials, a test setup, which allows a core excitation with a wide variety of waveforms, has been built. With it, new core loss models have been derived.

A graph that shows the dependency of the Steinmetz parameters ( $\alpha$ ,  $\beta$  and  $k$ ) on premagnetization, i.e. the *Steinmetz Premagnetization Graph* (SPG) has been introduced. Based on the SPG, the calculation of core losses under DC bias condition becomes possible. This new approach how to describe losses under DC bias condition is promising due to its simplicity.

A new loss model that considers relaxation effects has been proposed. As experimentally verified, core losses are not necessarily zero when zero voltage is applied across a transformer or inductor winding after an interval of changing flux density. A short period after switching the winding voltage to zero, losses still occur in the material. This is due to magnetic relaxation. A new loss modeling approach has been introduced and named the *improved-improved Generalized Steinmetz Equation*,  $i^2\text{GSE}$ . The  $i^2\text{GSE}$  needs five new parameters to calculate new core loss components. Hence, in total eight parameters are necessary to accurately determine core losses.

Other issues have been discussed, such as the impact of the core shape on core losses or how to handle minor and major B-H loops. A high level of accuracy has been achieved by combining the best state-of-the-art approaches with the newly-developed approaches.

Step 3 (winding losses) has been discussed in Chapter 4. Formulae for round conductors, foil conductors and litz wires, each including skin- and proximity effects (including the effect of an air gap fringing field) have been given for the calculation of winding losses. The accuracy has been confirmed by FEM simulations.

Step 4 (temperature) has been discussed in Chapter 5. A thermal model is not only important to avoid overheating; it has also importance to model the losses correctly, as they are influenced by the temperature. Formulae to set up a thermal resistor network have been given. The heat transfer mechanisms are conduction, convection, and radiation.

The steps 1) to 4) lead to an accurate loss and thermal modeling of inductive power components. The concepts and models have been confirmed using the example of an LCL input filter of a three-phase Power Factor Correction (PFC) rectifier in Chapter 7. A multi-objective optimization procedure for three-phase LCL filters based on a generic optimization approach is introduced guaranteeing low volume and/or low losses. The cost function, which characterizes a given filter design, allows a weighting of the filter losses and of the filter volume according to the designer needs. Different designs have been calculated to

show the trade-off between filter volume and filter losses. Experimental results have shown that a very high loss accuracy has been achieved. Furthermore, an overall system optimization, i.e. an optimization of the complete three-phase PFC rectifier including the filter, has been performed.

## 8.2 Outlook

Within the thesis inductive components have been thoroughly modeled and it has been shown how a multi-objective optimization leads to optimal designs of inductive components. However, there are still some (modeling) issues that could be addressed in the future in order to further improve the model applicability. In the following some open tasks are listed, with no claim of completeness.

- ▶ Improvement of measurement system. Particularly, measurements of gapped-cores, cores with low permeability, or measurements at very high frequency are difficult. There are publications addressing this issue, e.g. [13, 46, 47]; however, a solution that is easy to implement and allows any shape of waveform as an excitation would be very interesting to have.
- ▶ In this thesis, a brief overview about tape wound cores and the losses that additionally occur in them has been given. This topic gives opportunities for further research, since, to the author's knowledge, there exists no approach which allows to analytically describe the presented effects.
- ▶ Foil windings in (gapped) inductors. The approach introduced in Section 4.4.5 gives, in a limited range, a reasonably good estimation of the losses. However, its accuracy is much worse compared to any other model discussed in this thesis. An improved model would be very interesting to have.
- ▶ The thermal model presented in this thesis could further be improved. Particularly, a model that determines the thermal resistance of litz wires has, to the authors knowledge, not been successfully addressed yet.
- ▶ A multi-objective optimization procedure, similar as presented in Chapter 7, could be applied to any kind of problem. Therewith

the existing efficiency or loss density boundaries of existing power electronic systems could be determined and possibly shifted to higher levels.

# Appendix A

## Appendix

### A.1 Derivation of the Basic Reluctance

The derivation of the basic reluctance (2.8) is given in this section. All considerations are based on works presented in [9, 18, 21]. A function of the type

$$z = f(t) = x(u, v) + jy(u, v) \quad (\text{A.1})$$

that defines a complex variable  $z = x + jy$  as a function of another complex variable  $t = u + jv$  and preserves angles is termed conformal. Conformal transformations are very helpful to derive solutions of field problems. A transformation equation must be found relating the given field to a simpler one to which a solution is known or easily found.

One particular conformal transformation equation that transforms the real axis of one plane to the boundary of a polygon of another plane was first given, independently, by Schwarz and Christoffel. The transformation is in such a way that the upper half of the first plane transforms into the interior of the polygon.

For the situation illustrated in Figure A.1, the transformation from the real axis of the  $t$ -plane to the polygon boundary in the  $z$ -plane is derived by integrating the equation

$$\frac{dz}{dt} = S(t-a)^{(\alpha/\pi)-1}(t-b)^{(\beta/\pi)-1}(t-c)^{(\gamma/\pi)-1} \dots, \quad (\text{A.2})$$

which is named the *Schwarz-Christoffel differential equation*.  $S$  is a constant,  $a, b, c, \dots$  are points on the real axis in the  $t$ -plane corresponding

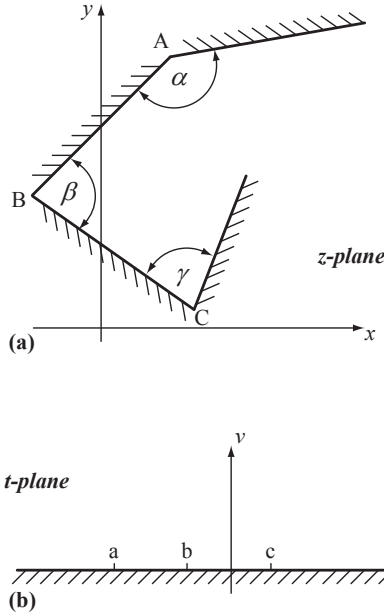


**Figure A.1:** Illustration of Schwarz-Christoffel Transformation.

to the points  $A, B, C, \dots$  in the  $z$ -plane, and  $\alpha, \beta, \gamma, \dots$  are the interior angles of the vertices of the polygon in the  $z$ -plane.

The Schwarz-Christoffel transformations that are used to calculate the reluctance of the basic geometry of Figure 2.3 are given in the following. Two transformation equations have to be found: first a transformation equation that relates the basic geometry in the  $z$ -plane (cf. Figure A.2(a)) to the real axis in the  $t$ -plane (cf. Figure A.2(b)) is derived. Second, a transformation equation that relates the real axis of the  $t$ -plane to a geometry of a parallel-type capacitor (cf. Figure A.2(c)) is further derived. The geometry of a parallel-type capacitor permits easy calculation of the capacitance that, with (2.5), directly leads to the reluctance.

The dashed line in Figure A.2(a) illustrates the chosen polygon structure that will be transformed to the real axis in the  $t$ -plane of Figure A.2(b). In Table A.1 the vertex coordinates of the  $z$ -plane polygon, the vertex angles, and the corresponding points on the real axis of

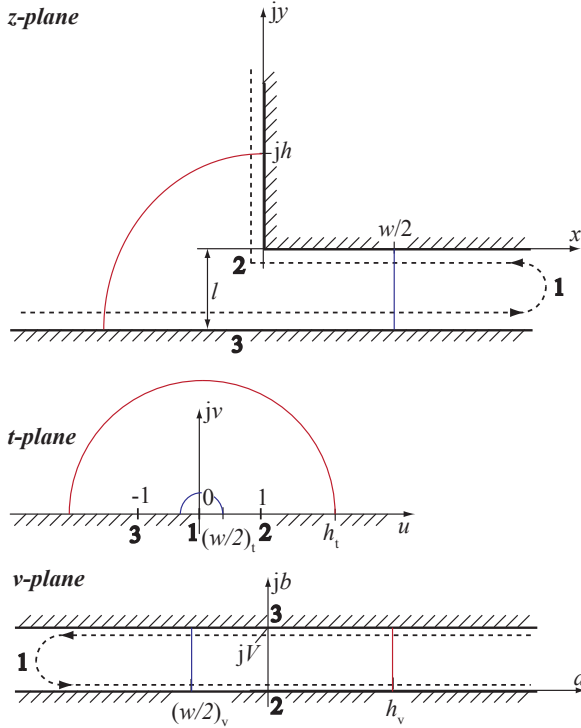


**Figure A.2:** The Schwarz-Christoffel transformation of the basic geometry.

the  $t$ -plane are given. This leads to the Schwarz-Christoffel differential equation

$$\frac{dz}{dt} = S_1 t^{-1} (t-1)^{1/2} = S_1 \frac{\sqrt{t-1}}{t}, \quad (\text{A.3})$$

hence

$$z(t) = -jS_1 (2 \ln(1 + \sqrt{t-1}) - \ln t - 2\sqrt{t-1}) + C_1, \quad (\text{A.4})$$

where  $S_1$  and  $C_1$  are constants that have to be further determined. For  $z(1) = 0$ ,  $C_1$  becomes  $C_1 = 0$ . When  $z(t \rightarrow 0) = \infty$  is assumed for the second boundary condition, some further steps are necessary. Assume

|              | <b>1</b> | <b>2</b> |
|--------------|----------|----------|
| $z_i$        | $\infty$ | 0        |
| $\alpha/\pi$ | 0        | 3/2      |
| $t_i$        | 0        | 1        |

**Table A.1:** Transformation Table 1.

$t = \epsilon e^{j\theta}$  and thus  $dt = j\epsilon e^{j\theta} d\theta$ . For  $t \rightarrow 0$ , (A.3) becomes

$$dz = S_1 \frac{j}{t} dt = j S_1 \frac{j\epsilon e^{j\theta} d\theta}{\epsilon e^{j\theta}} = -S_1 d\theta. \quad (\text{A.5})$$

Near  $t = 0$  (point **1** in Figure A.2),  $z$  varies from  $x - jl$  to  $x$  and  $\theta$  varies from  $\pi$  to zero. Thus,

$$\int_{x-jl}^x dz = - \int_{\pi}^0 S_1 d\theta, \quad (\text{A.6})$$

hence,  $jl = S_1\pi$  or  $S_1 = j\frac{l}{\pi}$ . Thus, the transformation equation is fully described with

$$z(t) = \frac{l}{\pi} \left( 2 \ln(1 + \sqrt{1-t}) - \ln t - 2\sqrt{1-t} \right). \quad (\text{A.7})$$

The transformation equation relating the real axis of the  $t$ -plane to a geometry of a parallel-type capacitor (cf. Figure A.2(c)) will be derived next. The appropriate transformation table is given in Table A.2, which leads to the Schwarz-Christoffel differential equation

$$\frac{dv}{dt} = S_2 t^{-1} = \frac{S_2}{t}, \quad (\text{A.8})$$

hence

$$v(t) = S_2 \ln t + C_2, \quad (\text{A.9})$$

where  $S_2$  and  $C_2$  are constants that have to be further determined. With  $v(1) = 0$ ,  $C_2$  becomes  $C_2 = 0$ . With  $v(-1) = jV$ , where  $V$  represents a constant that will cancel out later,

$$jV = S_2 \ln(-1) = S_2 j\pi, \quad (\text{A.10})$$

|              |           |
|--------------|-----------|
|              | <b>1</b>  |
| $v_i$        | $-\infty$ |
| $\alpha/\pi$ | $0$       |
| $t_i$        | $0$       |

**Table A.2:** Transformation Table 2.

hence,  $S_2 = V/\pi$ . Thus, the transformation equation is

$$v(t) = \frac{V}{\pi} \ln t. \tag{A.11}$$

For the geometry in Figure A.2(c) the capacitance per unit length can be calculated as

$$C' = \epsilon_0 \frac{h_v - \left(\frac{w}{2}\right)_v}{V}, \tag{A.12}$$

where  $h_v$  and  $(w/2)_v$  have to be determined based on the above derived transformation functions. First,  $(w/2)_v$  will be derived. From (A.7) and with  $t \approx 0$

$$\begin{aligned} z(t) = x + j0 &= \frac{l}{\pi} (2 \ln(1 + \sqrt{1-t}) - \ln t - 2\sqrt{1-t}) \\ &= \frac{l}{\pi} (2 \ln 2 - \ln t - 2), \end{aligned} \tag{A.13}$$

hence,

$$-\ln t = \frac{\pi x}{l} + 2(1 - \ln 2). \tag{A.14}$$

With (A.11) and  $x = w/2$ ,  $(w/2)_v$  becomes

$$\left(\frac{w}{2}\right)_v = \frac{V}{\pi} \ln t = -\frac{V}{\pi} \left(\frac{\pi w}{2l} + 2(1 - \ln 2)\right). \tag{A.15}$$

Next,  $h_v$  will be derived. From (A.7) and with  $t \rightarrow \infty$

$$\begin{aligned} z(t) = 0 + jy &= \frac{l}{\pi} (2 \ln(1 + \sqrt{1-t}) - \ln t - 2\sqrt{1-t}) \\ &= \frac{l}{\pi} (\ln(-1) + 2j\sqrt{t}), \end{aligned} \tag{A.16}$$

hence,

$$jy = j \frac{l}{\pi} (\pi + 2\sqrt{t}) \tag{A.17}$$

or

$$\frac{\pi y}{2l} = \frac{\pi}{2} + \sqrt{t}. \quad (\text{A.18})$$

For  $t \rightarrow \infty$ , (A.18) can be simplified to

$$\sqrt{t} \approx \frac{\pi y}{2l} \quad (\text{A.19})$$

and

$$t = \left( \frac{\pi y}{2l} \right)^2 \quad (\text{A.20})$$

With (A.11) and  $y = h$ ,  $h_v$  becomes

$$h_v = \frac{V}{\pi} \ln t = \frac{2V}{\pi} \ln \frac{\pi h}{2l}. \quad (\text{A.21})$$

Therewith, the capacitance of the geometry in Figure A.2 is determined. (A.12) becomes

$$\begin{aligned} C' &= \epsilon_0 \frac{\frac{2V}{\pi} \ln \frac{\pi h}{2l} + \frac{V}{\pi} \left( \frac{\pi w}{2l} + 2(1 - \ln 2) \right)}{V} \\ &= \epsilon_0 \left[ \frac{w}{2l} + \frac{2}{\pi} \left( 1 + \ln \frac{\pi h}{2l} \right) \right]. \end{aligned} \quad (\text{A.22})$$

(2.5) and (A.22) lead to the basic reluctance of (2.8).

## A.2 iGSE and Sinusoidal Flux Waveforms

If one inserts a sinusoidal flux density waveform into the iGSE, its equation transforms back to the Steinmetz equation (3.3). This is shown in the following. The iGSE is given as

$$P_v = \frac{1}{T} \int_0^T k_i \left| \frac{dB}{dt} \right|^\alpha (\Delta B)^{\beta-\alpha} dt \quad (\text{A.23})$$

where  $\Delta B$  is the peak-to-peak flux density and

$$k_i = \frac{k}{(2\pi)^{\alpha-1} \int_0^{2\pi} |\cos \theta|^{\alpha} 2^{\beta-\alpha} d\theta}. \quad (\text{A.24})$$

A sinusoidal flux density waveform  $B(t) = \frac{\Delta B}{2} \cdot \sin 2\pi ft$  with  $\frac{dB(t)}{dt} = 2\pi f \cdot \frac{\Delta B}{2} \cdot \cos 2\pi ft$  inserted in (A.23) leads to

$$P_v = \frac{1}{T} \int_0^T k_i \left| 2\pi f \cdot \frac{\Delta B}{2} \cdot \cos 2\pi ft \right|^\alpha (\Delta B)^{\beta-\alpha} dt. \quad (\text{A.25})$$

Inserting (A.24) into (A.25) and replacing  $1/T$  with  $f$ , one gets

$$P_v = \frac{fk\left(\frac{\Delta B}{2}\right)^\alpha (\Delta B)^{\beta-\alpha} (2\pi f)^\alpha \int_0^T |\cos 2\pi ft|^\alpha dt}{(2\pi)^{\alpha-1} 2^{\beta-\alpha} \int_0^{2\pi} |\cos \theta|^\alpha d\theta}. \quad (\text{A.26})$$

With (substitution of variables)

$$\frac{\int_0^T |\cos 2\pi ft|^\alpha dt}{\int_0^{2\pi} |\cos \theta|^\alpha d\theta} = \frac{1}{2\pi f}, \quad (\text{A.27})$$

(A.26) simplifies to

$$P_v = kf^\alpha \left(\frac{\Delta B}{2}\right)^\beta. \quad (\text{A.28})$$

Equation (A.28) is the Steinmetz equation (3.3).

## A.3 SPGs of Other Materials

In Figure A.3 the SPG is given for the material EPCOS N27, and in Figure A.4 for the material Ferroxcube 3F3. In Figure A.5 the SPG for the nanocrystalline material VITROPERM 500F from Vacuumschmelze (VAC) is depicted. The independency of  $\alpha$  with the frequency has been confirmed for all materials ( $\alpha = \text{constant}$ ). All given SPGs consider only the premagnetization range where it is still appropriate to use the Steinmetz approach, i.e. the losses still follow a power equation.

## A.4 Derivation of the Steinmetz Premagnetization Graph

The Steinmetz parameters as a function of  $H_{\text{DC}}$  are described with a fourth order series expansion

$$\begin{bmatrix} \alpha \\ \beta \\ k_i \end{bmatrix} = \begin{bmatrix} \alpha_0 & 0 & 0 & 0 & 0 \\ \beta_0 & p_{\beta 1} & p_{\beta 2} & p_{\beta 3} & p_{\beta 4} \\ k_{i0} & p_{ki1} & p_{ki2} & p_{ki3} & p_{ki4} \end{bmatrix} \cdot \begin{bmatrix} 1 \\ H_{\text{DC}} \\ H_{\text{DC}}^2 \\ H_{\text{DC}}^3 \\ H_{\text{DC}}^4 \end{bmatrix} \quad (\text{A.29})$$

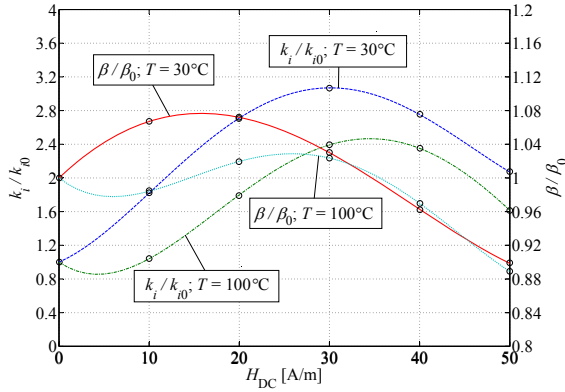


**Figure A.3:** SPG of the material ferrite N27 (EPCOS); measured on R25 core.

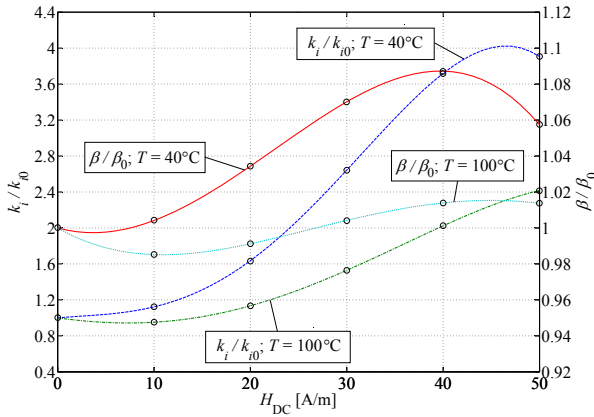


**Figure A.4:** SPG of the material ferrite 3F3 (Ferroxcube); measured on core type TN25/15/10.

or

$$\mathbf{S} = \mathbf{P} \cdot \mathbf{H}. \tag{A.30}$$

To extract the dependency of the Steinmetz parameters on the pre-magnetization, one has to find the right coefficients of the matrix  $\mathbf{P}$ .

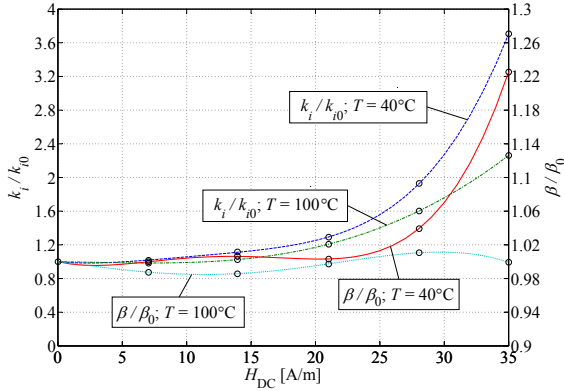


**Figure A.5:** SPG of the material VITROPERM 500F (VAC); measured on W452 core.

This is an optimization problem. A least square algorithm has been implemented that fits measured curves with calculated data by minimizing the relative error at 3 different values of  $\Delta B$ , each measured at two frequencies, and 6 premagnetization values  $H_{DC}$  (including  $H_{DC} = 0$ ). The losses are calculated according to (3.33) with Steinmetz parameters from (A.29)/(A.30). In the initial matrix  $\mathbf{P}$ , all elements  $p_*$  (cf. (A.29)) are set to zero. The values that represent the Steinmetz values under no DC bias condition ( $\alpha_0$ ,  $\beta_0$ , and  $k_{i0}$ ) have reasonable initial values. As an optimization constraint, it is assumed that  $\alpha(H_{DC}) > 1$  and  $\beta(H_{DC}) > 2$  for all values of  $H_{DC}$ . The optimization is based on the MATLAB function `fminsearch()` that applies the Downhill-Simplex-Approach of Nelder and Mead [75]. This optimization procedure leads to graphs for the Steinmetz parameter dependency as Figure 3.23, or normalized to  $\beta_0$  respectively  $k_{i0}$  to the SPG as e.g. shown in Figure 3.24.

For the sake of completeness, a drawback of the chosen straightforward fitting procedure is discussed in the following. The above described fitting procedure to calculate the SPG may, in some cases, result in flawed SPGs that lead to partly wrong core loss calculations. This is illustrated in Figure A.6, where an initial dip in the  $k/k_{i0}$  curve (cf. Figure A.6(a)) leads to an underestimation of core losses for very low values of  $H_{DC}$  (cf. Figure A.6(b)). This behavior is not supported by any mea-

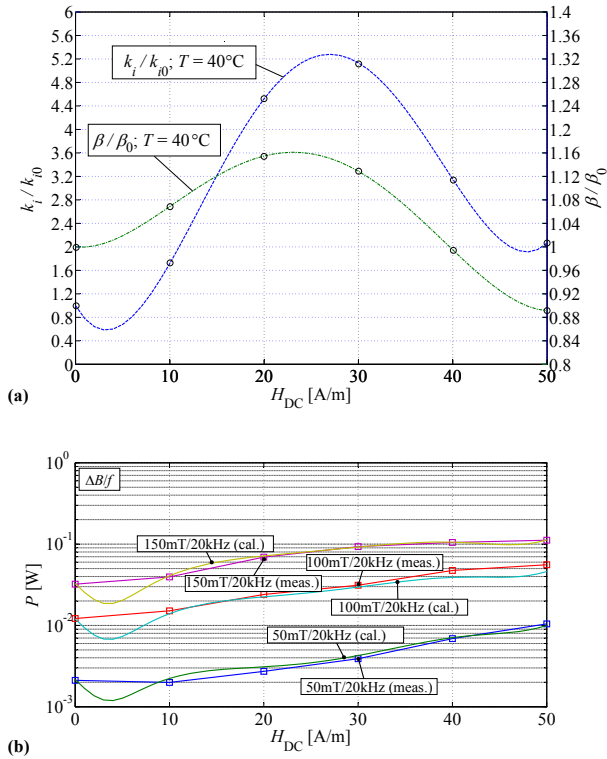


**Figure A.6:** (a) Illustration of a flawed SPG (material ferrite N27 (EPCOS) at  $40^\circ\text{C}$ ; measured on R25 core). The initial dip in the curve  $k/k_{i0}$  is not supported by measurement data and (b) leads to a partly wrong core loss calculation.

surement data. Such interpolation errors could e.g. be avoided/limited by an increase of the  $H_{DC}$  resolution. However, all published SPGs (except the one in Figure A.6) are tested to be (almost) free from anomalies like that.

## A.5 Classic Steinmetz Parameter $k$

A short discussion how to extract the Steinmetz parameter value  $k$  (not  $k_i$ ) from the SPG is given in the following. According to (3.5), for  $k$  we have

$$\frac{k}{k_0} = \frac{k_i(2\pi)^{\alpha-1} \int_0^{2\pi} |\cos \theta|^{\alpha} 2^{\beta-\alpha} d\theta}{k_{i0}(2\pi)^{\alpha-1} \int_0^{2\pi} |\cos \theta|^{\alpha} 2^{\beta_0-\alpha} d\theta} \quad (\text{A.31})$$

that is, under the assumption  $\alpha = \text{constant}$ ,

$$\frac{k}{k_0} = \frac{k_i 2^{\beta}}{k_{i0} 2^{\beta_0}} = \frac{k_i}{k_{i0}} \cdot 2^{\left(\frac{\beta}{\beta_0} - 1\right)\beta_0}, \quad (\text{A.32})$$

where  $\beta/\beta_0$  can be extracted from the SPG. Of course, it is conceivable to write  $k/k_0$  in the SPG, instead of  $k_i/k_{i0}$ . However, because the built test system excites the core with a triangular current shape,  $k_i/k_{i0}$  has been chosen for the graph. The iGSE is in any case very broadly used, hence, to avoid further calculations, to have directly the information about  $k_i$  is often desired.

## A.6 Derivation of Effective Dimensions for Toroidal Cores

In the following, the effective dimensions for toroidal cores (introduced in Section 3.10.1) are derived. The derivations are from [22]. An infinitesimal small flux part is

$$d\Phi = \mu_0 \mu_r H dA = \mu_0 \mu_r \frac{NI}{l} dA, \quad (\text{A.33})$$

where  $\mu_0$  is the magnetic constant,  $\mu_r$  the relative permeability,  $N$  the amount of turns around the core,  $I$  the current through the winding, and  $l$  the magnetic path length. With it, the flux is described by

$$\Phi = \mu_0 NI \int \frac{\mu_r dA}{l}. \quad (\text{A.34})$$

With the second order Peterson relation<sup>1</sup> for the relative permeability  $\mu_r$ , (A.34) can be written as

$$\Phi = \mu_0 NI \left( a_{10} \int \frac{dA}{l} + a_{11} NI \int \frac{dA}{l^2} \right). \quad (\text{A.35})$$

The flux in an equivalent ideal toroid (with dimensions  $l_e$  and  $A_e$ ) is

$$\Phi = \mu_0 NI \mu_r \frac{A_e}{l_e} = \mu_0 NI \left( a_{10} \frac{A_e}{l_e} + a_{11} NI \frac{A_e}{l_e^2} \right). \quad (\text{A.36})$$

By comparison of coefficients in (A.35) and (A.36), it follows that

$$\frac{A_e}{l_e} = \int \frac{dA}{l}, \quad (\text{A.37})$$

and

$$\frac{A_e}{l_e^2} = \int \frac{dA}{l^2}. \quad (\text{A.38})$$

With  $dA = h dr$  and  $l = 2\pi r$  ( $r$  is the radius and  $h$  is the axial thickness), (A.37) and (A.38) can be solved

$$\frac{A_e}{l_e} = \int_{r_1}^{r_2} \frac{h dr}{2\pi r} = \frac{h \ln r_2/r_1}{2\pi}, \quad (\text{A.39})$$

and

$$\frac{A_e}{l_e^2} = \int_{r_1}^{r_2} \frac{h dr}{4\pi^2 r^2} = \frac{h}{4\pi^2} \left( \frac{1}{r_1} - \frac{1}{r_2} \right), \quad (\text{A.40})$$

where  $r_1$  is the inner radius and  $r_2$  the outer radius.

Hence, the effective dimensions for a toroidal core are

$$A_e = \frac{h \ln^2 r_2/r_1}{1/r_1 - 1/r_2}, \quad (\text{A.41})$$

and

$$l_e = \frac{2\pi \ln r_2/r_1}{1/r_1 - 1/r_2}. \quad (\text{A.42})$$

---

<sup>1</sup>Peterson expressed the flux density as a double power series of the instantaneous field strengths  $\mathbf{H}$ . Ignoring the higher powers of  $\mathbf{H}$ , it is

$$\mathbf{B} = \mu_0 (a_{10} \mathbf{H} + a_{11} \mathbf{H}^2)$$

or

$$\mu_r = a_{10} + a_{11} \mathbf{H}$$

[22].

## A.7 Derivation of Winding Losses in Foil Conductors

Within this section, formulae, which allow to quantitatively calculate losses in foil conductors will be derived. The current, voltage and fields are assumed to be sinusoidal, hence the derivative with respect to time  $d/dt$  simplifies to a multiplication with  $j\omega$ . In case of current and voltage shapes that are non-sinusoidal, a Fourier expansion has to be performed first<sup>2</sup>. The presented derivation is from [58, 60].

The Maxwell equations are

$$\operatorname{div} \mathbf{E} = \frac{\rho}{\epsilon} \quad (\text{A.43})$$

$$\operatorname{rot} \mathbf{E} = -j\omega \mathbf{B} \quad (\text{A.44})$$

$$\operatorname{div} \mathbf{B} = 0 \quad (\text{A.45})$$

$$\operatorname{rot} \mathbf{B} = j\omega\epsilon\mu\mathbf{E} + \mu\mathbf{J} \quad (\text{A.46})$$

With the ohmic law  $\mathbf{J} = \sigma\mathbf{E}$ , (A.46) simplifies to

$$\operatorname{rot} \mathbf{B} = (\sigma + j\omega\epsilon)\mu\mathbf{E} \quad (\text{A.47})$$

The substitution of (A.44) in (A.47) leads to

$$\operatorname{rot} \operatorname{rot} \mathbf{E} = \nabla(\operatorname{div} \mathbf{E}) - \nabla^2 \mathbf{E} = -(\sigma + j\omega\epsilon)j\omega\mu\mathbf{E} \quad (\text{A.48})$$

that, with (A.43), can be simplified to

$$\nabla^2 \mathbf{E} = \frac{\nabla\rho}{\epsilon} + (\sigma + j\omega\epsilon)j\omega\mu\mathbf{E}. \quad (\text{A.49})$$

Substituting (A.46) in (A.44), and performing similar transformations as above, leads to

$$\operatorname{rot} \operatorname{rot} \mathbf{B} = \nabla(\operatorname{div} \mathbf{B}) - \nabla^2 \mathbf{B} = -(\sigma + j\omega\epsilon)j\omega\mu\mathbf{B}, \quad (\text{A.50})$$

and, with  $\operatorname{div} \mathbf{B} = 0$  (A.45),

$$\nabla^2 \mathbf{B} = (\sigma + j\omega\epsilon)j\omega\mu\mathbf{B}. \quad (\text{A.51})$$

---

<sup>2</sup>Because of the orthogonality of the cosine/sine-functions, it is valid to perform a Fourier expansion of the current, calculate the loss for each frequency component, and total the losses up (cf. Appendix A.9).

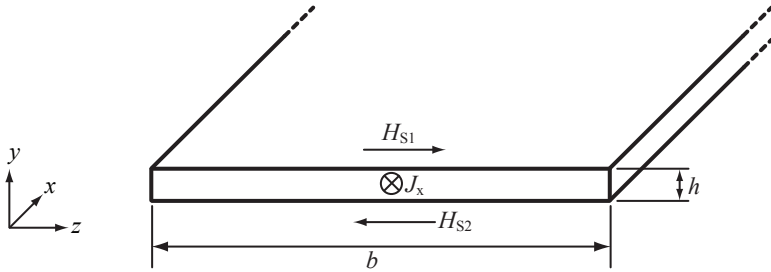


**Figure A.7:** Cross section of a foil conductor with a current density in  $x$ -direction. The conductor is infinitely long in  $x$ -direction.

Equations (A.49) and (A.51) differ in the term  $\frac{\nabla \rho}{\epsilon}$ , that describes the induced charge distribution perpendicular to the current flow, due to an external quasi static electric field. Such an electric field exists, for instance, due to a voltage between the conductors of a winding. In case the displacement current density is neglected<sup>3</sup> and under the assumption of no external quasi static electric field, it is

$$\nabla^2 \mathbf{E} = \mathrm{j}\omega\sigma\mu\mathbf{E}, \quad (\text{A.52})$$

$$\nabla^2 \mathbf{B} = \mathrm{j}\omega\sigma\mu\mathbf{B}, \quad (\text{A.53})$$

and with  $\mathbf{J} = \sigma\mathbf{E}$

$$\nabla^2 \mathbf{J} = \mathrm{j}\omega\sigma\mu\mathbf{J}. \quad (\text{A.54})$$

In the following, formulae for calculating losses, and considering the skin- and proximity-effect, will be derived based on the above derived equations. It is assumed that the current is flowing in  $x$ -direction, with frequency  $f$  and magnitude  $\hat{I}$ .

### A.7.1 Skin Effect

The geometry considered to calculate the skin effect in foil windings is illustrated in Figure A.7. In case of conductor materials with relative permeabilities of unity (e.g. copper), we have  $\mathbf{B} = \mu_0\mathbf{H}$ . Equation (A.53) can then be written as

$$\nabla^2 \mathbf{H} = \alpha^2 \mathbf{H}, \quad (\text{A.55})$$

---

<sup>3</sup>The displacement current density is described with the term  $-\omega\epsilon\mu$  in (A.49) and (A.51).

with

$$\alpha = \frac{1 + j}{\delta}$$

and

$$\delta = \frac{1}{\sqrt{\pi\mu_0\sigma f}}.$$

In a conductor with width  $b$  and height  $h$ , whereas  $h \ll b$ , and whereas the current flows only in  $x$ -direction, the magnetic field strength  $\mathbf{H}$  can be considered as independent of its  $z$  and  $x$  position. Hence, the magnetic field strengths  $\mathbf{H}$  can be described with only a  $z$ -component and, consequently, (A.55) can be simplified to a one dimensional problem

$$\frac{d^2}{dy^2} H_z = \alpha^2 H_z. \quad (\text{A.56})$$

The general solution of (A.56) is

$$H_z = K_1 e^{\alpha y} + K_2 e^{-\alpha y}. \quad (\text{A.57})$$

The magnetic field strengths on the surface (boundary) of the conductor can be calculated with Ampere's Law (cf. Figure A.7) as

$$H_{S1} = -H_{S2} = \frac{\hat{I}}{2b}. \quad (\text{A.58})$$

Out of it, the constants  $K_1$  and  $K_2$  can be determined

$$K_1 = \frac{\hat{I}}{4b \sinh \frac{\alpha h}{a}} = -K_2, \quad (\text{A.59})$$

and the magnetic field strength  $H_z$  becomes

$$H_z = \frac{\hat{I} \sinh \alpha y}{2b \sinh \frac{\alpha h}{2}}. \quad (\text{A.60})$$

With  $dH_z/dy = J_x$  (cf. (A.46) and displacement current density neglected), the current distribution  $J_x$  becomes

$$J_x = \frac{\alpha \hat{I} \cosh \alpha y}{2b \sinh \frac{\alpha h}{2}}. \quad (\text{A.61})$$

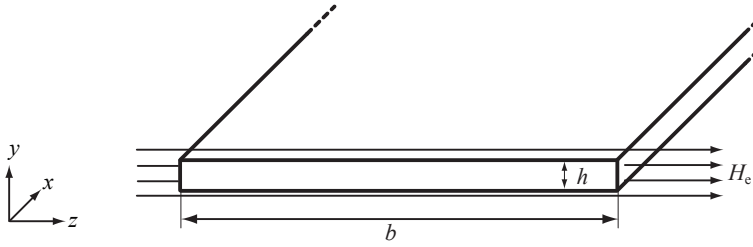


**Figure A.8:** Cross section of a foil conductor that is influenced by an external magnetic field in  $z$ -direction. The conductor is infinitely long in  $x$ -direction.

With the current distribution the ohmic losses per unit length can be calculated as

$$P_S = \frac{b}{2\sigma} \int_0^h |J_x|^2 dy = \frac{\hat{I}^2}{4b\sigma\delta} \frac{\sinh \nu + \sin \nu}{\cosh \nu - \cos \nu}, \quad (\text{A.62})$$

where

$$\nu = \frac{h}{\delta}.$$

Hence, the skin-effect losses (including DC losses) per unit length can be calculated as

$$P_S = F_F(f) \cdot R_{\text{DC}} \cdot \hat{I}^2 \quad (\text{A.63})$$

with

$$\delta = \frac{1}{\sqrt{\pi\mu_0\sigma f}},$$

$$\nu = \frac{h}{\delta},$$

$$R_{\text{DC}} = \frac{1}{\sigma bh},$$

and

$$F_F = \frac{\nu \sinh \nu + \sin \nu}{4 \cosh \nu - \cos \nu}.$$

### A.7.2 Proximity Effect

The geometry considered to calculate the proximity-effect losses in foil windings is illustrated in Figure A.8. On both conductor sides the magnetic field strength in  $z$ -direction has the magnitude  $\hat{H}_e$ . This boundary condition inserted in (A.57) leads to the field distribution

$$H_z = \frac{\cosh \alpha y}{\cosh \frac{\alpha h}{2}} \hat{H}_e \quad (\text{A.64})$$

and with  $dH_z/dy = J_x$  (cf. (A.46) and displacement current density neglected), the current distribution  $J_x$  becomes

$$J_x = \frac{\alpha \sinh \alpha y}{\cosh \frac{\alpha h}{2}} \hat{H}_e. \quad (\text{A.65})$$

With the current distribution the ohmic losses per unit length can be calculated as

$$P_P = \frac{b}{2\sigma} \int_0^h |J_x|^2 dy = \frac{b}{\sigma \delta} \frac{\sinh \nu - \sin \nu}{\cosh \nu + \cos \nu} \hat{H}_e^2 \quad (\text{A.66})$$

with

$$\nu = \frac{h}{\delta}.$$

Hence, the proximity losses per unit length can be written as

$$P_P = R_{\text{DC}} \cdot G_{\text{F}}(f) \cdot \hat{H}_e^2 \quad (\text{A.67})$$

with

$$\delta = \frac{1}{\sqrt{\pi \mu_0 \sigma f}},$$

$$\nu = \frac{h}{\delta},$$

$$R_{\text{DC}} = \frac{1}{\sigma b h},$$

and

$$G_{\text{F}} = b^2 \nu \frac{\sinh \nu - \sin \nu}{\cosh \nu + \cos \nu}.$$

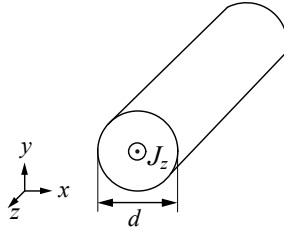


**Figure A.9:** Cross section of the considered round conductor with a current density in  $z$ -direction. The conductor is infinitely long in  $z$ -direction.

## A.8 Derivation of Winding Losses in Round Conductors

In this section, formulae to quantitatively calculate losses in round conductors will be derived. The considered round conductor is illustrated in Figure A.9. The round conductor has a diameter  $d$ , and the length  $l$ , whereas it is assumed that  $d \ll l$ , thus the round conductor is considered as infinitely long in  $z$ -direction. All following calculations are performed in cylindrical coordinates. Furthermore, the magnetic field has only a  $\varphi$ -component (cylindrical coordinates) and the current only an axial  $z$ -component. The presented derivation is from [58, 60].

### A.8.1 Skin Effect

Under the assumption that the problem is cylinder symmetric ( $\frac{\partial}{\partial \varphi} \mathbf{B} = 0$ ) and the displacement current density is neglected, the Maxwell equation (A.46) can be written as (in cylinder coordinates)

$$J_z = \frac{\partial H_\varphi}{\partial r} + \frac{H_\varphi}{r} \quad (\text{A.68})$$

The Maxwell equation (A.44) together with the ohmic law ( $\mathbf{J} = \sigma \mathbf{E}$ ) leads to

$$\frac{\partial J_z}{\partial r} = j\omega\sigma\mu H_\varphi. \quad (\text{A.69})$$

(A.68) and (A.69) lead to the differential equation

$$\frac{d^2}{dr^2} J_z + \frac{1}{r} \frac{d}{dr} J_z = j\omega\sigma\mu J_z \quad (\text{A.70})$$

for the current density inside the conductor. This is a *Bessel differential equation*<sup>4</sup>. The solution of (A.70) is

$$J_z = C \mathbb{J}_0(j^{\frac{3}{2}} \sqrt{\omega \sigma \mu} r), \quad (\text{A.71})$$

where  $\mathbb{J}_v(kx)$  is known as *Bessel function of the first kind* and order  $v$ . The integration constant  $C$  is calculated by integrating the current density

$$I = \iint_{A_L} J_z dA = 2\pi C \int_0^{d/2} r \mathbb{J}_0(j^{\frac{3}{2}} \sqrt{\omega \sigma \mu} r) dr \quad (\text{A.72})$$

where  $A_L$  is the cross section area of the conductor. With  $\int x^v \mathbb{J}_{v-1}(x) dx = x^v \mathbb{J}_v(x) + C$  [59], (A.72) simplifies to

$$I = \frac{2\pi}{j^{\frac{3}{2}} \sqrt{\omega \sigma \mu}} C \frac{d}{2} \mathbb{J}_1(j^{\frac{3}{2}} \sqrt{\omega \sigma \mu} \frac{d}{2}). \quad (\text{A.73})$$

The integration constant  $C$  is eliminated by substituting (A.73) into (A.71), hence

$$J_z = I \frac{j^{\frac{3}{2}} \sqrt{\omega \sigma \mu}}{2\pi \frac{d}{2}} \frac{\mathbb{J}_0(j^{\frac{3}{2}} \sqrt{\omega \sigma \mu} r)}{\mathbb{J}_1(j^{\frac{3}{2}} \sqrt{\omega \sigma \mu} \frac{d}{2})}, \quad (\text{A.74})$$

where  $J_z \in \mathbb{C}$ . On the surface, i.e.  $r = \frac{d}{2}$ , the voltage drop arises from the resistance  $R$  and reactance  $\omega L$ . The voltage drop per unit length is

$$(R + j\omega L)I = I \frac{j^{\frac{3}{2}} \sqrt{\omega \sigma \mu}}{2\pi \frac{d}{2} \sigma} \frac{\mathbb{J}_0(j^{\frac{3}{2}} \sqrt{\omega \sigma \mu} \frac{d}{2})}{\mathbb{J}_1(j^{\frac{3}{2}} \sqrt{\omega \sigma \mu} \frac{d}{2})}. \quad (\text{A.75})$$

To resolve the right-hand side of (A.75) into its real- and imaginary part, the *Kelvin functions* can be used

$$\mathbb{J}_v(j^{\frac{3}{2}} x) = \text{ber}_v x + j \text{bei}_v x. \quad (\text{A.76})$$

After some mathematical conversions, the skin-effect losses (including DC losses) per unit length can be calculated as

$$P_S = R_{\text{DC}} \cdot F_R(f) \cdot \hat{I}^2 \quad (\text{A.77})$$

---

<sup>4</sup>The *Bessel differential equation* has the form  $x^2 y'' + xy' + (k^2 x^2 - v^2)y = 0$ . With the general solution  $y = C_1 \mathbb{J}_v(kx) + C_2 \mathbb{Y}_v(kx)$ , whereas  $\mathbb{J}_v(kx)$  is known as *Bessel function of the first kind* and order  $v$  and  $\mathbb{Y}_v(kx)$  is known as *Bessel function of the second kind* and order  $v$  [59]. Equation (A.70) can be transformed to  $r^2 J_z'' + r J_z' + j^3 \omega \sigma \mu r^2 J_z = 0$ , which is a *Bessel differential equation*.

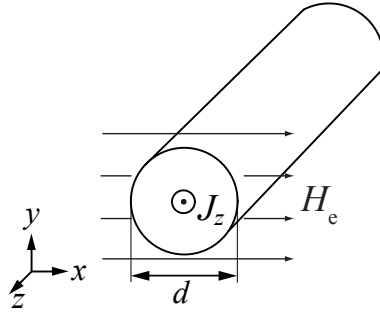


**Figure A.10:** Cross section of a round conductor that is influenced by an external magnetic field in  $x$ -direction. The conductor is infinitely long in  $z$ -direction.

with

$$\delta = \frac{1}{\sqrt{\pi\mu_0\sigma f}},$$

$$\xi = \frac{d}{\sqrt{2}\delta},$$

$$R_{\text{DC}} = \frac{4}{\sigma\pi d^2},$$

and

$$F_{\text{R}} = \frac{\xi}{4\sqrt{2}} \left( \frac{\text{ber}_0(\xi)\text{bei}_1(\xi) - \text{ber}_0(\xi)\text{ber}_1(\xi)}{\text{ber}_1(\xi)^2 + \text{bei}_1(\xi)^2} - \frac{\text{bei}_0(\xi)\text{ber}_1(\xi) + \text{bei}_0(\xi)\text{bei}_1(\xi)}{\text{ber}_1(\xi)^2 + \text{bei}_1(\xi)^2} \right). \quad (\text{A.78})$$

### A.8.2 Proximity Effect

A round conductor with diameter  $d$  that is positioned parallel to the  $z$ -axis is influenced by an alternating magnetic field  $\mathbf{H}(r, \varphi) = H_r(r, \varphi)\mathbf{e}_r + H_\varphi(r, \varphi)\mathbf{e}_\varphi$  with magnitude  $\hat{H}_e$ . The considered situation is illustrated in Figure A.10. The corresponding vector potential has the form  $\mathbf{H}(r, \varphi) = A_z(r, \varphi)\mathbf{e}_z$ , where the vector potential is defined by

$$\mathbf{H} = \text{rot } \mathbf{A}. \quad (\text{A.79})$$

When the displacement current density in the Maxwell equation (A.46) is neglected, it is

$$\mathbf{J} = \text{rot}\mathbf{H} = \text{rot rot } \mathbf{A}, \quad (\text{A.80})$$

hence

$$J_z = -\frac{1}{r} \frac{\partial A_z}{\partial r} - \frac{\partial^2 A_z}{\partial r^2} - \frac{1}{r^2} \frac{\partial^2 A_z}{\partial \varphi^2}. \quad (\text{A.81})$$

With (A.44) ( $\text{rot } \mathbf{E} = -j\omega\mathbf{B}$ ) and the ohmic law ( $\mathbf{J} = \sigma\mathbf{E}$ ), it is

$$\mathbf{J} = -j\sigma\mu\omega\mathbf{A}, \quad (\text{A.82})$$

and the partial differential equation for the vector potential becomes

$$j\sigma\mu\omega A_z = \frac{1}{r} \frac{\partial A_z}{\partial r} + \frac{\partial^2 A_z}{\partial r^2} + \frac{1}{r^2} \frac{\partial^2 A_z}{\partial \varphi^2}. \quad (\text{A.83})$$

How to solve this differential equation is presented in [60]. The solution for the magnetic vector potential  $A_z$  is

$$A_z = \frac{2\mu_0^2 \hat{H}_e}{j^{\frac{3}{2}} \xi} \frac{\mathbb{J}_1(j^{\frac{3}{2}} \xi r)}{\mathbb{J}_0(j^{\frac{3}{2}} \xi \frac{d}{2})} \sin \varphi, \quad (\text{A.84})$$

with

$$\xi = \frac{d}{\sqrt{2}\delta}.$$

The relative permeability  $\mu_r$  of the conductor is considered to be one, which is valid for e.g. copper, aluminium, etc. Also the space around the conductor has the relative permeability of one, as e.g. valid for air. With (A.82) and (A.84), the current density inside the conductor can be calculated

$$J_z = \frac{2\mu_0^2 \hat{H}_e j^{\frac{3}{2}} \xi \mathbb{J}_1(j^{\frac{3}{2}} \xi r)}{\mathbb{J}_0(j^{\frac{3}{2}} \xi \frac{d}{2})} \sin \varphi. \quad (\text{A.85})$$

Out of it, the resulting proximity losses per unit length can be calculated

$$P_P = \frac{1}{2\sigma} \int_0^{2\pi} \int_0^{\frac{d}{2}} |J_z|^2 r dr d\varphi = R_{DC} \cdot G_R(f) \cdot \hat{H}_e^2 \quad (\text{A.86})$$

with

$$\delta = \frac{1}{\sqrt{\pi\mu_0\sigma f}},$$

$$\xi = \frac{d}{\sqrt{2}\delta},$$

$$R_{\text{DC}} = \frac{4}{\sigma\pi d^2},$$

and

$$G_{\text{R}} = -\frac{\xi\pi^2 d^2}{2\sqrt{2}} \left( \frac{\text{ber}_2(\xi)\text{ber}_1(\xi) + \text{ber}_2(\xi)\text{bei}_1(\xi)}{\text{ber}_0(\xi)^2 + \text{bei}_0(\xi)^2} + \frac{\text{bei}_2(\xi)\text{bei}_1(\xi) - \text{bei}_2(\xi)\text{ber}_1(\xi)}{\text{ber}_0(\xi)^2 + \text{bei}_0(\xi)^2} \right). \quad (\text{A.87})$$

## A.9 Orthogonality of Winding Losses

In the derivations in Chapter 4, a current with sinusoidal waveform has been assumed. However, often a non-sinusoidal current is flowing through the conductor. This current can be expressed as a Fourier series with complex fourier coefficients  $\mathbf{I}_v$

$$I(t) = \mathbf{I}_0 + \mathbf{I}_1 \cos \omega t + \mathbf{I}_2 \cos 2\omega t + \mathbf{I}_3 \cos 3\omega t + \dots \quad (\text{A.88})$$

and accordingly, the corresponding current density is

$$J(x, y, t) = \mathbf{J}_0 + \mathbf{J}_1 \cos \omega t + \mathbf{J}_2 \cos 2\omega t + \mathbf{J}_3 \cos 3\omega t + \dots \quad (\text{A.89})$$

The losses per-unit-length are

$$P = \frac{1}{T\sigma} \int_A \int_0^T |J(x, y, t)|^2 dt dA \quad (\text{A.90})$$

with  $A$  the conductor cross section, and  $T$  the current period. Because of the orthogonality of the cosine-function, the product of two Fourier parts with different frequencies is zero ( $\int_0^{2\pi} \cos kx \cdot \cos lx dx = 0$  for  $l \neq k$ ), hence

$$P = \frac{1}{2\sigma} \sum_{i=0}^{\infty} \int_A \mathbf{J}_i \mathbf{J}_i^* dA. \quad (\text{A.91})$$

The part  $\mathbf{J}_i$  can be split into the current density due to skin-  $\mathbf{J}_{\text{Si}}$  and due to proximity-effect  $\mathbf{J}_{\text{Pi}}$

$$P = \frac{1}{2\sigma} \sum_{i=0}^{\infty} \int_A (\mathbf{J}_{\text{Si}} + \mathbf{J}_{\text{Pi}})(\mathbf{J}_{\text{Si}}^* + \mathbf{J}_{\text{Pi}}^*) dA. \quad (\text{A.92})$$

When a conductor has an axis of symmetry and the applied field is uniform and parallel to the symmetry axis (as in round-, or foil conductors), the current density due to the skin effect  $J_S$  has an even symmetry, while the current density due to the proximity effect  $J_P$  has an odd symmetry [63]. Consequently, it is  $\int_A J_P \cdot J_S dA = 0$  and (A.92) simplifies to

$$P = \frac{1}{2\sigma} \sum_{i=0}^{\infty} \int_A (\mathbf{J}_{S_i} \mathbf{J}_{S_i}^* + \mathbf{J}_{P_i} \mathbf{J}_{P_i}^*) dA \quad (\text{A.93})$$

$$= \sum_{i=0}^{\infty} (P_{S_i} + P_{P_i}). \quad (\text{A.94})$$

Above it is shown that the assumption to directly sum the skin- and proximity losses is valid. Furthermore, because of the orthogonality of the cosine-function, it is valid to perform a Fourier expansion of the current, calculate the loss for each frequency component, and total the losses up.



# Bibliography

- [1] Steven Milunovich and Jose Rasco. The sixth revolution: The coming of cleantech. *Merrill Lynch Report*, Nov. 2008.
- [2] B. K. Bose. Energy, environment, and advances in power electronics. *IEEE Transactions on Power Electronics*, 15(4):688–701, 2000.
- [3] G. Andersson. Power electronics solutions for sustainability. In *Proc. of the IEEE Power Engineering Society General Meeting*, pages 2304–2308, 2004.
- [4] J. W. Kolar, J. Biela, S. Waffler, T. Friedli, and U. Badstuebner. Performance trends and limitations of power electronic systems. In *Proc. of the 6th International Conference on Integrated Power Electronics Systems (CIPS)*, pages 1–20, 2010.
- [5] Alex van den Bossche and Vencislav Cekov Valchev. *Inductors and Transformers for Power Electronics*. CRC Press, Taylor & Francis Group, 2005.
- [6] I. Villar, U. Viscarret, I. Etxeberria-Otadui, and A. Rufer. Global loss evaluation methods for nonsinusoidally fed medium-frequency power transformers. *IEEE Transactions on Industrial Electronics*, 56(10):4132–4140, Oct. 2009.
- [7] R. Petkov. Optimum design of a high-power, high-frequency transformer. *IEEE Transactions on Power Electronics*, 11(1):33–42, Jan. 1996.
- [8] Thomas Komma. *Allgemein gültiger Entwurfsalgorithmus für magnetische Komponenten in Schaltnetzteilen mit unterschiedlichen*

- Topologien und Schaltfrequenzen bis 2 MHz*. PhD thesis, Technische Universität Dresden, 2005.
- [9] Peter Wallmeier. *Automatisierte Optimierung von induktiven Bauelementen für Stromrichteranwendungen*. PhD thesis, Universität - Gesamthochschule Paderborn, 2001.
- [10] Ansgar Brockmeyer. *Dimensionierungswerkzeug für magnetische Bauelemente in Stromrichteranwendungen*. PhD thesis, RWTH Aachen, 1997.
- [11] J. Reinert, A. Brockmeyer, and R. De Doncker. Calculation of losses in ferro- and ferrimagnetic materials based on the modified Steinmetz equation. *IEEE Transactions on Industry Applications*, 37(4):1055–1061, 2001.
- [12] C. A. Baguley, B. Carsten, and U. K. Madawala. The effect of DC bias conditions on ferrite core losses. *IEEE Transactions on Magnetics*, 44(2):246–252, Feb. 2008.
- [13] C. A. Baguley, U. K. Madawala, and B. Carsten. A new technique for measuring ferrite core loss under DC bias conditions. *IEEE Transactions on Magnetics*, 44(11):4127–4130, 2008.
- [14] G. Niedermeier and M. Esguerra. Measurement of power losses with DC bias - The Displacement Factor. In *Proc. of PCIM*, pages 169–174, 2000.
- [15] A. Brockmeyer. Experimental evaluation of the influence of DC-premagnetization on the properties of power electronic ferrites. In *Proc. of the 11<sup>th</sup> Annual Applied Power Electronics Conference (APEC)*, volume 1, pages 454–460, 3–7 March 1996.
- [16] M. S. Lancarotte, C. Goldemberg, and Ad. A. Penteadó. Estimation of FeSi core losses under PWM or DC bias ripple voltage excitations. *IEEE Transactions on Energy Conversion*, 20(2):367–372, 2005.
- [17] Manfred Albach. *Grundlagen der Elektrotechnik 1*. Pearson Studium, 2008.
- [18] K. J. Binns, P. J. Lawrenson, and C. W. Trowbridge. *The Analytical and Numerical Solution of Electric and Magnetic Fields*. John Wiley & Sons, Inc., 1992.

- [19] Miles Walker. *The Schwarz-Christoffel transformation and its applications - A simple exposition*. Dover Publications, Inc., 1964.
- [20] J. J. Thomson. *Notes on recent researches in electricity and magnetism*. Oxford, 1893.
- [21] A. Balakrishnan, W. T. Joines, and T. G. Wilson. Air-gap reluctance and inductance calculations for magnetic circuits using a Schwarz-Christoffel transformation. *IEEE Transactions on Power Electronics*, 12(4):654–663, July 1997.
- [22] E. C. Snelling. *Soft Ferrites, Properties and Applications*. 2<sup>nd</sup> edition. Butterworths, 1988.
- [23] Marian K. Kazimierczuk. *High-Frequency Magnetic Components*. John Wiley & Sons, Inc., 2009.
- [24] Ned Mohan, Tore M. Undeland, and William P. Robbins. *Power Electronics - Converters, Applications, and Design*. John Wiley & Sons, Inc., 2003.
- [25] A. F. Hoke and C. R. Sullivan. An improved two-dimensional numerical modeling method for E-core transformers. In *Proc. of the Applied Power Electronics Conference and Exposition (APEC)*, pages 151–157, 2002.
- [26] Herbert C. Roters. *Electromagnetic Devices*. John Wiley & Sons, Inc., 1944.
- [27] A. van den Bossche, V. Valchev, and T. Filchev. Improved approximation for fringing permeances in gapped inductors. In *Proc. of the 37th IAS Annual Meeting*, volume 2, pages 932–938, 2002.
- [28] C. Marxgut, J. Mühlethaler, F. Krismer, and J. W. Kolar. Multi-objective optimization of ultra-flat magnetic components with a PCB-integrated core. In *Proc. of the 8th International Conference on Power Electronics - ECCE Asia*, pages 460–467, 2011.
- [29] *Ferrites and Accessories, Edition 2007*. EPCOS AG.
- [30] J. B. Goodenough. Summary of losses in magnetic materials. *IEEE Transaction on Magnetics*, 38(5):3398–3408, Sept. 2002.

- [31] B. D. Cullity and C. D. Graham. *Introduction to Magnetic Materials*. John Wiley & Sons, Inc., 2009.
- [32] Soshin Chikazumi. *Physics of Ferromagnetism*. Oxford University Press, 1997.
- [33] Giorgio Bertotti. *Hysteresis in Magnetism*. Academic Press, Inc., 1998.
- [34] J. Li, T. Abdallah, and C. R. Sullivan. Improved calculation of core loss with nonsinusoidal waveforms. In *Proc. of the 36<sup>th</sup> IEEE IAS Annual Meeting*, volume 4, pages 2203–2210, 2001.
- [35] K. Venkatachalam, C. R. Sullivan, T. Abdallah, and H. Tacca. Accurate prediction of ferrite core loss with nonsinusoidal waveforms using only Steinmetz parameters. In *Proc. of IEEE Workshop on Computers in Power Electronics*, pages 36–41, 2002.
- [36] J. Biela, U. Badstuebner, and J. W. Kolar. Impact of power density maximization on efficiency of DC-DC converter systems. *IEEE Transactions on Power Electronics*, 24(1):288–300, Jan. 2009.
- [37] S. Iyasu, T. Shimizu, and K. Ishii. A novel iron loss calculation method on power converters based on dynamic minor loop. In *Proc. of European Conference on Power Electronics and Applications*, pages 2016–2022, 2005.
- [38] T. Shimizu and K. Ishii. An iron loss calculating method for AC filter inductors used on PWM inverters. In *Proc. of 37<sup>th</sup> IEEE Power Electronics Specialists Conference (PESC)*, pages 1–7, 2006.
- [39] K. Terashima, K. Wada, T. Shimizu, T. Nakazawa, K. Ishii, and Y. Hayashi. Evaluation of the iron loss of an inductor based on dynamic minor characteristics. In *Proc. of European Conference on Power Electronics and Applications*, pages 1–8, 2007.
- [40] W. A. Roshen. A practical, accurate and very general core loss model for nonsinusoidal waveforms. *IEEE Transactions on Power Electronics*, 22(1):30–40, 2007.
- [41] C. R. Sullivan, J. H. Harris, and E. Herbert. Core loss predictions for general PWM waveforms from a simplified set of measured data. In *Proc. of Applied Power Electronics Conference and Exposition (APEC)*, pages 1048–1055, 2010.

- [42] B. Carsten. Why the magnetics designer should measure core loss; with a survey of loss measurement techniques and a low cost, high accuracy alternative. In *Proc. of PCIM*, pages 163–179, 1995.
- [43] F. Dong Tan, J. L. Vollin, and S. M. Cuk. A practical approach for magnetic core-loss characterization. *IEEE Transactions on Power Electronics*, 10(2):124–130, Mar. 1995.
- [44] W. Shen, F. Wang, D. Boroyevich, and C. W. Tipton. Loss characterization and calculation of nanocrystalline cores for high-frequency magnetics applications. *IEEE Transactions on Power Electronics*, 23(1):475–484, Jan. 2008.
- [45] V. J. Thottuvelil, T. G. Wilson, and H. A. Owen. High-frequency measurement techniques for magnetic cores. *IEEE Transactions on Power Electronics*, 5(1):41–53, Jan. 1990.
- [46] M. Mu, Q. Li, D. Gilham, F. C. Lee, and K. D. T. Ngo. New core loss measurement method for high frequency magnetic materials. In *Proc. of IEEE Energy Conversion Congress and Exposition (ECCE)*, pages 4384–4389, 2010.
- [47] Yehui Han, G. Cheung, An Li, C. R. Sullivan, and D. J. Perreault. Evaluation of magnetic materials for very high frequency power applications. *IEEE Transactions on Power Electronics*, 27(1):425–435, Jan. 2012.
- [48] F. Krismer and J. W. Kolar. Accurate power loss model derivation of a high-current dual active bridge converter for an automotive application. *IEEE Transactions on Industrial Electronics*, 57(3):881–891, 2010.
- [49] M. Hartmann, J. Miniboeck, and J. W. Kolar. A three-phase delta switch rectifier for more electric aircraft applications employing a novel PWM current control concept. In *Proc. of the Applied Power Electronics Conference and Exposition (APEC)*, pages 1633–1640, Feb. 2009.
- [50] Alexander Stadler. *Messtechnische Bestimmung und Simulation der Kernverluste in weichmagnetischen Materialien*. PhD thesis, Universität Erlangen - Nürnberg, 2009.
- [51] Ferroxcube data sheet to material 3E6, Sep. 2008.

- [52] F. G. Brockman, P. H. Dowling, and W. G. Steneck. Dimensional effects resulting from a high dielectric constant found in a ferro-magnetic ferrite. *Physical Review*, 77(1):85–93, January 1950.
- [53] H. Kakehashi and Y. Ohta. A study of amorphous alloy cutting core. *IEEE Translation Journal on Magnetics in Japan*, 1(5):608–609, 1985.
- [54] W. Shen, F. Wang, D. Boroyevich, and C. W. Tipton. High-density nanocrystalline core transformer for high-power high-frequency resonant converter. *IEEE Transactions on Industry Applications*, 44(1):213–222, 2008.
- [55] H. Fukunaga, T. Eguchi, Y. Ohta, and H. Kakehashi. Core loss in amorphous cut cores with air gaps. *IEEE Transactions on Magnetics*, 25(3):2694–2698, 1989.
- [56] H. Fukunaga, T. Eguchi, K. Koga, Y. Ohta, and H. Kakehashi. High performance cut cores prepared from crystallized Fe-based amorphous ribbon. *IEEE Transactions on Magnetics*, 26(5):2008–2010, 1990.
- [57] B. Cougo, A. Tüysüz, J. Mühlethaler, and J. W. Kolar. Increase of tape wound core losses due to interlamination short circuits and orthogonal flux components. In *Proc. of the 37th Annual Conference of the IEEE Industrial Electronics Society (IECON)*, 2011.
- [58] Jürgen Biela. *Optimierung des elektromagnetisch integrierten Serien-Parallel-Resonanzkonverters mit eingepprägtem Ausgangsstrom*. PhD thesis, ETH Zurich, 2005.
- [59] Larry C. Andrews. *Elementary Partial Differential Equations with Boundary Value Problems*. Academic Press College Division, 1986.
- [60] Jiri Lammeraner and Milos Staffl. *Eddy Currents*. Iliffe Books Ltd., 1966.
- [61] P. L. Dowell. Effects of eddy currents in transformer windings. *Proceedings of the Institution of Electrical Engineers*, 113(8):1387–1394, 1966.
- [62] J. A. Ferreira. *Electromagnetic Modelling of Power Electronic Converters*. Kluwer Academics Publishers, 1989.

- [63] J. A. Ferreira. Improved analytical modeling of conductive losses in magnetic components. *IEEE Transactions on Power Electronics*, 9(1):127–131, Jan. 1994.
- [64] C. R. Sullivan. Optimal choice for number of strands in a litz-wire transformer winding. *IEEE Transactions on Power Electronics*, 14(2):283–291, March 1999.
- [65] H. Rossmanith, M. Doebroenti, M. Albach, and D. Exner. Measurement and characterization of high frequency losses in nonideal litz wires. *IEEE Transactions on Power Electronics*, 26(11):3386–3394, 2011.
- [66] P. Wallmeier. Improved analytical modeling of conductive losses in gapped high-frequency inductors. *IEEE Transactions on Industry Applications*, 37(4):1045–1054, 2001.
- [67] *VDI-Wärmeatlas*. Springer-Verlag Berlin Heidelberg, 2006.
- [68] M. Liserre, F. Blaabjerg, and S. Hansen. Design and control of an LCL-filter-based three-phase active rectifier. *IEEE Transactions on Industry Applications*, 41:1281–1291, 2005.
- [69] S. V. Araujo, A. Engler, B. Sahan, and F. Antunes. LCL filter design for grid-connected NPC inverters in offshore wind turbines. In *Proc. of the 7th International Conf. Power Electronics (ICPE)*, pages 1133–1138, 2007.
- [70] Thomas Friedli. *Comparative Evaluation of Three-Phase Si and SiC AC-AC Converter Systems*. PhD thesis, ETH Zurich, 2010.
- [71] *Film Capacitors, Edition 2009*. EPCOS AG.
- [72] R. D. Middlebrook. Design techniques for preventing input filter oscillations in switched-mode regulators. In *Proc. of Powercon 5*, pages A3.1–A3.16, 1978.
- [73] Robert W. Erickson and Dragan Maksimovic. *Fundamentals of Power Electronics*. Springer Science+Business Media, LLC, 2004.
- [74] J. W. Kolar and T. Friedli. The essence of three-phase PFC rectifier systems. In *Proc. of the 33rd IEEE International Telecommunication Energy Conference (INTELEC), Amsterdam, Netherlands*, 2011.

- [75] J. A. Nelder and R. Mead. A simplex method for function minimization. *The Computer Journal*, 4:308–313, 1965.
- [76] M. Schweizer and J. W. Kolar. High efficiency drive system with 3-level T-type inverter. In *Proceedings of the 14th European Conference on Power Electronics and Applications - ECCE Europe, Birmingham, UK*, 2011.
- [77] T. Friedli and J. W. Kolar. A semiconductor area based assessment of ac motor drive converter topologies. In *Proc. of the 24th Annual IEEE Applied Power Electronics Conf. and Exposition (APEC)*, pages 336–342, 2009.
- [78] M. Schweizer, I. Lizama, T. Friedli, and J. W. Kolar. Comparison of the chip area usage of 2-level and 3-level voltage source converter topologies. In *Proc. of the 36th Annual Conf. on IEEE Industrial Electronics Society (IECON)*, pages 391–396, 2010.
- [79] U. Drogenik, G. Laimer, and J. W. Kolar. Theoretical converter power density limits for forced convection cooling. In *Proc. of the International PCIM Europe Conference, Nuremberg, Germany*, 2005.

# Curriculum Vitae

## Personal Data

|               |                      |
|---------------|----------------------|
| Name          | Jonas Mühlethaler    |
| Date of Birth | 16.09.1982           |
| Citizen of    | Lucerne, Switzerland |

## Education

|             |  |
|-------------|--|
| 2008 - 2012 | Ph.D. Studies at the Power Electronic Systems Laboratory, ETH Zurich                   |
| 2003 - 2008 | M.Sc. Studies in Information Technology and Electrical Engineering, ETH Zurich         |
| 2002 - 2003 | Preparation for the Entrance Exam ETH Zurich, AKAD                                     |
| 1998 - 2002 | Apprenticeship as an Electronic Technician (with Berufsmatura), ABB Lernzentren, Baden |
| 1989 - 1998 | Primary School & Bezirksschule, Mellingen  |

## Work Experience

|             |  |
|-------------|--|
| 2012 - ...  | Researcher (Post-Doc) at the Power Electronic Systems Laboratory, ETH Zurich |
| 2008 - 2012 | Research Assistant at the Power Electronic Systems Laboratory, ETH Zurich    |
| 2002 - 2003 | Electronic Technician, Varian Medical Systems, Baden                         |